

MECHANICS OF MACHINING WITH CHAMFERED TOOLS

By

Haikun Ren

B. Sc. Chengdu Technological University, P.R. China

A THESIS SUBMITTED IN PARTIAL FULFILLMENT OF
THE REQUIREMENTS FOR THE DEGREE OF
MASTER OF APPLIED SCIENCE

in

THE FACULTY OF GRADUATE STUDIES
DEPARTMENT OF MECHANICAL ENGINEERING

We accept this thesis as conforming
to the required standard

THE UNIVERSITY OF BRITISH COLUMBIA

March 1998

© Haikun Ren, 1998

In presenting this thesis in partial fulfilment of the requirements for an advanced degree at the University of British Columbia, I agree that the Library shall make it freely available for reference and study. I further agree that permission for extensive copying of this thesis for scholarly purposes may be granted by the head of my department or by his or her representatives. It is understood that copying or publication of this thesis for financial gain shall not be allowed without my written permission.

Department of Mechanical Engineering
The University of British Columbia
2324 Main Mall
Vancouver, Canada
V6T 1Z4

Date: April 22, 1998

Abstract

High speed machining of hardened steels is the recent preferred manufacturing technology in die and mold manufacturing technology. P20 tool steel is the most widely used material in injection molding dies, and its high speed-high productivity machining is the focus of this thesis. P20 has an average hardness of 35 Rc. High speed cutting of P20 is constrained by chatter vibrations, accelerated tool wear and chipping of cutting tool edges. The chamfered cutting tools are used in machining hardened steels due to their increased strength of cutting edges. An analytical model, which allows the evaluation of cutting forces, stress and temperature distribution for cutting tools with chamfered edges, is studied in this thesis.

The cutting process is modeled at three distinct zones by extending the slip line field proposed by Oxley et al. [36]. The primary and secondary deformation zones are treated similar to the work of Oxley, but the flow stress characteristics of the work material are calibrated from orthogonal cutting tests, as opposed to high-speed compression or tensile tests. The chamfer zone is modeled by assuming dead metal trapped over the chamfered edge. The trapped metal is assumed to be stationary and the metal flows around it similar to the extrusion process. The contact between the rake face and chip is assumed to have equal sticking and sliding lengths, and the total contact length is measured experimentally. The flow stress of the material in all three zones are expressed as a function of temperature, strain and strain rate. The deformation and friction energy in all three zones are evaluated individually, and summed to find the total energy consumed in forming the chip. By applying the minimum energy principle to total energy consumed, an average shear angle in the primary shear deformation zone is predicted. The overall analytical model allows evaluation of stress, temperature and cutting forces contributed in each deformation zone for a given set of cutting conditions and

chamfered cutting tool geometry. The predicated and experimental results obtained from orthogonal turning of P20 steel with ISO S10 carbide and Cubic Boron Nitride (CBN) tools agreed well. The model and experimental results indicate that the optimal chamfer angle is about -15 degrees, and optimal cutting speeds are about 240 m/min and 500 m/min for ISO S10 carbide and CBN tools, respectively. The model predicts a rake face temperature, which is just under the diffusion limit of binding materials for S10 and CBN tools at the optimal cutting speeds and chamfer angle.

Table of Contents

Abstract	ii
List of Tables	v
List of Figures	vi
Acknowledgement	vii
Nomenclature	viii
1 Introduction	1
2 Literature Review	4
2.1 Introduction	4
2.2 Mechanics of Orthogonal Machining with Sharp Edge Tools	6
2.2.1 Classical Shear Plane Models	6
2.2.2 Oxley's Shear Zone Model	10
2.3 Mechanics of Orthogonal Cutting with Chamfered Edge Tools	16
2.3.1 The Effect of Tool Edge Geometry on the Cutting Process	16
2.3.2 Zhang's Three Zone Model	19
2.3.3 Summary	19
3 Modeling of Machining with Sharp Tools	20
3.1 Introduction	20
3.2 Modeling of Plastic Deformation in Cutting with Sharp Tools	20

3.2.1	Stress and Strain	20
3.2.2	Plastic Deformation in the Primary Shear Zone	27
3.2.3	Plastic Deformation in the Tool-Chip Interface Zone	29
3.3	Experimental Modeling	32
3.3.1	Experimental Setup	33
3.3.2	Experimental Procedures	36
3.3.3	Modeling of Flow Stresses and Strain Hardening Under High Strain Rate and Temperature Through Machining Tests	47
3.4	Prediction of Cutting Process with Sharp Tools	56
3.4.1	A Minimum Energy Approach	56
3.4.2	Model Verification	61
3.5	Summary	80
4	Modeling of Machining with Chamfered Tools	84
4.1	Introduction	84
4.2	Modeling of Plastic Deformation for Cutting with Chamfered Tools	86
4.2.1	Plastic Deformation in the Primary Shear Zone	88
4.2.2	Plastic Deformation in the Chamfered Edge Zone	89
4.2.3	Plastic Deformation in the Tool-Chip Interface Zone	93
4.2.4	Prediction of Cutting Process with Chamfered Tool	95
4.3	Model Verification	100
4.3.1	Chamfer Tools Used in Machining Tests	101
4.3.2	Predicted and Experimental Results	102
4.3.3	Summary	116
5	Conclusions	118

Bibliography	123
Appendices	129
A Temperature in the Primary Shear and the Tool-Chip Interface Zones	129
B Mapping Flow Stresses in the machining process	131
C Identification of Edge Forces	133

List of Tables

3.1	Chemical composition of P20 mold steel	33
3.2	Mechanical properties of P20 Mold steel	35
3.3	Cutting conditions	41
3.4	Machining test data (“ sharp tool ”), $w=3.6$ mm	44
3.5	Machining test data (“ sharp tool ”), $w=5.0$ mm	47
3.6	Flow stress σ_1 , strain hardening index n , cutting temperature T_{AB} obtained from machining test data	51
3.7	Flow stress σ_{inter} , cutting temperature T_{inter} obtained from machining test data	53
4.1	Cutting conditions and chamfer geometry for the prepared chamfered edge tools used in machining tests. width of cut $w=3.6$ mm, main rake angle $\alpha_o = 0^\circ$. P20 work material: hardness 34 HRC, Composition: C 0.37%, S_i 0.3%, M_n 1.4%, C_r 2.0%, N_i 1.0%, M_o 0.2%. SANDIVIK S10 carbide tool: WC 36.1%, T_iC 39.3%, T_aC 8.6%, C_o 11.0%.	101
4.2	Cutting conditions and chamfer geometry for the CBN (MITSUBISHI MB820) chamfered edge tools used in machining tests. Average width of cut $w=2.55$ mm, main rake angle $\alpha_o = -5^\circ$. CBN tool material composition: CBN 50%, (T_iN and Al_2O_3) 50%.	102

List of Figures

2.1	Diagram of orthogonal cutting	5
2.2	Force diagram in Merchant's model	7
2.3	Chip formation model proposed by Lee and Shaffer [22]	9
2.4	Force diagram of orthogonal cutting proposed by Albrecht [32]	10
2.5	Chip formation model proposed by Oxley and his coworkers	12
2.6	Heat Sources in Cutting Process	15
2.7	Mechanism of SWC cutting	17
2.8	Cross-section of the end of planer chip cutting with SWC tool [15]	18
3.1	State of stresses in plane plastic flow	21
3.2	Velocity diagram in chip formation	26
3.3	Distribution of normal and shear stresses at the tool-chip interface	30
3.4	Diagram of experimental setup for orthogonal machining of P20 mold steel	34
3.5	Shaft used in machining tests	37
3.6	Hardinge CNC turning center used in machining tests	38
3.7	Workpiece used in machining tests	39
3.8	SANDVIK carbide insert	40
3.9	Illustration of measurement of contact length l_c and tool wear land VB from the cutting tool	42
3.10	Plot of correlation of contact length with cutting speed V_w and undeformed chip thickness t_1 , $w=3.6$ mm.	45

3.11 Plot of correlation of shear stress on the shear plane with cutting speed V_w and undeformed chip thickness t_1 , $w=3.6$ mm.	46
3.12 An algorithm of the cutting temperature estimation	50
3.13 Flow stress, strain hardening index, shear strain, shear strain rate, and cutting temperature versus different cutting conditions	55
3.14 A generalized cutting process evaluation algorithm for cutting with sharp edge tools	57
3.15 Predicted shear angles by Merchant's [21] and Lee and Shaffer's [22] shear angle solutions	62
3.16 Comparison of predicted shear angles by the proposed model with experimentally evaluated shear angles, $w=3.6$ mm, $\alpha_o = 0^\circ$, V_w : 240, 380, 600 m/min. . .	64
3.17 Comparison of predicted shear angles by the proposed model with experimentally evaluated shear angles, $w=3.6$ mm, $\alpha_o = 0^\circ$, t_1 : 0.06, 0.08, 0.10 mm. . . .	65
3.18 Variation of experimentally measured contact length l_c and friction angle β with cutting speed V_w	66
3.19 Predicted and experimentally determined friction angles versus various cutting speeds, $w=3.6$ mm, $\alpha_o = 0^\circ$, t_1 : 0.06, 0.08, 0.10 mm.	68
3.20 Predicted and experimentally determined friction angles versus various undeformed chip thickness, $w=3.6$ mm, $\alpha_o = 0^\circ$, V_w : 240, 380, 600 m/min.	70
3.21 Predicted and experimentally determined cutting energy per unit volume of cut, $w=3.6$ mm, $\alpha_o = 0^\circ$, t_1 : 0.06, 0.08, 0.10 mm.	71
3.22 Predicted and experimentally determined cutting energy per unit volume of cut, $w=3.6$ mm, $\alpha_o = 0^\circ$, V_w : 240, 380, 600 m/min.	72
3.23 Predicted cutting temperatures rise in the primary shear zone and the tool-chip interface zone versus cutting speed, $w=3.6$ mm, $\alpha_o = 0^\circ$, t_1 : 0.06, 0.08, 0.10 mm.	74

3.24	Predicted cutting temperatures rise in the primary shear zone and the tool-chip interface zone versus undeformed chip thickness t_1 , $w=3.6$ mm, $\alpha_o = 0^\circ$, V_w : 240, 380, 600 m/min.	75
3.25	Plot of predicted cutting temperatures T_{AB} and T_{inter} and experimentally measured wear rate versus cutting speed, $w=5.0$ mm, $\alpha_o = 0^\circ$, t_1 : 0.06 mm.	77
3.26	Predicted and experimental measured cutting forces versus cutting speed, $w=3.6$ mm, $\alpha_o = 0^\circ$, t_1 : 0.06, 0.08, 0.10 mm.	78
3.27	Predicted and experimentally measured cutting forces versus undeformed chip thickness t_1 , $w=3.6$ mm, $\alpha_o = 0^\circ$, V_w : 240, 380, 600 m/min.	79
3.28	Predicted and experimentally evaluated shear stress in the primary shear zone versus cutting speed, $w=3.6$ mm, $\alpha_o = 0^\circ$, t_1 : 0.06, 0.08, 0.10 mm.	81
3.29	Predicted and experimentally evaluated shear stress in the primary shear zone versus undeformed chip thickness t_1 , $w=3.6$ mm, $\alpha_o = 0^\circ$, V_w : 240, 380, 600 m/min.	82
4.1	A proposed chip formation model for cutting with chamfered tools	87
4.2	A proposed slip-line field for cutting with chamfered tools	91
4.3	A generalized prediction algorithm for cutting with chamfered tools	96
4.4	A procedure to estimate cutting temperatures for cutting with chamfered tools.	98
4.5	Effect of chamfer angle on the predicted and experimental shear angles ϕ (a), (c)) and predicted friction angles β (b), (d) (S10 chamfered carbide tools).	103
4.6	Effect of chamfer angle α_1 on the total cutting forces ((a), (b), (c), (d) and chamfer forces ((e), (f)) (S10 chamfered carbide tools).	105
4.7	Effect of chamfer angle α_1 on the cutting temperature (T_{AB} , T_{inter}) (a), (b) and energy (E_c) (c), (d), (S10 chamfered carbide tools).	107

4.8	Effect of cutting speed on the predicted and experimental shear angle ϕ (a) and predicted friction angle β (b) (MB820 CBN chamfered tools).	109
4.9	Effect of cutting speed V_w on the total cutting forces ((a), (b)) and chamfer forces (c) (MB820 CBN chamfered tools).	110
4.10	Effect of cutting speed V_w on the predicted cutting temperature in the primary shear and the tool-chip interface zones ((a), (b)), the predicted and experimental cutting energy (c) (MB820 CBN chamfered tools).	112
4.11	Comparison of tool wear V_B for chamfered carbide (a), (b), and CBN (c) tools from machining tests.	113
4.12	Comparison of tool wear history between a chamfered tool with -15° chamfer angle and a conventional sharp tool (SANDVIK carbide tools).	115
4.13	Comparison of the tool wear history between a chamfered tool with -15° chamfer angle and a conventional sharp tool (SANDVIK carbide tools).	117
C.1	Experimental identification of edge force components	128
C.2	Plot of variation of edge forces with cutting speed	129

Acknowledgement

I would like to take this opportunity to express my sincere appreciation to Professor Yusuf Altintas, my research supervisor, for the most valuable guidance and the financial support throughout the entire research work. My thanks are also due to all my colleagues in the Manufacturing Automation laboratory at UBC for their assistances, encouragements and friendship. I am grateful to Mr. Mashine and MITSUBISHI Material Corporation, Japan, for their kindness to provide CBN cutting tools and the tool holder.

Finally, I would like to deeply thank my parents and my wife, xiaochun, for their love and steady encouragement during the course of my work. This work is fully dedicated to them.

Nomenclature

α_0	main rake angle of cutting tool (degree)
α_1	chamfer angle (second rake angle) (degree)
b_{cf}	length of chamfer cutting edge (mm)
β	friction angle at the tool-chip interface (degree)
ϕ	shear angle (degree)
t_1	undeformed chip thickness (mm)
w	width of cut (mm)
l_c	contact length along the tool-chip interface (mm)
V_w	cutting speed (m/min.)
V_s	shear velocity (velocity discontinuity) (m/min.)
V_c	chip velocity (m/min.)
F_s	shear force acting on slip-line \overline{AB} (N)
F_c	total cutting force (tangential force) (N)
F_t	total feed force (thrust force) (N)
F_{c-cf}	chamfer force component in cutting direction (N)
F_{t-cf}	chamfer force component in feed direction (N)
R_s	resultant force exerted on slip-line \overline{AB} (N)
σ_1	flow stress corresponding strain $\epsilon = 1.0$
n	strain hardening index
T_{room}	initial temperature of work material ($^{\circ}C$)
T_{AB}	temperature rise in the primary shear zone ($^{\circ}C$)
T_{cf}	temperature rise in the chamfered edge zone ($^{\circ}C$)

T_{inter}	temperature rise at the tool-chip interface ($^{\circ}C$)
T_{mod}	velocity modified temperature (K)
k_{AB}	shear flow stress in the primary shear zone (N/mm^2)
k_{cf}	shear flow stress in the chamfered edge zone (N/mm^2)
σ_{inter}	flow stress acting at the tool-chip interface (N/mm^2)
γ_{AB}	shear strain in the primary shear zone
$\dot{\gamma}_{AB}$	shear strain rate in the primary shear zone (1/second)
ϵ_{cf}	strain in the chamfered edge zone
$\dot{\epsilon}_{cf}$	strain rate in chamfered edge zone (1/second)
$\dot{\gamma}_{inter}$	shear strain rate at the tool-chip interface (1/second)
E_s	energy dissipation in the primary shear deformation zone (J/mm^3)
E_{cf}	energy per unit volume in the chamfered edge zone (J/mm^3)
E_{inter}	energy per unit volume in the tool-chip interface zone (J/mm^3)
E_c	total cutting energy per unit volume (J/mm^3)
ρ	density of material (kg/m^3)
c	specific heat of work material ($J/Kg^{\circ}C$)
κ	thermal conductivity of work material ($J/m S^{\circ}C$)

To my daughter, Deanna

Chapter 1

Introduction

Dies and molds are used in mass production of plastic parts and sheet metal products using forming technology. Various hardened tool steels are used as die materials. In general, the hardness of a tool steel ranges from 30Rc up to 62 Rc depending on the die application. P20 mold steel, which has an average of 35 Rc hardness, is the most widely used as an injection mold material. The molten plastic is injected into a mold, which has the shape of plastic part to be manufactured in massive quantity. Molds are either machined directly from P20 blanks, or chemically eroded using male electrodes. First, male graphite or copper electrodes are milled on special CNC electrode machining centers. Later, the electrode is penetrated into the blank P20 by gradually eroding the work material. Several trials may be necessary until correct mold dimensions are obtained using electrochemical machining process. The current trend is to replace costly and environmentally unfriendly electrochemical machining by direct high speed machining of molds from steel blanks [4].

High speed machining of hardened tool steels has several constraints. The machine tools must have rigid structures, high speed feed and spindles drives and accurate high speed positioning and contouring capability. The current trend in machine tool design is to develop lightweight machine tool drives using linear motor and electro-spindle technology. Likewise, CNC systems, which have high speed computation as well as contouring capabilities, are developed. In parallel to high speed machine tool design, cutting tool material, geometry as well as process design for high speed material removal are also subject of present research. In this thesis, the focus is placed on the analytical modeling of high speed machining processes. The

objective is to identify optimal cutting tool geometry and cutting conditions for a given set of work material, and cutting tool geometry and grade.

In machining, the material is separated from the blank by forming chips. The deformation starts at the primary shear zone, where the undeformed work material experiences severe strain at high strain rates. The stress and temperature depends on the thermoplastic properties of the work material, as well as the cutting tool geometry and cutting conditions. The shear stress in the shear plane depends on the hardness of the material, as well as its flow stress characteristics, which are dependent on the local strain, strain rate and temperature. Higher the material hardness is, higher the stress and temperature will be at the shear zone. Later the deformed material, i.e the chip, travels over the rake face of the cutting tool, thus imparting more deformation and energy to the chip formation process. The chamfered cutting tools are often used in order to strengthen the cutting edges in high speed machining of hardened materials. Some of the deformed material is trapped over the chamfered zone, acting as a protective thermal and mechanical barrier for the cutting tool. Excessive chamfer angles and cutting speeds increase both stress and temperature loading of the cutting tool, which leads to promoter chipping or accelerated tool wear. Optimal selection of chamfer angle and cutting speed is usually evaluated from costly experimental observations. In this thesis, an analytical model of the machining process with chamfered cutting tools is presented. The model allows analytical evaluation of optimal chamfer angle and cutting conditions (i.e. cutting speed) as opposed to costly experimental trials and guesses.

Henceforth the thesis is organized as follows. The literature related to mechanics of cutting, the influence of cutting edge, and cutting conditions on cutting process is reviewed in chapter 2. Chapter 3 presents the mechanics of machining with conventional sharp tools based on the slip line model of Oxley et al. [36]. However, the flow stress properties of the material is evaluated from orthogonal cutting tests as opposed to high speed compression and tensile tests conducted in the past. The model developed in chapter 3 predicts shear angle, cutting forces

and temperature for a given set of cutting conditions and tool geometry. The chamfered cutting tool is considered in chapter 4, where the slip line field is modified to include the chamfered cutting edge zone. The primary and secondary deformation zones are modeled similar to sharp tools. The chamfered zone is considered to have a dead metal trapped over the chamfered edge. The chamfered edge zone is treated like an extrusion process, where the dead metal boundary acts like a die surface. The strain, strain rate and temperature dependent stresses in the three deformation zones are modeled, and the total cutting energy consumed is evaluated. By applying the minimum energy principle, the shear angle in the primary shear deformation zone is predicted. The model leads to prediction of stresses, temperature and forces in each zone as a function of chamfer edge geometry, cutting conditions and material properties of mold steel. Optimal chamfer angle and cutting speed, which give the maximum material removal rate at an acceptable cutting tool temperature, are evaluated. The model is verified by high-speed orthogonal turning of P20 mold steel with chamfered ISO S10 carbide and CBN cutting tools. The optimal chamfer angle has been identified as -15 degrees, and the optimal speeds are about 240m/min for ISO S10 and 500 m/min for CBN cutting tools. The findings are supported by tool wear tests conducted at various speeds with different tool chamfer angles. The thesis is concluded with a summary of contributions and future research work in chapter 5.

Chapter 2

Literature Review

2.1 Introduction

Machining is one of the most common manufacturing processes used in industry. Mechanics of machining process aims at understanding the nature of interaction between cutting tools and work materials. This chapter covers the past and current research and development in the mechanics of orthogonal machining process.

As seen in figure 2.1, the machining process is defined as an operation in which a thin layer of work material, namely, chip, is removed by a wedge-shaped cutting tool from the bulk of work material. A new work surface is formed during machining. Essentially, machining is a process of chip formation. To understand the machining process, it has been usual to simplify the tool geometry from the three dimensional (oblique) geometry to a two dimensional geometry (orthogonal). In orthogonal cutting, the straight cutting edge of the tool is perpendicular to the direction of relative motion between the tool and workpiece. Width of cut w is usually much larger than the undeformed chip thickness t_1 . The removed chip is formed under approximately plane strain conditions. Orthogonal cutting is approximately a steady-state process if the continuous chip is formed during machining.

In general, machining process is influenced by:

- Material properties
- Strain and strain rate
- Tool geometry, tool material, and temperature

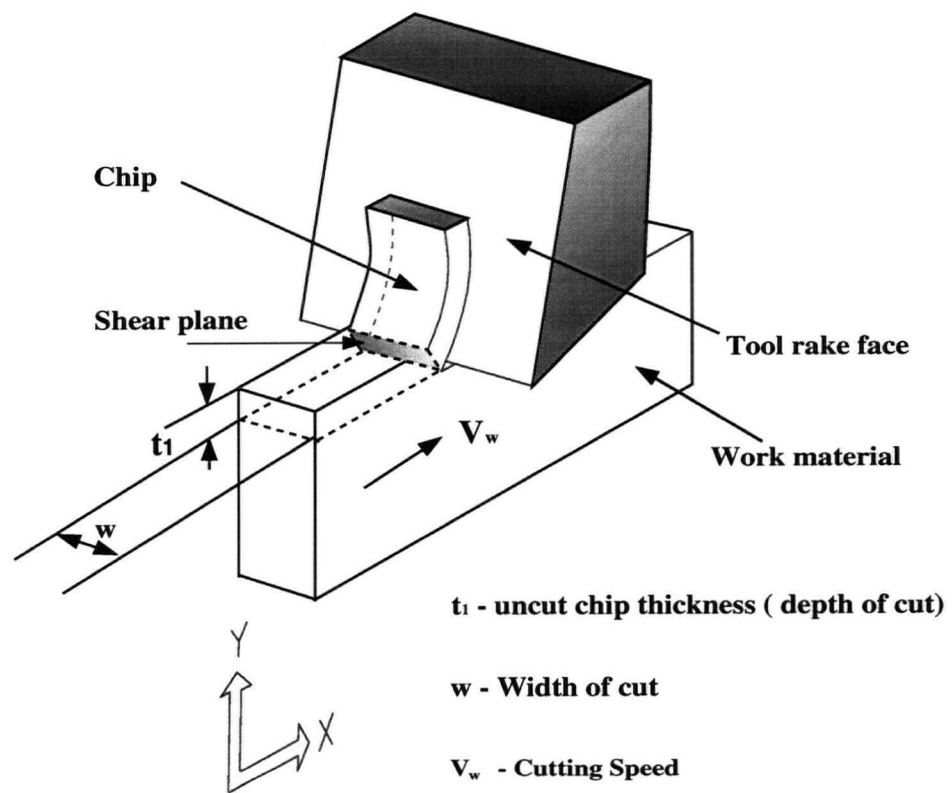


Figure 2.1: Diagram of orthogonal cutting

During machining, the chip is formed by shearing. The whole volume of metal removed is plastically deformed, undergoing large strain and high strain rate. Thus, a large amount of energy is required to form the chip and move it across the tool face. Understanding the chip formation is essential to the problems associated with the rate of metal removal and tool performance.

2.2 Mechanics of Orthogonal Machining with Sharp Edge Tools

2.2.1 Classical Shear Plane Models

Much research effort has been made in understanding the chip formation since the shear plane model was proposed by Ernst and Merchant [21]. In Merchant's model, the shear stress is assumed to be invariant with shear angle and is distributed uniformly along shear plane. Chip is formed continuously without a built-up edge. Chip is formed as the result of plastic shear deformation along a plane ahead of the cutting edge. Work velocity is instantaneously changed to the chip velocity. This requires a velocity discontinuity in the direction along the shear plane. From figure 2.2, chip ratio r_c is determined by

$$r_c = \frac{t_1}{t_2} = \frac{\sin \phi}{\cos(\phi - \alpha_o)} \quad (2.1)$$

Where ϕ is shear angle, α_o is rake angle of tool, t_1 is undeformed chip thickness, and t_2 is the deformed chip thickness. From equation 2.1, shear angle ϕ can be found by measuring chip ratio r_c .

$$\tan \phi = \frac{r_c \cos \alpha_o}{1 - r_c \sin \alpha_o} \quad (2.2)$$

Cutting forces are not only associated with the energy input in the machining process, but also they affect the surface finish and tool life. Therefore, it is important to determine the cutting

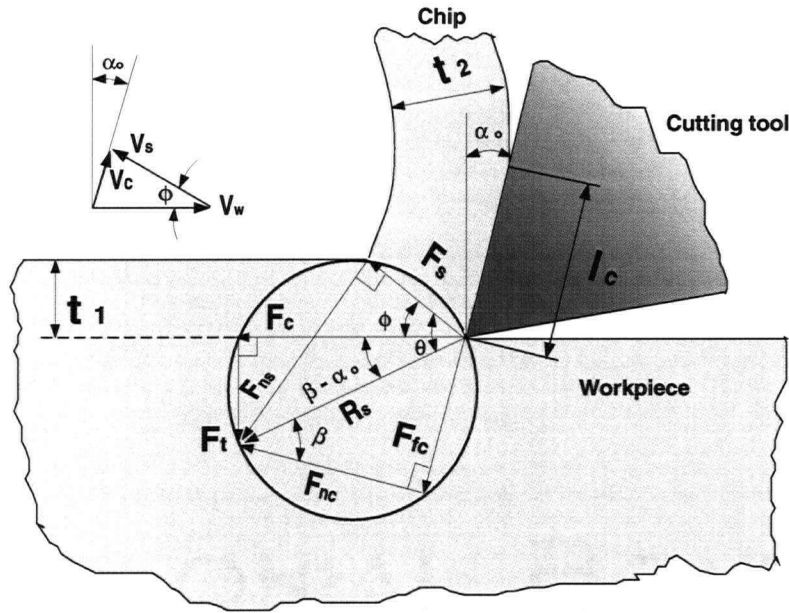


Figure 2.2: Force diagram in Merchant's model

forces required for the given chip load and tool geometry. The cutting forces, tool and chip geometry were related in Merchant's model as seen in figure 2.2. In Merchant's model, cutting force F_c and feed force F_t are determined if the shear angle ϕ , friction angle β , shear stress τ , tool rake angle α_o , and chip load t_1 , w are known.

$$F_c = \frac{t_1 w \tau \cos(\beta - \alpha_o)}{\sin \phi \cos \theta} \quad (2.3)$$

$$F_t = \frac{t_1 w \tau \sin(\beta - \alpha_o)}{\sin \phi \cos \theta} \quad (2.4)$$

$$\theta = \phi + \beta - \alpha_o \quad (2.5)$$

where θ defines a angle between resultant force R_s and shear plane. Assuming ideal plastic work material, Merchant proposed a shear angle solution using minimum energy method. The

cutting energy per unit volume W_c is found by

$$W_c = \frac{F_c V_w}{V_w t_1 w} \quad (2.6)$$

$$\frac{\partial W_c}{\partial \phi} = \frac{t_1 w \tau}{t_1 w} \frac{\partial}{\partial \phi} \left[\frac{\cos(\beta - \alpha_o)}{\sin \phi \cos(\phi + \beta - \alpha_o)} \right]$$

$$\frac{\partial W_c}{\partial \phi} = 0 \quad (2.7)$$

$$\frac{\cos(\beta - \alpha_o) \cos(2\phi + \beta - \alpha_o)}{\sin^2 \phi \cos^2(\phi + \beta - \alpha_o)} = 0$$

$$2\phi + \beta - \alpha_o = \frac{\pi}{2} \quad (2.8)$$

Which yields to Merchant's shear angle prediction

$$\phi = \frac{\pi}{4} - \left(\frac{\beta - \alpha_o}{2} \right) \quad (2.9)$$

Quantitatively, this equation has been observed to overestimate shear angles. However, as Turkovitch [18] suggested, shear angle solution 2.9 proposed by Merchant provides a reference for checking other solutions.

Lee and Shaffer[22] developed a model which gives cutting forces, the chip thickness, and chip formation from tool geometry, the relevant coefficients of friction, and flow stress of work material. Again, continuous chip formation and sharp tool were assumed. Their model applies theory of ideal plastic deformation without work hardening. Figure 2.3 shows slip line field postulated by Lee and Shaffer. Since slip lines parallel to \overline{AC} are straight, the stress distribution is uniform in the region ABC. There is no stress transmitted above \overline{AB} , which is a free stress surface. \overline{AC} , the shear plane is inclined at $\frac{\pi}{4}$ with \overline{AB} . From Mohr circle and geometrical relationship, the shear angle equation is

$$\eta + \beta = \frac{\pi}{4} \quad (2.10)$$

$$\phi = \eta + \alpha_o = \frac{\pi}{4} - (\beta - \alpha_o) \quad (2.11)$$

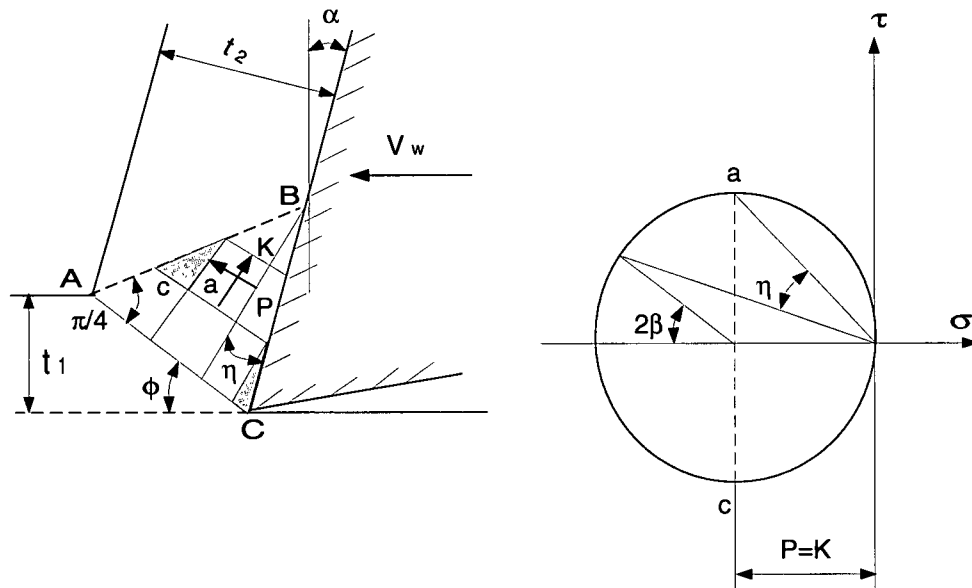


Figure 2.3: Chip formation model proposed by Lee and Shaffer [22]

Albrecht [32] first realized that ploughing process around cutting edge exists as a secondary mechanism during cutting beside the shear process. He pointed out that any fresh tool has only finite sharpness. Edge forces due to ploughing process have no contribution to shear process in the chip formation. Albrecht proposed a new force diagram of the orthogonal cutting process as seen in figure 2.4.

In Albrecht's work, the effect of cutting speed on cutting forces were analyzed. He suggested that only ploughing force \mathbf{P} is affected by the cutting speed. As cutting speed increases, cutting forces decrease due to the the decrease of ploughing forces and absence of the built-up edge.

Armarego [33] generalized a computer based modelling for the estimation of machining characteristics, such as forces and power. He suggested that forces arise from two sources, that is, work material deformation and edge effect. Cutting force coefficients are determined from the thin shear zone analysis. The “ edge ” force components are found from machining

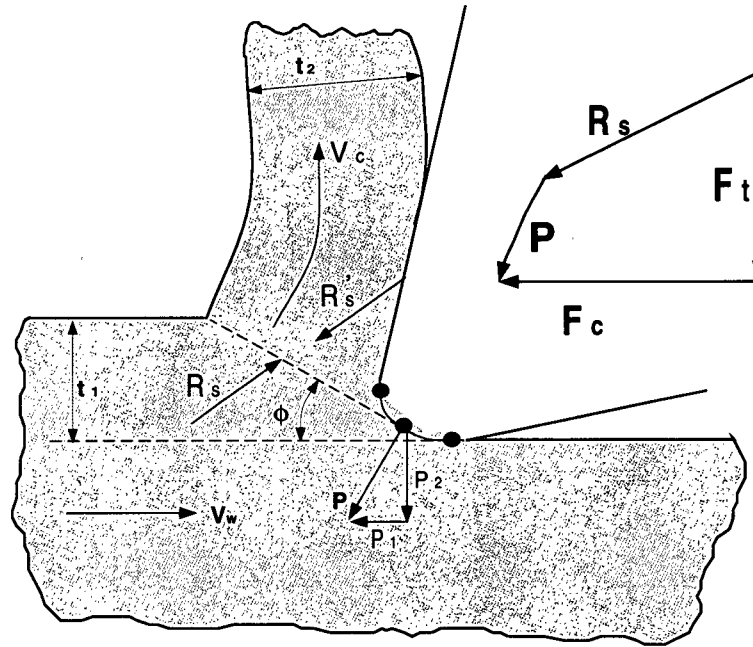


Figure 2.4: Force diagram of orthogonal cutting proposed by Albrecht [32]

experiments by extrapolating measured cutting forces at zero undeformed chip thickness. The mechanics of orthogonal cutting can be extended to analyze more complex machining process. To model a relative complex machining process, such as milling, Budak, Altintas and Armarego [1] proposed a unify model to determine the cutting coefficients for milling process from the orthogonal cutting test data in order to obtain elemental force components.

2.2.2 Oxley's Shear Zone Model

Metal cutting is a highly complicated process. The flow stress of metals varies with strain, strain rate, and temperature when materials undergo a large plastic deformation. The classical shear plane models fail to explain how flow stress of plastic deformation and frictional state along the tool-chip interface are influenced with variations in the cutting speed. Furthermore, the important characteristics, such as cutting temperatures, the variation of strain rate under

different cutting conditions, can not be analyzed from the classical machining theories, for instance, such as Merchant's model [21].

Oxley and his colleagues [6] developed a shear zone model applying the plastic theory to the analysis of chip formation. Flow stress of work material varies with strain, strain rate, temperature, and the frictional conditions at the tool-chip interface described in terms of the shear flow stress in the layer of chip material adjacent to the tool rake face. The shear zone model they proposed can account for the influence of cutting conditions and work material properties on the important variables in machining, such as cutting forces and cutting temperatures.

The chip formation model proposed by Oxley and his coworkers can be represented as shown in figure 2.5. Their theory is based on a chip formation model derived from the analysis of experimental flow fields. Plane strain, steady-state cutting conditions with continuous chip formation are assumed to apply and cutting tool is assumed to be perfectly sharp. Hence, Plastic zone mainly consists of the primary shear zone and secondary deformation zone at the tool-chip interface.

\overline{AB} is a slip-line which represents the direction of maximum shear strain rate and maximum shear stress. Based on the experimental observation, Oxley et al. [7] suggested that the maximum shear strain rate can be estimated from

$$\dot{\gamma}_{AB} = S_c \frac{V_s}{l_{AB}} \quad (2.12)$$

where V_s is the shear velocity, l_{AB} is the length of \overline{AB} , and S_c is a constant. In the secondary deformation zone, a flow zone exists along the tool-chip interface and around the cutting edge due to high compressive stress applied at the rake face-chip interface. Sticking friction is assumed to prevail inside secondary deformation zone. Then the shear strain rate in tool-chip interface zone is given by

$$\dot{\gamma}_{inter} = \frac{V_c}{\delta \cdot t_2} \quad (2.13)$$

where δ is the ratio of the average thickness of interface plastic zone to the chip thickness t_2 . V_c is chip velocity. The governing equation of stress and strain in the primary shear zone is determined by applying the “power law”.

$$\sigma = \sigma_1 \epsilon^n \quad (2.14)$$

where σ_1 and ϵ are effective plastic stress and effective plastic strain. n represents the strain hardening exponent. To account for the effects of strain rate and cutting temperatures, velocity modified temperature which was first suggested by Macgregor and Fisher [20] was introduced to combine the effects of strain rate and temperature on the variation of flow stress. Velocity modified temperature T_{mod} can be expressed as

$$T_{mod} = (T + 273.0)[1 - \nu \log_{10}(\dot{\epsilon})] \quad (2.15)$$

where T is cutting temperature ($^{\circ}C$) rise in plastic deformation zone, $\dot{\epsilon}$ is strain rate, ν is material constant. Oxley [6] suggested that for a given strain, the flow stress σ_1 and strain hardening index n for a particular work material can be assumed to be a unique function of velocity modified temperature T_{mod} . Essentially, σ_1 and n should be obtained for a wide range of strain rate and temperature. High speed compression test by Oyane et al. [16] provided a very wide range of temperature ($0 \sim 1100^{\circ}C$) with constant strain rate (450 1/s). Hastings, Mathew, and Oxley applied Oyane's test data to obtain the correlation of flow stress and strain hardening exponent with velocity modified temperature. Although they determined the flow stress under a high speed compression tests which do not cover high strains and strain rates observed in machining, their work is the most fundamental approach in modeling the machining process based on the laws of plasticity.

Through the analysis of chip formation, calculating temperature rise in plastic deformation zone is an important aspect since it changes the material properties and influences tool life

directly. Stephenson [37] pointed out that model of Loewen and Shaw [39], the model of Boothroyd [19] as modified by Oxley and his coworkers, et.al. are well known among others in the study of temperature distribution in cutting process. Models they proposed are all based on the assumption of shear plane idealization and cutting with sharp tool. Figure 2.6 shows heat sources on the shear plane and tool rake face. Cutting energy is converted into heat due to plastic work. $\lambda_s Q_s$ represents a portion of heat which flows into work material and $(1 - \lambda_s) Q_s$ stands for the amount of heat flowing into the chip. Similarly, a portion of heat flows into chip and another portion of heat flows into cutting tool due to friction occurred at tool-chip interface. The rate of energy consumed during cutting is given by

$$W_c = F_c V_w \quad (2.16)$$

The energy is transformed as heat into two main regions, namely, the primary shear zone, and the secondary deformation zone at the tool-chip interface. The plastic work done W_s on shear plane is the product of shear force F_s and shear velocity V_s

$$W_s = F_s V_s = \frac{F_s V_w \cos \alpha_o}{\cos(\phi - \alpha_o)} \quad (2.17)$$

The temperature rise in the primary shear zone is found by adding initial temperature T_{room} in work material to a portion of heat generated by the plastic deformation occurred in primary shear zone

$$T_{AB} = T_{room} + \eta \left[\frac{(1 - \lambda_s) F_s \cos \alpha_o}{\rho c t_1 w \cos(\phi - \alpha_o)} \right] \quad (2.18)$$

Where λ_s and η are the proportion of heat conducted into work material and a factor which defines the amount of heat converted from plastic work, respectively. ρ and c are material density specific heat, respectively.

The average temperature rise at the tool-chip interface is determined by summing up the temperature rise in primary shear zone T_{AB} and the maximum temperature ΔT_M rise at the tool-chip interface.

$$T_{inter} = T_{AB} + \psi \Delta T_M \quad 0 < \psi < 1.0 \quad (2.19)$$

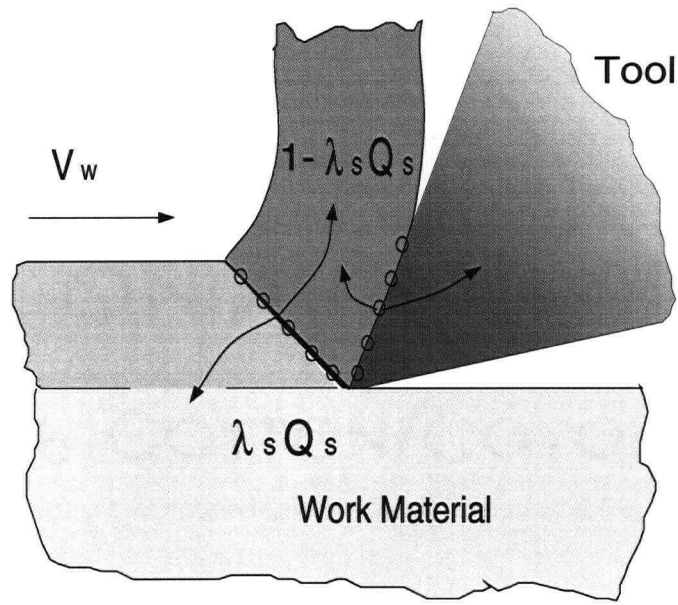


Figure 2.6: Heat Sources in Cutting Process

Again, ψ is a factor to allow for possible variations of temperature along the interface. For a given tool rake angle α_o , undeformed thickness t_1 , the cutting speed V_w , cutting forces can be estimated provided the correlation of flow stress of work material with velocity modified temperature is known. Once shear angle ϕ is given, then force components applied to cutting are determined from following geometrical force equations

$$\left. \begin{aligned} R_s &= \frac{F_s}{\cos\theta} = \frac{k_{AB} t_1 w}{\sin\phi \cos\theta} \\ F_{fc} &= R_s \sin\beta \\ F_{nc} &= R_s \cos\beta \\ F_c &= R_s \cos(\beta - \alpha_o) \\ F_t &= R_s \sin(\beta - \alpha_o) \\ F_s &= \frac{k_{AB} t_1 w}{\sin\phi} \end{aligned} \right\} \quad (2.20)$$

where k_{AB} is shear flow stress acting on slip-line \overline{AB} . The procedures for predicting cutting

forces and cutting temperatures, etc. will be discussed in more detail in chapter 3.

2.3 Mechanics of Orthogonal Cutting with Chamfered Edge Tools

In the literature, the investigation on tool geometry mainly consists of two categories. One is the tool edge geometry, and the other emphasizes on the tool rake geometry, such as restricted contact length tools. This section presents some investigative work on the effect of tool geometry on the machining process.

2.3.1 The Effect of Tool Edge Geometry on the Cutting Process

As M.C. Shaw [39] pointed out, Klopstock was the first to show that tool life and cutting forces could be altered by restricting the contact length between the tool and chip. K.Hitomi [46] reported that Hoshi invented the “ silver-white ” chip cutting method (SWC) as seen in figure 2.7. SWC edge is designed with negative rake angle to provide chamfered edge, and a positive rake angle as main rake face. A chip former is provided in the case of the turning tool in order to control the chip. The chamfer traps the work material over the chamfered edge, and the formed dead metal acts like a cutting edge which increases the tool edge strength and reduces tool wear.

Figure 2.8 shows chip formation with SWC tool. Hosi [15] suggested that SWC tool performs a unique cutting mechanism involving the controlled built-up edge, and it offers increased tool edge strength, freedom from chip adhesion.

E. Usui, K. KiKuchi and K. Hoshi [49] first attempted to model cutting with the cut away tool (artificially controlled tool-chip contact length tool). They applied the theory of ideal plastic deformation material to postulate the plastic flow fields which consist of one centre-fan and two straight slip-line fields. Based on the characteristics of slip-line fields, a quantitative formula was obtained to determine the coefficient of friction on the rake face with artificial

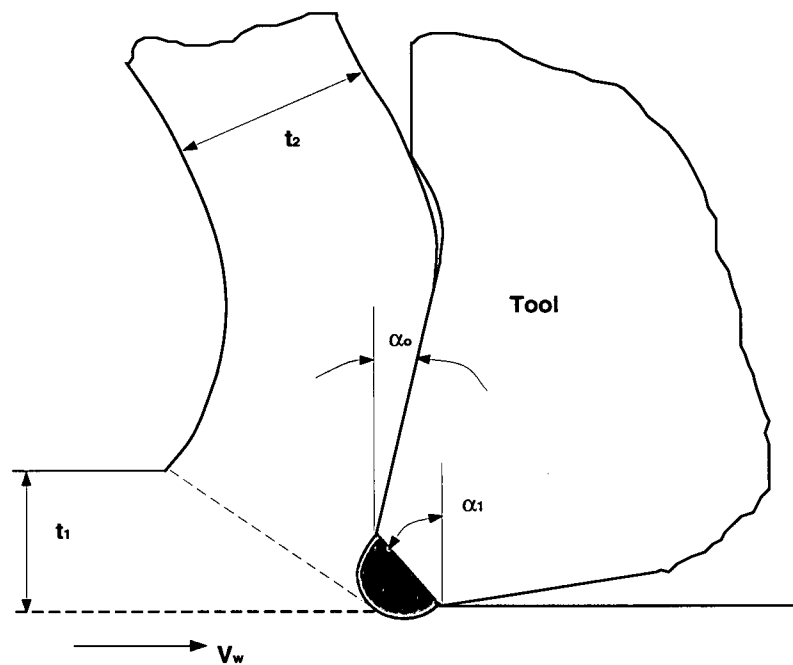


Figure 2.7: Mechanism of SWC cutting

restriction of the tool-chip contact length. S. Jacobson and P. Wallen [47] investigated the dead metal zone with different edge geometry. From their experimental evidence, they found that the chamfered cutting edge is almost completely filled by a dead metal zone. They suggested that the relative motion between chip and tool is under the condition of seizure, thus, the secondary shear occurs inside the chip, and the work material adjacent to the chamfer is stagnated. A dead metal zone is formed as a result. M. Hirao, J. Tlustý, et al. [3] observed the same mechanism from their machining tests. They found that a dead metal forms over the chamfer which acts as a cutting edge, and the chip is formed essentially the same way as compared to cutting with and without chamfer, but, the forces are different. They reported that the chamfer has more influence on the thrust (feed) force than the tangential force.

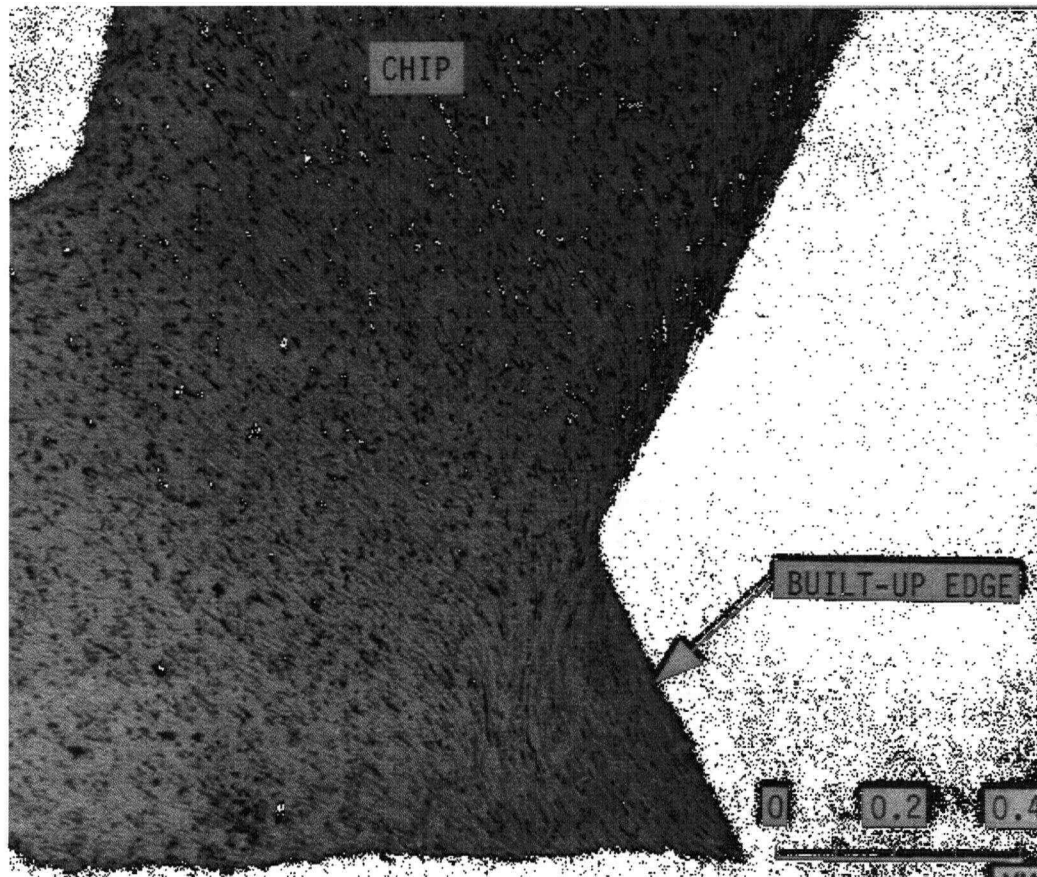


Figure 2.8: Cross-section of the end of planer chip cutting with SWC tool [15]

2.3.2 Zhang's Three Zone Model

H.T. Zhang, P.D. Liu and R.S. Hu [50] analyzed the mechanics of machining with chamfered tools by considering the primary, dead metal and the secondary deformation zones separately. Their model predicts shear angle in orthogonal machining with chamfered tools. Based on their experimental observations using microphotographic and quick-stop techniques, it is found that the existence of dead metal zone is not dependent on the cutting speed, tool main rake angle or the chamfer angle. They concluded that the decrease of shear angle due to chamfer is about $2^\circ \sim 3^\circ$ compared to that for cutting with sharp tools under same cutting conditions.

2.3.3 Summary

The major shortcoming of classical shear plane models is that strain hardening, strain rate sensitivity, and thermo-mechanical coupling are neglected. It is essential for high speed machining to analyze these important features. The "shear zone" model proposed by Oxley et al. [6] included these effects in a model giving more realistic explanation. Their model only considered machining with sharp tools and required flow stress of material from high speed compression tests. Finite element method by Strenkowski and Carroll [56], Komvopoulos and Erpenbeck [57], and Ortiz and Marusich [58] can describe the temperature, stress and strain rate distribution in more detail. However finite element modeling of machining process requires intensive computation time and problems associated with the criterion of elemental node separation and modeling of the tool-chip interface due to large deformation are still difficult to solve at the present stage.

The past work reported on the mechanics of machining with chamfered tools was mainly experimental, and lacked the support of an analytical model. In this thesis a comprehensive analytical model of the process is developed as shown in the following chapters.

Chapter 3

Modeling of Machining with Sharp Tools

3.1 Introduction

Mechanics of machining aims to investigate how process variables, such as cutting forces, power, and temperature etc., vary with the machining conditions and materials properties. In this chapter, a mechanics model for the machining with conventional sharp tools is presented. Strain, strain rate, temperature and stress are evaluated based on the model proposed by Oxley et al. [6], [36]. The flow stress of work material under high strain rate and temperature is modeled through orthogonal machining tests with S10 carbide sharp tools on P20 mold steel. A minimum energy method is proposed to predict shear angle from given cutting conditions. Hence, the model developed in this chapter focuses on the plastic deformation in two main areas, namely, the primary shear and the secondary deformation (tool-chip interface zone) zones. Energy dissipation involved in these two regions are formulated. In the predictions of cutting forces, the analysis of edge forces is incorporated. To compare the predictions by this model, orthogonal cutting tests have been performed. Through analysis, steady-state cutting with continuous chip formation, sharp edge tool, and plane strain are assumed.

3.2 Modeling of Plastic Deformation in Cutting with Sharp Tools

3.2.1 Stress and Strain

For plane strain problems, the plastic flow is parallel to the xy plane, and velocity field is independent of Z direction. Figure 3.1 shows the state of stresses bounded by slip-lines.

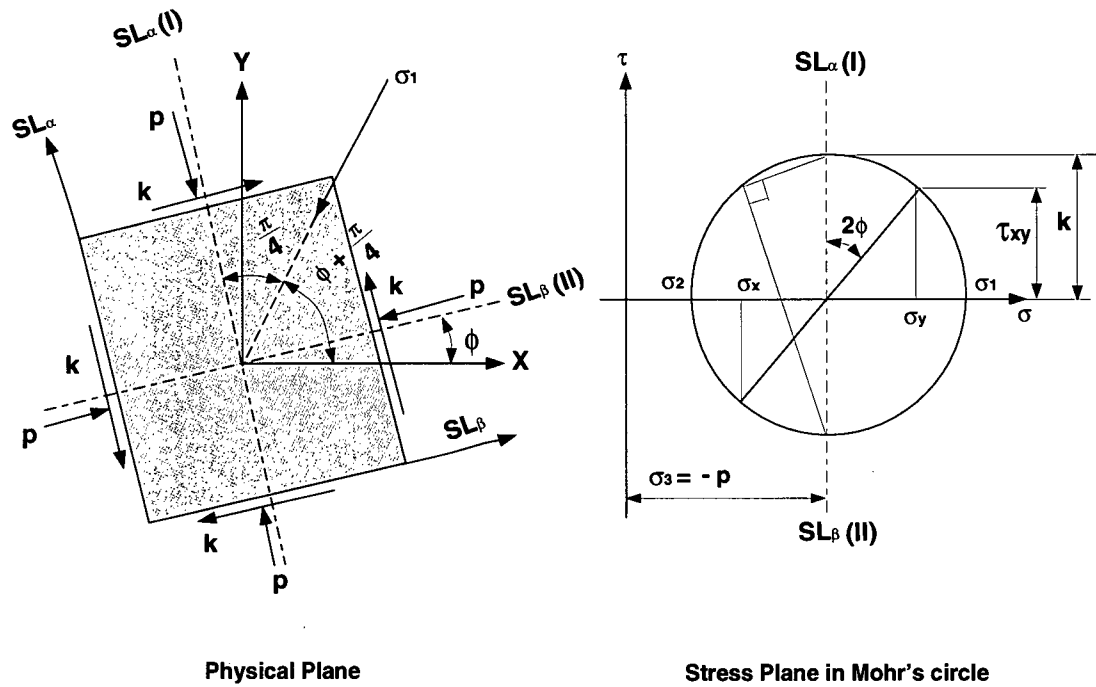


Figure 3.1: State of stresses in plane plastic flow

Through each point in the plane of plastic flow, a pair of orthogonal curves along which the shear stress has its maximum value k . These curves are called slip-lines denoted by SL_α and SL_β lines. The families of slip-lines represent the direction of maximum shear stress and maximum shear strain rate at every point in the plastic deformation region. The stress acting on the slip-lines is shear stress k and the normal stress on the slip-lines is hydrostatic stress p . The state of stresses at a point is completely determined if p and k and orientation of slip-lines are known.

The work material is assumed to be isotropic. The components of stress depend only on x

and y.

$$\tau_{xz} = \tau_{yz} = 0 \quad (3.1)$$

The Lèvy-Mise stress-strain increment equations [59] are expressed as

$$d\epsilon_{ij} = \sigma_{ij}' d\lambda = \left(\frac{2}{3}\right) \left(\frac{d\bar{\epsilon}}{\bar{\sigma}}\right) \sigma_{ij}' \quad (3.2)$$

$$d\epsilon_{ij} = (\sigma_{ij} - \sigma_m) d\lambda \quad \text{where} \quad \sigma_m = \frac{(\sigma_x + \sigma_y + \sigma_z)}{3} \quad (3.3)$$

$$d\epsilon_z = \left(\frac{2}{3}\right) d\lambda \left\{ \sigma_z - \frac{(\sigma_x + \sigma_y)}{2} \right\} \quad (3.4)$$

where σ_{ij}' is the deviator stress tensor and $d\lambda$ is a scalar non-negative constant of proportionality which is not material constant and may vary throughout the stress history. The z direction is a principle direction. Thus, σ_z is a principle stress. For the plane strain problem, strain and shear stress related in Z direction show

$$\epsilon_z = \gamma_{xz} = \gamma_{yz} = 0 \quad (3.5)$$

Therefore

$$d\epsilon_z = d\gamma_{xz} = d\gamma_{yz} = 0 \quad (3.6)$$

From equation 3.4, σ_z and hydrostatic stress are obtained

$$\sigma_z = \frac{(\sigma_x + \sigma_y)}{2} \quad (3.7)$$

$$\sigma_m = \frac{(\sigma_x + \sigma_y + \sigma_z)}{3} \quad (3.8)$$

$$= \frac{\left\{ \sigma_x + \sigma_y + \frac{1}{2}(\sigma_x + \sigma_y) \right\}}{3}$$

$$= \frac{(\sigma_x + \sigma_y)}{2}$$

$$\sigma_z = \sigma_m = p \quad (3.9)$$

Applying Von Mises yield criterion for plane strain plastic deformation gives

$$(\sigma_x - \sigma_y)^2 + (\sigma_y - \sigma_z)^2 + (\sigma_z - \sigma_x)^2 + 6(\tau_{xy}^2 + \tau_{yz}^2 + \tau_{zx}^2) = 6k^2 \quad (3.10)$$

where k is the yield stress in pure shear. Equation 3.10 reduces to

$$(\sigma_x - \sigma_y)^2 + 4\tau_{xy}^2 = 4k^2 \quad (3.11)$$

In the absence of body forces, the equations of equilibrium for quasi-static deformation for plane strain problem are

$$\begin{cases} \frac{\partial \sigma_x}{\partial x} + \frac{\partial \tau_{xy}}{\partial y} = 0 \\ \frac{\partial \tau_{xy}}{\partial x} + \frac{\partial \sigma_y}{\partial y} = 0 \end{cases} \quad (3.12)$$

From Mohr's circle as shown in figure 3.1, the yield criterion is satisfied by

$$\begin{cases} \sigma_x = -p - k \sin 2\phi \\ \sigma_y = -p + k \sin 2\phi \\ \tau_{xy} = k \cos 2\phi \end{cases} \quad (3.13)$$

Substituting equation 3.13 into the equilibrium equations 3.12 and differentiating and collecting terms gives

$$\begin{cases} \frac{\partial p}{\partial x} + 2k \cos 2\phi \frac{\partial \phi}{\partial x} + 2k \sin 2\phi \frac{\partial \phi}{\partial y} = 0 \\ \frac{\partial p}{\partial y} - 2k \cos 2\phi \frac{\partial \phi}{\partial y} + 2k \sin 2\phi \frac{\partial \phi}{\partial x} = 0 \end{cases} \quad (3.14)$$

The choice of x and y axes are arbitrary, let x and y axes be tangential to the SL_α and SL_β shear slip lines direction. Thus, ϕ is zero. If material is assumed to be perfectly plastic (non-hardening) with constant k , equations 3.14 reduce to

$$\begin{cases} \frac{\partial p}{\partial x} + 2k \frac{\partial \phi}{\partial x} = 0 \text{ along } SL_\alpha \text{ line} \\ \frac{\partial p}{\partial y} - 2k \frac{\partial \phi}{\partial y} = 0 \text{ along } SL_\beta \text{ line} \end{cases} \quad (3.15)$$

Integrating equation 3.15 gives the well known Hencky's equations

$$\begin{cases} \Delta p + 2k\phi = 0 \text{ along } SL_\alpha \text{ line} \\ \Delta p - 2k\phi = 0 \text{ along } SL_\beta \text{ line} \end{cases} \quad (3.16)$$

Palmer and Oxley [61] proposed a modified Hencky's equation which allows for the variation of yield stress when the work-hardening of the material is taken into account. Again, let the x and y axes be taken along the tangents to the SL_α and SL_β lines respectively, this corresponds to $\phi = 0$, yields

$$\begin{aligned}
 -\frac{\partial \mathbf{p}}{\partial x} - \sin 2\phi \frac{\partial \mathbf{k}}{\partial x} - 2\mathbf{k} \cos 2\phi \frac{\partial \phi}{\partial x} + \cos 2\phi \frac{\partial \mathbf{k}}{\partial y} - 2\mathbf{k} \sin 2\phi \frac{\partial \phi}{\partial y} &= 0 \\
 -\frac{\partial \mathbf{p}}{\partial y} + \sin 2\phi \frac{\partial \mathbf{k}}{\partial y} + 2\mathbf{k} \cos 2\phi \frac{\partial \phi}{\partial y} + \cos 2\phi \frac{\partial \mathbf{k}}{\partial x} - 2\mathbf{k} \sin 2\phi \frac{\partial \phi}{\partial x} &= 0 \\
 \left\{ \begin{array}{l} \frac{\partial \mathbf{p}}{\partial SL_\alpha} + 2\mathbf{k} \frac{\partial \phi}{\partial SL_\alpha} - \frac{\partial \mathbf{k}}{\partial SL_\beta} = 0 \quad \text{along } SL_\alpha \text{ line} \\ \frac{\partial \mathbf{p}}{\partial SL_\beta} - 2\mathbf{k} \frac{\partial \phi}{\partial SL_\beta} - \frac{\partial \mathbf{k}}{\partial SL_\alpha} = 0 \quad \text{along } SL_\beta \text{ line} \end{array} \right. & \quad (3.17)
 \end{aligned}$$

Equation 3.17 presented by Palmer and Oxley [61] indicates that the variation of hydrostatic stress \mathbf{P} along a slip line is not only dependent on the curvature of slip line, but also upon the rate of change on the flow stress of work material in a direction perpendicular to the slip line. Having analyzed the experimental flow field in machining process, Hasting, Mathew and Oxley [36] presented a theory of chip formation. As illustrated in figure 2.5, plastic deformation undergoes in a finite thickness zone in Oxley's shear zone analysis. The plane AB and tool-chip interface are both assumed to be the direction of maximum shear stress and maximum shear strain rate. From equation 3.17, let AB be SL_α slip line in the primary shear zone. The variation of hydrostatic stress along \overline{AB} \mathbf{p} and shear flow stress \mathbf{k}_{AB} are expressed as

$$\frac{\partial \mathbf{p}}{\partial SL_\alpha} + 2\mathbf{k}_{AB} \frac{\partial \phi}{\partial SL_\alpha} - \frac{\partial \mathbf{k}_{AB}}{\partial SL_\beta} = 0 \quad (3.18)$$

If slip-line \overline{AB} is assumed a straight line, this leads to

$$\frac{\partial \phi}{\partial SL_\alpha} = 0 \quad (3.19)$$

Then,

$$\frac{\partial \mathbf{p}}{\partial SL_\alpha} = \frac{\partial \mathbf{k}_{AB}}{\partial SL_\beta} \quad (3.20)$$

The flow stress and strain relation is governed by power law and is expressed as

$$\sigma_{AB} = \sigma_1 (\epsilon_{AB})^n \quad (3.21)$$

From Von Mise yield criterion, shear flow stress \mathbf{k}_{AB} , strain rate $\dot{\epsilon}_{AB}$, and strain ϵ_{AB} are

$$\left. \begin{aligned} \mathbf{k}_{AB} &= \frac{\sigma_{AB}}{\sqrt{3}} \\ \epsilon_{AB} &= \frac{\gamma_{AB}}{\sqrt{3}} \\ \dot{\epsilon}_{AB} &= \frac{\dot{\gamma}_{AB}}{\sqrt{3}} \end{aligned} \right\} \quad (3.22)$$

From equation 3.21, the variation of flow stress σ_{AB} with ϵ_{AB} can be expressed as

$$\frac{d\sigma_{AB}}{d\epsilon_{AB}} = \frac{n \sigma_{AB}}{\epsilon_{AB}} \quad (3.23)$$

Similarly, taking the derivative for equations 3.22 gives

$$\mathbf{k}_{AB} = \frac{\sigma_1 \epsilon_{AB}^n}{\sqrt{3}} \quad (3.24)$$

$$\begin{aligned} \frac{d\mathbf{k}_{AB}}{d\gamma_{AB}} &= \frac{d\sigma_{AB}}{d\epsilon_{AB}} = \frac{n \sigma_1 \left(\frac{\gamma_{AB}}{\sqrt{3}}\right)^{n-1} \frac{1}{\sqrt{3}}}{\sqrt{3}} \\ &= \frac{n \sigma_1 \left(\frac{\gamma_{AB}}{\sqrt{3}}\right)^n}{\sqrt{3} \gamma_{AB}} = \frac{n \mathbf{k}_{AB}}{\gamma_{AB}} \end{aligned} \quad (3.25)$$

Therefore, the variation of shear flow stress along SL_β slip line which is perpendicular to AB can be expressed as the form

$$\frac{d\mathbf{k}_{AB}}{dSL_\beta} = \frac{d\mathbf{k}_{AB}}{d\gamma_{AB}} \frac{d\gamma_{AB}}{dt} \frac{dt}{dSL_\beta} \quad (3.26)$$

where dt is time interval. $\frac{dt}{dSL_\beta}$ can be determined from velocity diagram as shown in figure 3.2. Where SL_β corresponds to \overline{CF} or \overline{EA} if $\overline{AA'} = V_w dt$.

$$\overline{EA} = \overline{AA'} \sin \phi = V_w \sin \phi dt \quad (3.27)$$

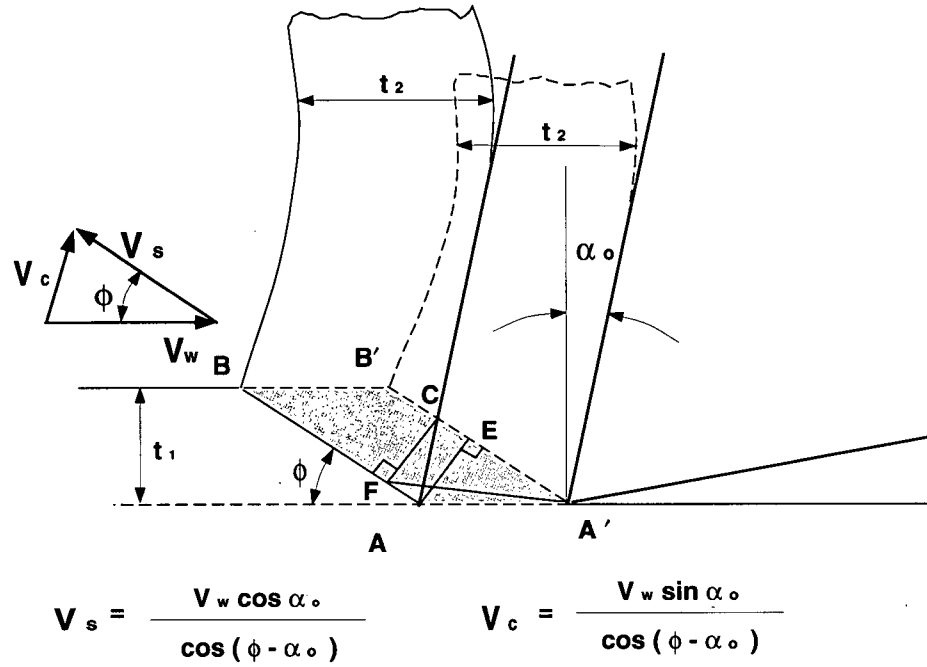


Figure 3.2: Velocity diagram in chip formation

Then, $\frac{dt}{dSL_\beta}$ is given by

$$\frac{dt}{dSL_\beta} = \frac{1}{V_w \sin \phi} \quad (3.28)$$

Shear strain occurring as work material crosses the slip-line \overline{AB} is given from geometrical relation shown in figure 3.2.

$$\left. \begin{aligned} \gamma_{AB} &= \frac{A'C}{FC} = \frac{A'E}{AE} + \frac{CE}{AE} \\ &= \frac{1}{\tan \phi} + \tan(\phi - \alpha_o) \\ &= \frac{\cos \alpha_o}{\sin \phi \cos(\phi - \alpha_o)} \end{aligned} \right\} \quad (3.29)$$

Hence, substituting equations 3.28, 3.25 into equation 3.26, the variation of shear flow stress

along AB as shown in figure 2.5 is

$$\left. \begin{aligned} \frac{d\mathbf{k}_{AB}}{dSL_\beta} &= \frac{d\mathbf{k}_{AB}}{d\gamma_{AB}} \frac{d\gamma_{AB}}{dt} \frac{dt}{dSL_\beta} \\ &= \frac{n\mathbf{k}_{AB}}{\gamma_{AB}} \dot{\gamma}_{AB} \frac{1}{V_w \sin\phi} \\ &= \frac{n\mathbf{k}_{AB}}{S_c} \frac{V_s}{l_{AB}} \frac{1}{V_w \sin\phi} \\ &= \frac{\gamma_{AB}}{S_c n\mathbf{k}_{AB}} \frac{1}{l_{AB}} \end{aligned} \right\} \quad (3.30)$$

Note that shear velocity in the primary shear zone V_s is given by

$$V_s = \frac{V_w \cos\alpha_o}{\cos(\phi - \alpha_o)} \quad (3.31)$$

3.2.2 Plastic Deformation in the Primary Shear Zone

As seen in figure 2.5, slip-line \overline{AB} is assumed to be the line of maximum shear strain and shear strain rate as proposed by Oxley et al [6], [36]. For the given undeformed thickness t_1 , tool rake angle α_o , width of cut w , and cutting speed V_w , shear strain γ_{AB} and shear strain rate $\dot{\gamma}_{AB}$ in the primary shear deformation zone are obtained from the following equations

$$\left. \begin{aligned} \gamma_{AB} &= \frac{\cos\alpha_o}{\sin\phi_s \cos(\phi_s - \alpha_o)} \\ \dot{\gamma}_{AB} &= \frac{\gamma_{AB}}{\Delta t} = \gamma_{AB} \frac{V_s}{l_{AB}} = S_c \frac{V_s}{l_{AB}} \\ V_s &= \frac{V_w \cos\alpha_o}{\cos(\phi_s - \alpha_o)}, \quad l_{AB} = \frac{t_1}{\sin\phi_s} \end{aligned} \right\} \quad (3.32)$$

where α_o , ϕ_s , l_{AB} , V_s are main rake angle of cutting tool, shear angle, length of shear line \overline{AB} , and shear velocity along \overline{AB} . If shear angle varies between $5^\circ \sim 40^\circ$, the average value of strain $\gamma_{AB} \approx 6$, i.e. $S_c \approx 6.0$, is obtained from equation 3.32. Where S_c is designated as an average value used to calculate shear rate $\dot{\gamma}_{AB}$. Oxley et al. [36] observed an average strain value of 5.9 from their experiments.

From Von-Mises yield criterion, shear flow stress (\mathbf{k}_{AB}) distributed along AB in the primary

shear zone is found by

$$\left. \begin{aligned} \sigma_{AB} &= \sigma_1 \epsilon_{AB}^n \\ \epsilon_{AB} &= \frac{\gamma_{AB}}{\sqrt{3}} \\ \mathbf{k}_{AB} &= \frac{\sigma_{AB}}{\sqrt{3}} = \frac{\sigma_1 \epsilon_{AB}^n}{\sqrt{3}} \\ F_s &= \mathbf{k}_{AB} l_{AB} w = \frac{\sigma_1 \epsilon_{AB}^n}{\sqrt{3}} l_{AB} w \end{aligned} \right\} \quad (3.33)$$

where σ_{AB} , n , and F_s are flow stress, strain hardening index, and shear force along the slip-line \overline{AB} , respectively. σ_1 and n are found by evaluating the shear stress, shear strain and strain rate (equations 3.32 and 3.33) from a set of orthogonal cutting tests. The procedures to obtain σ_{AB} and n will be presented in detail later.

During machining, the plastic energy dissipated in the primary shear zone is transformed as heat. To determine shear flow stress \mathbf{k}_{AB} in this zone, temperature, strain rate, and strain are needed. As proposed by Boothroyd [19] and Oxley et al. [6], [36], temperature rise in the primary shear zone is predicted by

$$T_{AB} = T_{room} + \eta \left[\frac{(1 - \lambda_s) F_s \cos \alpha_o}{\rho c t_1 w \cos(\phi - \alpha_o)} \right] \quad (3.34)$$

where T_{room} , ρ and c are initial temperate, density, and the specific heat of work material, respectively. λ_s and η are the empirical factors, which indicate the partial heat conducted into the work material, and the percentage of the deformation takes place on shear plane (AB), respectively. The values of the constants evaluated from orthogonal cutting tests are given in the Appendix A. Oxley [6] suggested that better estimations of temperature rise in the primary shear zone T_{AB} is obtained when η is taken between 0.75 and 0.95, which is supported by the finite element analysis results reported by Tay et al. [73].

The following sections will show that the iterated procedures for the calculation of the mean temperature in the primary shear zone is required since thermal conductivity κ and specific heat c are temperature dependent.

The analysis of energy balance is introduced in this model. Unlike Oxley's approach [6], shear angle will be predicted by using minimum energy method instead of graphical method. Energy consumed in machining is composed of two source, namely, energy dissipations in the primary shear deformation and secondary deformation at the tool-chip interface zones. The energy dissipation in the primary shear deformation zone E_s is determined from the strain energy given by

$$\left. \begin{aligned} E_s &= \int_0^{\epsilon_{AB}} \sigma d\epsilon = \frac{\sigma_1}{n+1} (\epsilon_{AB})^{n+1} \\ &= \frac{\sigma_1}{n+1} \left[\frac{\cos \alpha_o}{\sqrt{3} \sin \phi \cos(\phi - \alpha_o)} \right]^{n+1} \end{aligned} \right\} \quad (3.35)$$

It can be seen that the energy consumed in the primary shear zone (E_s , J/mm³) is influenced by strain hardening (n), flow stress (σ_1), tool rake angle (α_o), and shear angle (ϕ). "Classical shear plane" models [21], [22] assumed ideal plastic deformation without strain hardening in the chip formation. Therefore, their models can not account for the effect of strain hardening.

3.2.3 Plastic Deformation in the Tool-Chip Interface Zone

Chip is formed by the shearing action in shear zone during the machining. Severe friction occurs in the contact area between the chip and the cutting tool. Zorev [28] suggested that the real contact area is equal to the apparent for part of the contact length under most cutting conditions. It was found that sticking friction prevails around the cutting edge and sliding friction occurs around the end of contact area between the tool and the chip. Boothroyd et al. [60] suggested that both the coefficient of sticking friction and the coefficient of sliding friction are constants. The mean coefficient of friction between the tool rake face and the chip is found to be variable, depending on the normal stress distribution on the tool rake face and shear stress at the tool-chip interface. The plastic flow zone of intense shear strain near the tool-chip interface are normally observed [45]. The existing knowledge about stresses distribution at

$$\left. \begin{aligned} \dot{\gamma}_{inter} &= \frac{V_c}{\delta \cdot t_2} \\ V_c &= \frac{V_w \sin \alpha_o}{\cos(\phi - \alpha_o)} \\ t_2 &= \frac{t_1 \cos(\phi - \alpha_o)}{\sin \phi} \end{aligned} \right\} \quad (3.36)$$

where V_c and t_2 are the chip velocity and the chip thickness, respectively. δ is the ratio of thickness of plastic deformation layer at the tool-chip interface to the chip thickness t_2 . The average thickness of the plastic layer is measured from cut chips (P20) with Scanning Electron Microscope (SEM), and found to be about 5% of the measured chip thickness. Same observation was reported by Tay et al. [73] and Stephenson [37].

Severe plastic deformation and friction in the tool-chip interface causes high temperature rise compared to that in the primary shear zone. Tool life is directly affected by the temperature loading in this zone. The analysis of temperature in tool-chip interface zone is included in the model development since flow stress of work material varies with temperature at the tool-chip interface. Applying the same approach as proposed by Oxley et al. [6], [36], [73], the temperature rise at the tool-chip interface is determined by

$$T_{inter} = T_{AB} + \psi \Delta T_M \quad 0 < \psi < 1.0 \quad (3.37)$$

where ΔT_M is the maximum temperature rise in the chip which occurs at the interface and ψ is a factor which allows for the variations of temperature along the interface. T_{AB} is the temperature evaluated in the primary shear zone. ΔT_M is determined from equations shown in Appendix A. The determination of temperature is considered by assuming heat generated in a finite plastic deformation zone (δt_2) instead of plane heat source along the tool-chip interface. Noted that an iterative procedure is required in order to calculate temperature rise at the tool-chip interface because thermal properties κ , c , are also temperature dependent.

The chip-tool contact length (l_c) is required to evaluate the friction energy produced on

the rake face. Gad and Armarego et al. [35] reviewed the literature, and concluded that the most adequate method of contact length estimation is to use empirical models calibrated from machining tests. In this chapter, the contact length (l_c) along the tool-chip interface is identified from machining tests, where l_c is calibrated as a function of cutting speed and feedrate. The equation will be shown later. Since the stresses distribution along the tool-chip interface is assumed, hence, the area of shear load on the rake face gives the total friction force exerted at the tool-chip interface

$$F_{fc} = \mathbf{k}_{inter} \frac{l_c}{2} w + \frac{1}{2} \mathbf{k}_{inter} \frac{l_c}{2} w = \frac{3}{4} \mathbf{k}_{inter} l_c w \quad (3.38)$$

where \mathbf{k}_{inter} is the shear flow stress and equal to $\mathbf{k}_{inter} = \frac{\sigma_{inter}}{\sqrt{3}}$. The flow stress at tool-chip interface σ_{inter} is mapped from the velocity modified temperature T_{mtc} , which is given in Appendix B. The energy per unit volume dissipated in tool-chip interface zone E_{inter} is found by

$$\left. \begin{aligned} E_{inter} &= \frac{F_{fc} V_c}{V_w t_1 w} \\ &= \frac{3\mathbf{k}_{inter} l_c w V_w \sin\phi}{4t_1 w V_w \cos(\phi - \alpha_o)} \\ &= \frac{3\sigma_{inter} l_c w V_w \sin\phi}{4\sqrt{3} t_1 w V_w \cos(\phi - \alpha_o)} \\ &= \frac{3\sigma_{inter} l_c \sin\phi}{4\sqrt{3} t_1 \cos(\phi - \alpha_o)} \end{aligned} \right\} \quad (3.39)$$

where V_c is the chip velocity given by equation 3.36.

3.3 Experimental Modeling

This section describes the experimental setup for orthogonal machining of P20 mold steel. A

set of orthogonal machining tests have been performed under a wide range of cutting conditions. The chip thickness t_2 , cutting force F_c , feed force F_t , and contact length l_c are measured from experiments. Tool wear tests for cutting with sharp tools also have been conducted. Similar to a transfer function to govern the relation between inputs and outputs of a dynamic system, the correlation of flow stress σ_1 , flow stress σ_{inter} , and strain hardening index n are identified through machining tests. The flow stress of P20 work material under high strain rate and temperature identified from machining with sharp tools is also applied in the modeling of machining with chamfered tools as shown in chapter 4.

Table 3.1: Chemical composition of P20 mold steel

Approximate composition%	C	S_i	M_n	C_r	N_i	M_o	S
	0.37	0.3	1.4	2.0	1.0	0.2	0.08
Standard specification	AISI P20 Modified						
Delivery condition	Hardness 321 HB, 35 HRC						

3.3.1 Experimental Setup

Figure 3.4 shows the schematic representation of the experimental setup used in this thesis. The experimental system consists of P20 workpiece, cutting tools, data acquisition components, and CNC turning center. The work material used in machining tests is P20 mold steel. Table 3.1 and 3.2 show the chemical compositions and general mechanical properties.

In the machining tests, P20 work material was made as a disk with outer diameter about 98.90 mm and thickness of 3.6 mm. All disk specimens were ground to keep accurate thickness

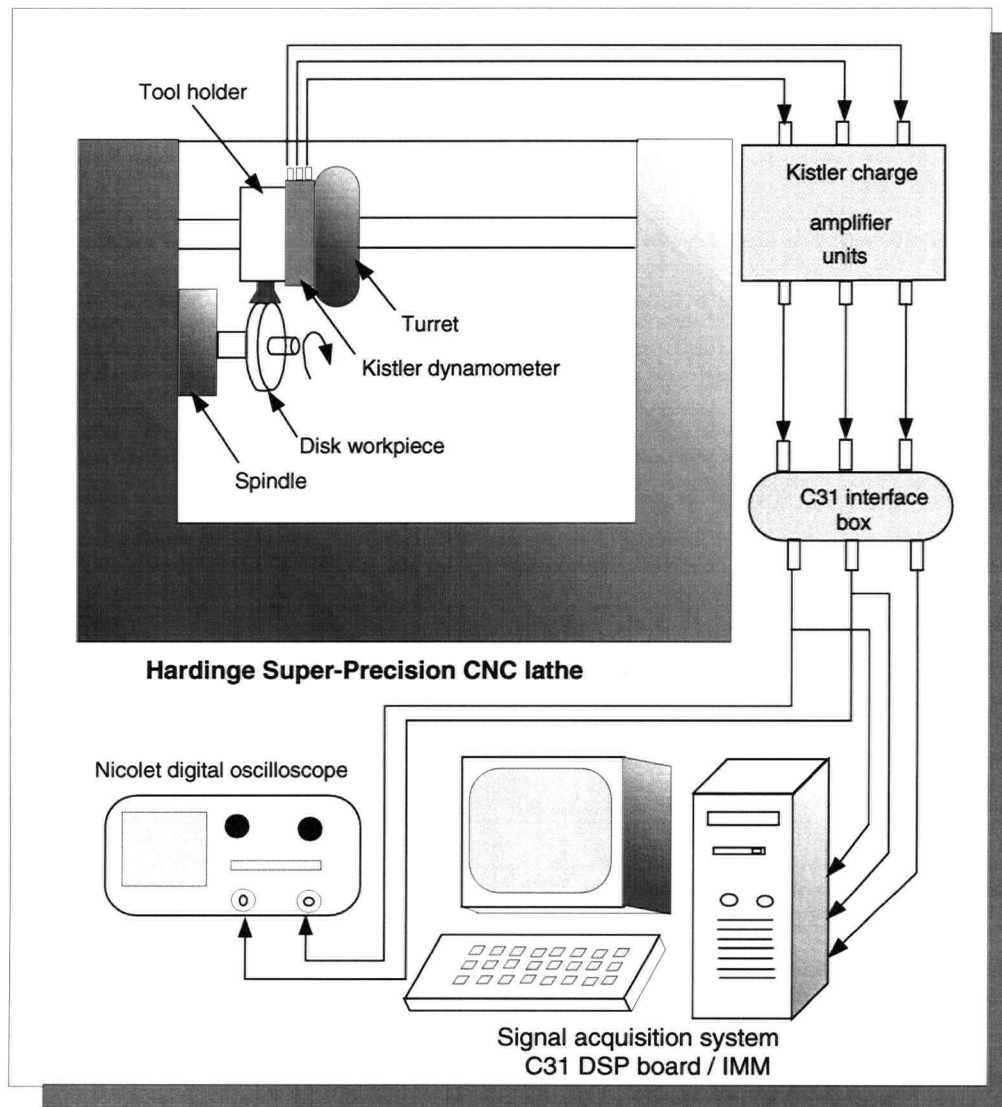


Figure 3.4: Diagram of experimental setup for orthogonal machining of P20 mold steel

Table 3.2: Mechanical properties of P20 Mold steel

Temperature	20° C	200° C	400° C
Density Kg/m^3	7800	7750	7700
Thermal conductivity $J/m s ^\circ C$	29.0	29.5	31.0
Modulus of elasticity GPa	205	200	185
Specific heat $J/Kg ^\circ C$	460	-	-

within tolerance of about $5.0 \mu m$. Figure 3.7 shows the dimension of the disk workpiece prepared for machining tests. The disk workpiece is connected with a shaft by two bolts. The shaft is clamped to the spindle by the collet of machine tool.

Figure 3.5 shows the dimension of the shaft used in the experiment. Initially, some disks were made with the average thickness about 5.0 mm for some cutting tests. Blank carbide insert made by SANDVIK (N151.2-650-50-3B) with grade number S10 were used in the machining tests. This type of tool has the basic geometry as shown in figure 3.8. All of them have zero degree rake angle and 10° clearance angle. These tools are prepared as orthogonal cutting with sharp tools. Figure 3.6 shows the Hardinge Super-Precision SUPERSLANT CNC turning center.

All cutting tests have been conducted using the same setup. CNC turning center can be programmed to provide the constant surface speed due to the changes of utter diameter of disk workpiece. For the desired cutting speed, the corresponding spindle speed N is determined by

$$N = \frac{1000 V_w}{\pi D} \quad (3.40)$$

where D (mm) is the diameter of disk workpiece, V_w (m/min) is the cutting speed. Data acquisition system consists of a Kisler three component piezo-electric 9257A dynamometer mounted on the turret, 5004 Dual Mode charge amplifiers, DSP external interface box, a PC supported by IMM real time signal processing software, which is developed by Manufacturing Automation Laboratory at University of British Columbia, and NIC-310 digital oscilloscope for signal monitoring.

3.3.2 Experimental Procedures

The orthogonal machining tests have been conducted under the cutting conditions as shown in table 3.3. A conventional parting process was applied with the main cutting edge of the tool set normal to the feed force. This setup makes machining as orthogonal cutting process.

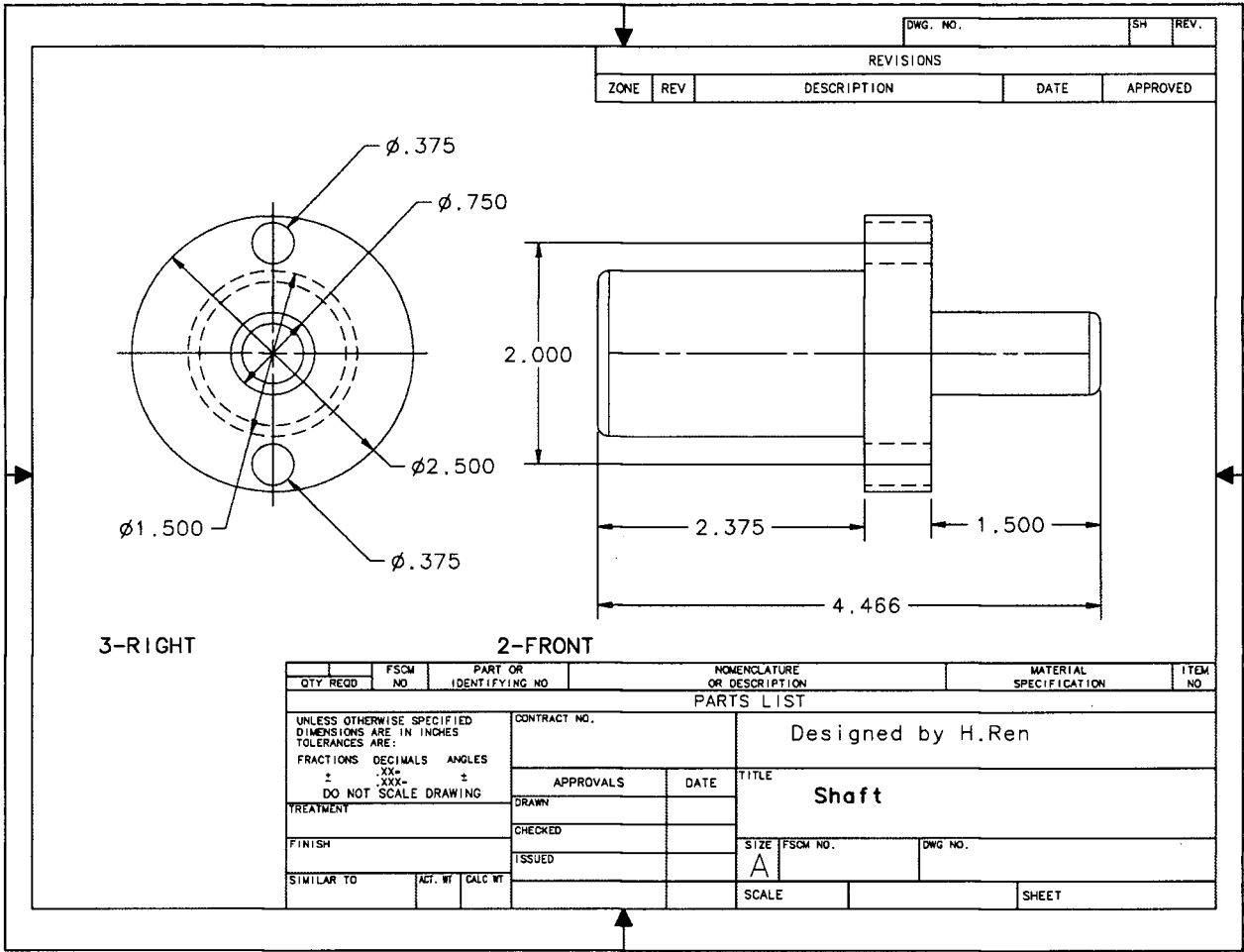


Figure 3.5: Shaft used in machining tests



Figure 3.6: Hardinge CNC turning center used in machining tests

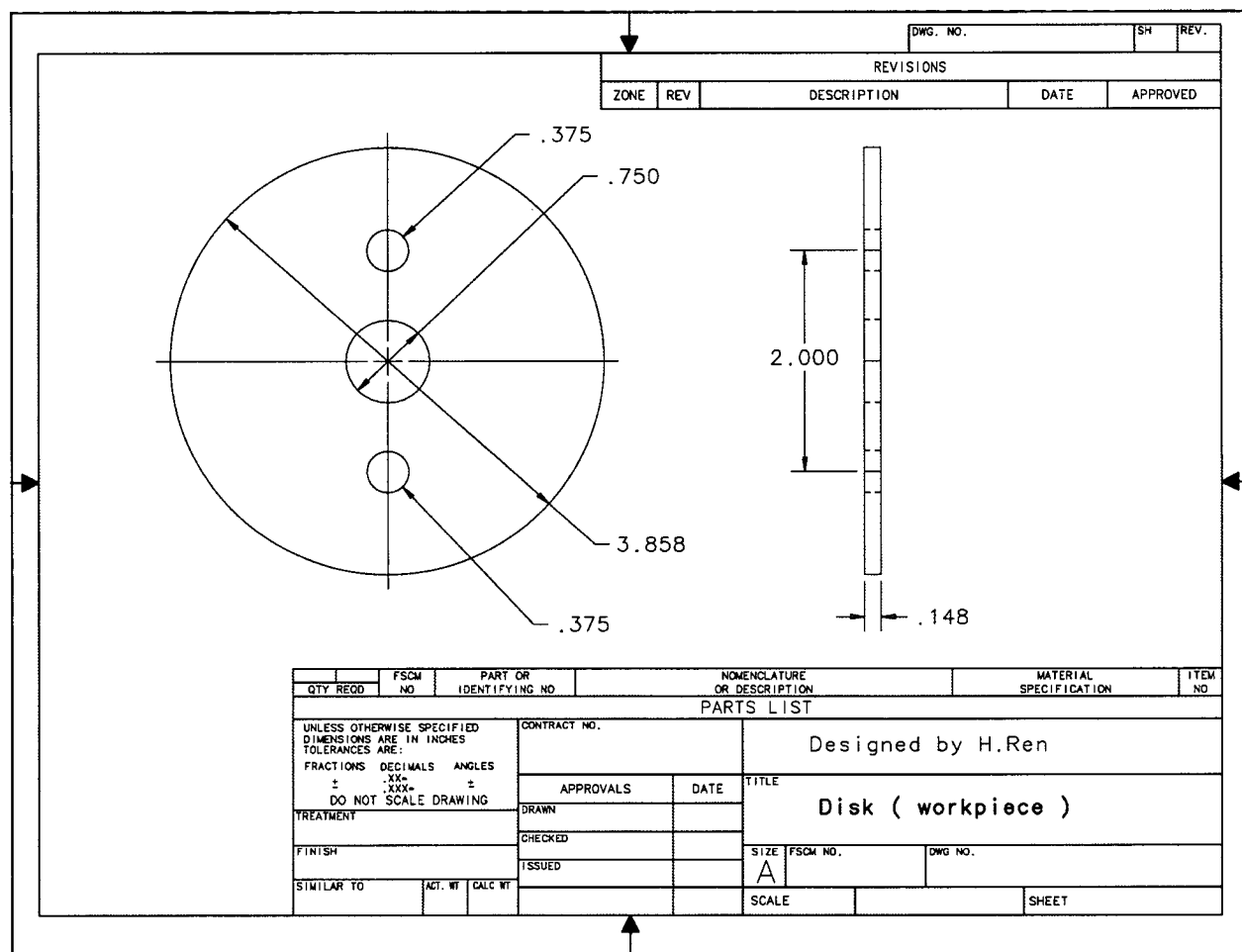


Figure 3.7: Workpiece used in machining tests

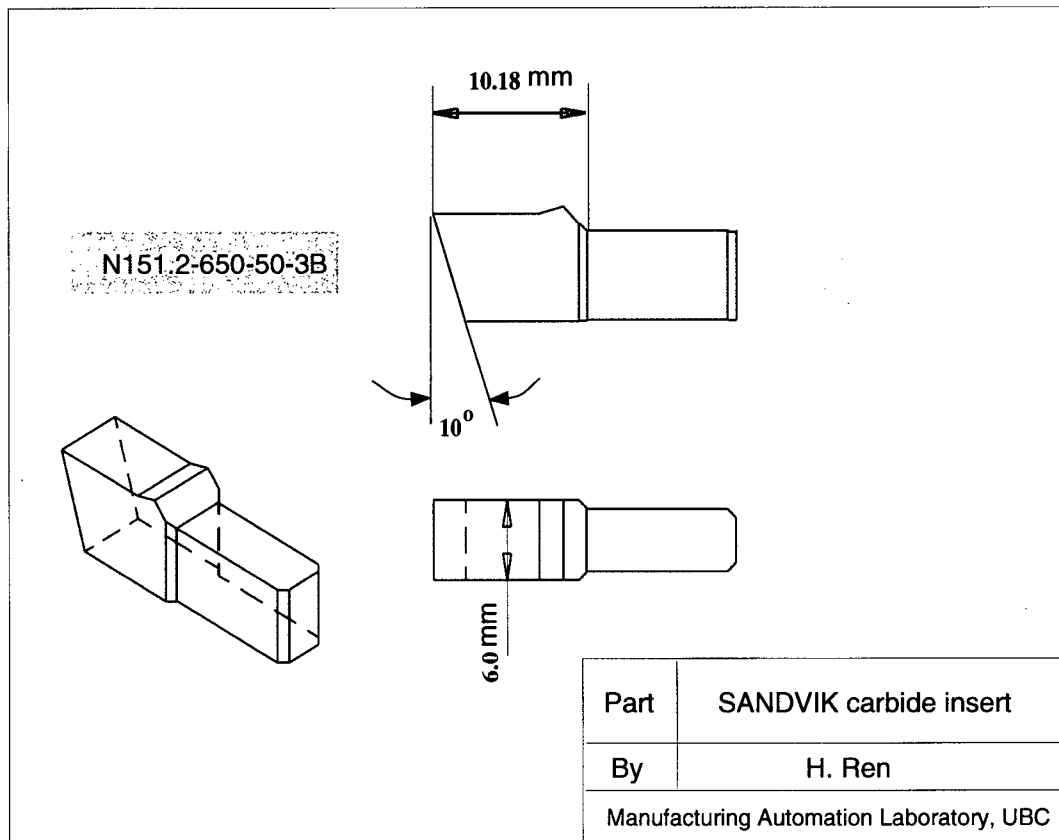


Figure 3.8: SANDVIK carbide insert

Cutting forces are found by averaging the forces recorded from experiments. The chip-rake face contact length was measured with a tool microscope for each test. The chips are collected, their thicknesses are measured. The weight of chip sample is measured by an electronic scale. Then, chip thickness t_2 is determined by equation 3.41, where h is the length of a small piece of chip sample, ρ is density of P20 mold steel, and w_g is the weight of a small piece of chip sample, respectively.

Table 3.3: Cutting conditions

Feedrate mm/rev		Cutting speed m/min
w=3.6 mm	0.02, 0.04, 0.06, 0.08, 0.10	100, 240, 380, 600
w=5.0 mm	0.02, 0.03, 0.04, 0.05, 0.06, 0.07, 0.08, 0.09	60, 120, 240, 380, 600
w=5.0 mm	0.04	60, 120, 200, 240, 380, 480, 600, 780, 1000, 1200

$$t_2 = \frac{w_g}{\rho h w} \quad (3.41)$$

Then, experimental shear angle is determined from the calculated chip ratio r_c

$$r_c = \frac{t_1}{t_2} \quad (3.42)$$

$$\phi = \tan^{-1} \frac{r_c \cos \alpha_o}{1 - r_c \sin \alpha_o} \quad (3.43)$$

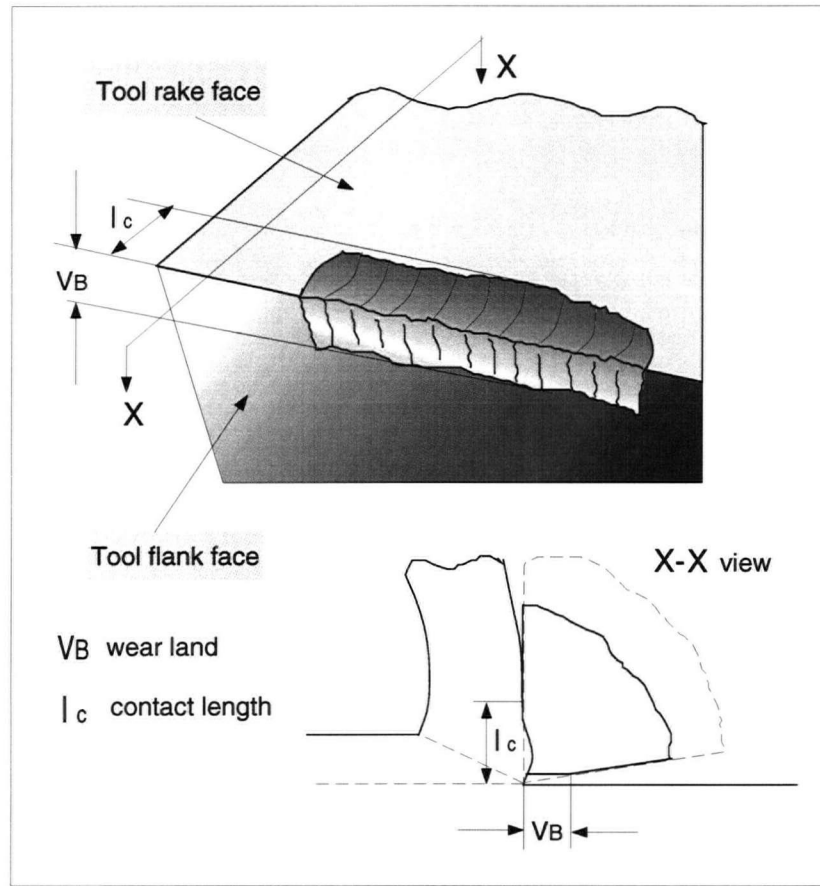


Figure 3.9: Illustration of measurement of contact length l_c and tool wear land VB from the cutting tool

From experimental cutting force measurement, the mean coefficient of friction at tool-chip interface is given by

$$\tan\beta = \frac{(F_t - F_{te}) + (F_c - F_{ce})\tan\alpha_o}{(F_c - F_{ce}) - (F_t - F_{te})\tan\alpha_o} \quad (3.44)$$

where F_c and F_t are measured cutting force and feed force, F_{ce} and F_{te} are edge force components in cutting and feed directions, respectively. The detail of the identification of edge force components F_{ce} and F_{te} is shown in Appendix C.

A scar remains on the rake surface of cutting tool due to severe friction acting at the tool-chip interface. Cutting tools get worn after certain machining time, which ultimately leads to the breakage of cutting tool. The stress distribution at the tool-chip interface is affected directly by the contact length. In experiments, the contact length l_c is measured with a tool maker microscope. Figure 3.9 illustrates the experimental method to determine the contact length l_c and tool wear land VB after each cutting test. The correlation of contact length l_c with undeformed chip thickness t_1 and cutting speed V_w is shown in figure 3.10. It can be seen that contact length along the tool-chip interface varies with cutting speed and uncut chip thickness. Based on the experimental observation, the contact length l_c is estimated from the correlation with the cutting speed V_w and undeformed chip thickness t_1 .

$$l_c = 0.2432 - 0.313 \times 10^{-8} V_w^3 + 0.47 \times 10^{-5} V_w^2 - 0.00198 V_w - 2.3499 t_1^2 + 3.2 t_1 \quad (3.45)$$

Table 3.4 and 3.5 show the data obtained from machining tests. Next section will demonstrate how to establish the material constitutive relation of flow stress and strain hardening exponent under a range of strain and strain rate from the machining test data. The proposed procedures involve the mapping of flow stress and strain hardening exponent from strain, strain rate, and velocity modified temperature which are obtained from machining tests.

It is noted that cutting force F_c' and feed F_t' shown in table 3.4 and 3.5 are given by subtracting edge forces F_{ce} and F_{te} (see in Appendix C) from the measured total cutting force F_c and feed force F_t . Figure 3.11 shows variation of shear stress with cutting speed and undeformed chip thickness. Experimental shear stress k_{AB} is calculated from measured forces F_c' and F_t'

$$k_{AB} = \frac{[F_c' \cos \phi - F_t' \sin \phi] \sin \phi}{t_1 w} \quad (3.46)$$

where ϕ is experimental shear angle found from equation 3.43.

Table 3.4: Machining test data (“sharp tool”), $w=3.6$ mm

$t_1(\text{mm})$	$V_w(\text{m/min})$	$F_c'(\text{N})$	$F_t'(\text{N})$	$\phi(\text{rad})$	$l_c(\text{mm})$
0.02	100.0	125.07	41.40	0.236	0.135
0.02	240.0	119.91	27.86	0.370	0.095
0.02	380.0	128.43	39.99	0.405	0.096
0.02	600.0	149.08	60.30	0.433	0.097
0.04	100.0	315.08	147.57	0.299	0.194
0.04	240.0	276.90	83.020	0.448	0.155
0.04	380.0	304.85	88.380	0.495	0.150
0.04	600.0	320.98	161.22	0.502	0.179
0.06	100.0	459.46	199.20	0.366	0.290
0.06	240.0	414.80	114.11	0.511	0.177
0.06	380.0	453.88	135.89	0.518	0.185
0.06	600.0	479.63	204.18	0.523	0.334
0.08	100.0	592.30	248.65	0.420	0.336
0.08	240.0	563.98	159.09	0.519	0.230
0.08	380.0	593.01	180.29	0.518	0.212
0.08	600.0	633.73	302.48	0.534	0.334
0.10	100.0	731.82	302.80	0.447	0.410
0.10	240.0	635.18	182.30	0.539	0.252
0.10	380.0	730.69	214.68	0.551	0.283
0.10	600.0	777.73	314.18	0.571	0.430

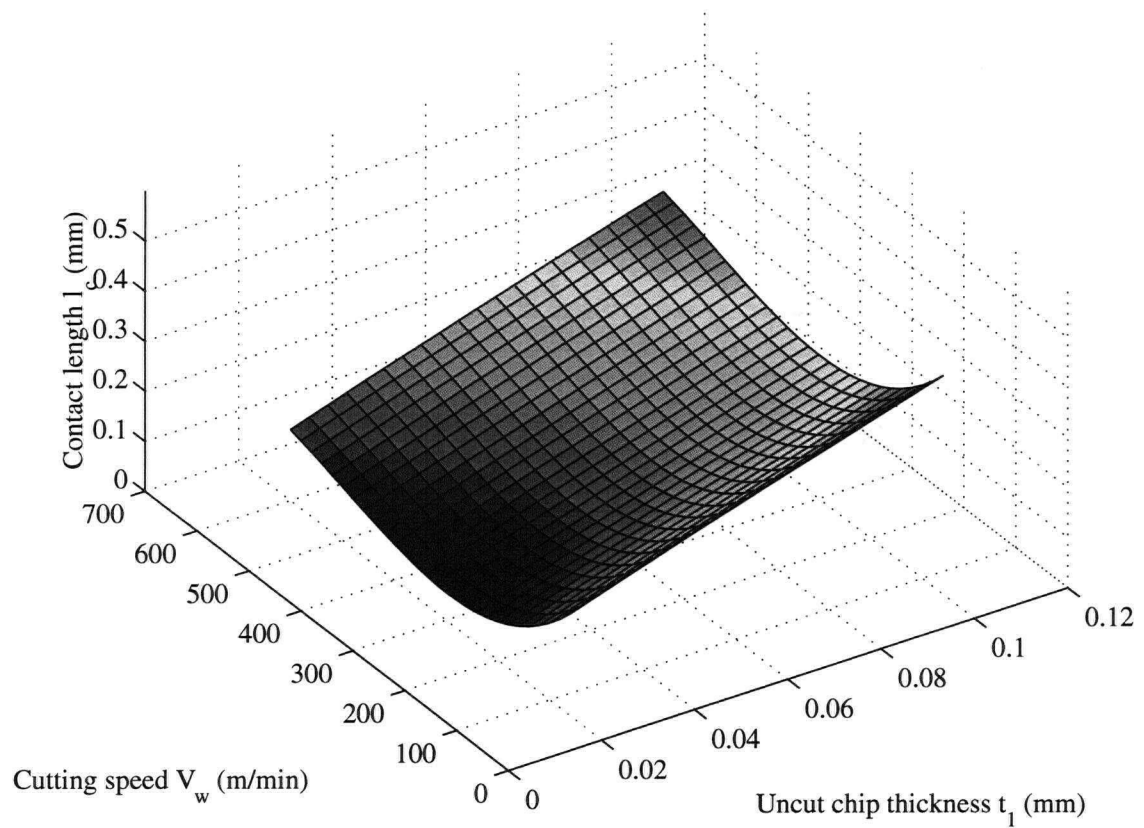


Figure 3.10: Plot of correlation of contact length with cutting speed V_w and undeformed chip thickness t_1 , $w=3.6$ mm.

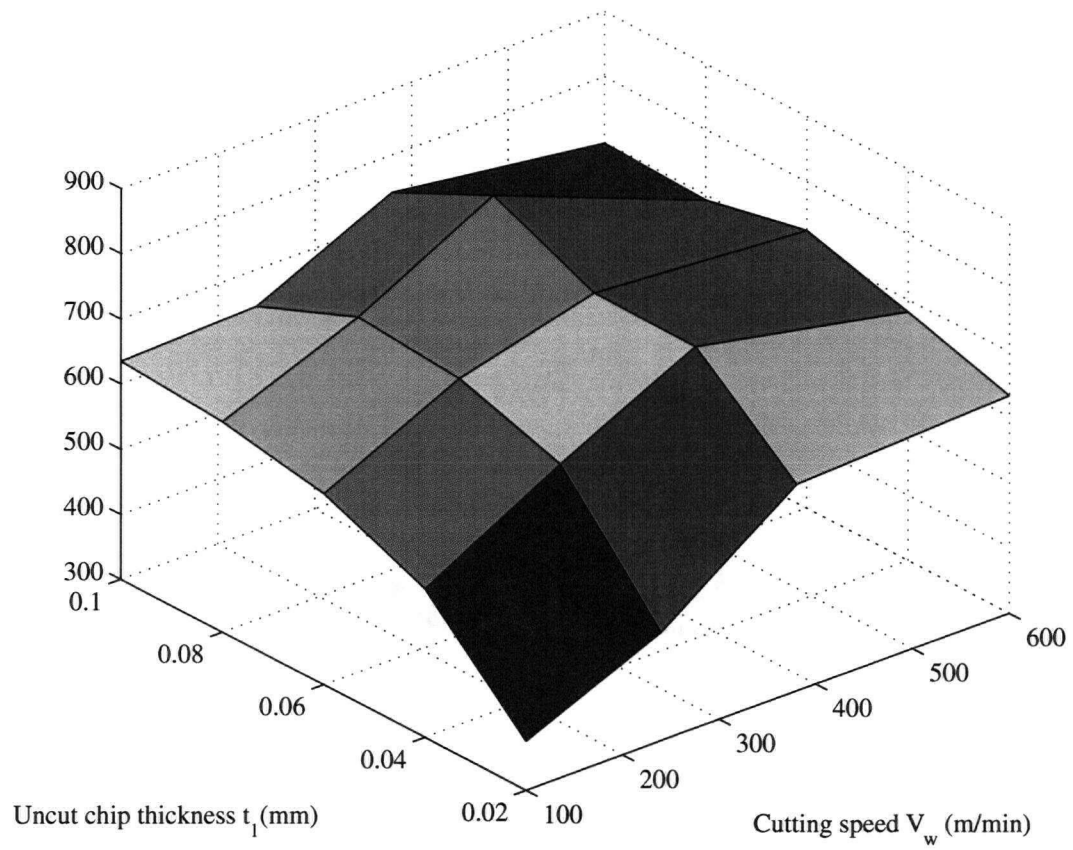


Figure 3.11: Plot of correlation of shear stress on the shear plane with cutting speed V_w and undeformed chip thickness t_1 , $w=3.6$ mm.

Table 3.5: Machining test data (“sharp tool”), $w=5.0$ mm

t_1 (mm)	V_w (m/min)	F_c' (N)	F_t' (N)	ϕ (rad)	l_c (mm)
0.04	60.00	632.44	381.82	0.257	0.370
0.04	120.0	530.14	352.42	0.425	0.196
0.04	200.0	447.64	233.00	0.488	0.129
0.04	240.0	416.00	208.29	0.497	0.114
0.04	380.0	448.20	140.20	0.527	0.118
0.04	480.0	396.33	117.50	0.537	0.124
0.04	600.0	520.90	204.10	0.540	0.132

3.3.3 Modeling of Flow Stresses and Strain Hardening Under High Strain Rate and Temperature Through Machining Tests

When applying “shear zone” model proposed by Oxley et al. [6], [36], a reliable material constitutive equation is required. The flow stress of work material obtained from high speed compression tests was used in Oxley’s model. This section presents a method to model the flow stresses in the primary shear and secondary deformation zones in detail. A number of C programs were developed to facilitate this effort. From machining test data shown in tables 3.4 and 3.5, shear angles, mean friction coefficients at the tool-chip interface, and shear stresses in the primary shear and the tool-chip interface zones are evaluated and the corresponding strain rate and temperature are evaluated as well. Hence, empirical constitutive equations for P20 work material are obtained.

The procedures are summarized as follows:

- Input a cutting test data file, which contains given undeformed chip thickness t_1 (mm), cutting speed V_w (m/min), cutting forces F_c' and F_t' (N), shear angle ϕ (rad), and measured contact length l_c (mm).

- Calculate the shear strain γ_{AB} and shear strain rate $\dot{\gamma}_{AB}$ in the primary shear zone, using equation 3.32.
- Calculate the shear strain rate $\dot{\gamma}_{inter}$ in the tool-chip interface zone, using equation 3.36.
- Calculate temperature rise in the primary shear zone T_{AB} and in the tool-chip interface zone T_{inter} shown in Appendix A.
- Determine the mean friction coefficient at the tool-chip interface $\tan(\beta)$, angle (θ) between resultant force R_s and slip-line \overline{AB} , and strain hardening index n .
- Calculate shear stress k_{AB} , and then σ_1 is found from equations 3.33.
- Calculate shear stress k_{inter} acting along the tool-chip interface.

The mean friction angle β is determined by

$$\beta = \alpha_o + \tan^{-1}\left(\frac{F'_t}{F'_c}\right) \quad (3.47)$$

where F'_c and F'_t are the cutting and feed forces, which are obtained by subtracting the edge forces from the measured cutting and feed forces. The angle θ which indicates the angle between the resultant force R_s and slip-line \overline{AB} in the primary shear zone as seen in figure 2.5 is found from equation

$$\theta = \phi + \beta - \alpha_o \quad (3.48)$$

As shown previously in equation 3.20, the variation of hydrostatic stress p along slip line \overline{AB} in figure 2.5 is

$$\Delta p = \frac{\Delta k_{AB}}{\Delta SL_\beta} \Delta SL_\alpha \quad (3.49)$$

$$p_A - p_B = \frac{\Delta k_{AB}}{\Delta SL_\beta} \Delta SL_\alpha \quad (3.50)$$

Palmer and Oxley [61] analyzed the slip-line along \overline{AB} and they suggested that this slip-line must in fact bend near the free surface at 45° . From Hencky's equation 3.16, this yields

$$p_A = k_{AB}[1 + 2(\frac{\pi}{4} - \phi)] \quad (3.51)$$

From geometrical relation as shown in figure 2.5, θ is given by

$$\tan\theta = \frac{F_{ns}}{F_s} = \frac{(p_A + p_B)/2}{k_{AB}} \quad (3.52)$$

According to the theory proposed by Oxley et al. [6], substituting equations 3.50, 3.51, and 3.30 into equation 3.52 gives

$$\tan\theta = [1 + 2(\frac{\pi}{4} - \phi)] - \frac{S_c n k_{AB} l_{AB}}{2 l_{AB} k_{AB}} = [1 + 2(\frac{\pi}{4} - \phi)] - \frac{S_c n}{2} \quad (3.53)$$

where $S_c \approx 6.0$ and l_{AB} is length of \overline{AB} given by

$$l_{AB} = \frac{t_1}{\sin\phi} \quad (3.54)$$

From equation 3.53, the average strain hardening index n in the primary shear zone is obtained

$$n = \left[\frac{1 + 2(\frac{\pi}{4} - \phi) - \tan\theta}{S_c} \right] \quad (3.55)$$

To determine the cutting temperature in the primary shear zone and the secondary deformation zone at the tool-chip interface, an iterative procedure is again applied to calculate cutting temperatures T_{AB} and T_{inter} since material properties, such as specific heat c and thermal conductivity κ , are temperature dependent. Figure 3.12 shows an algorithm to evaluate cutting temperature T_{AB} and T_{inter} . T_{room} is the initial temperature of work material or room temperature. The coefficient λ_s is determined from equations shown in Appendix A. The evaluation of temperature on the shear plane and the tool-chip interface zone is carried out using experimentally identified shear angle (ϕ), shear stress (k_{AB}), and friction coefficient ($\tan\beta$). As proposed by Oxley and his coworkers [6], velocity modified temperature T_{mod} is introduced to combine

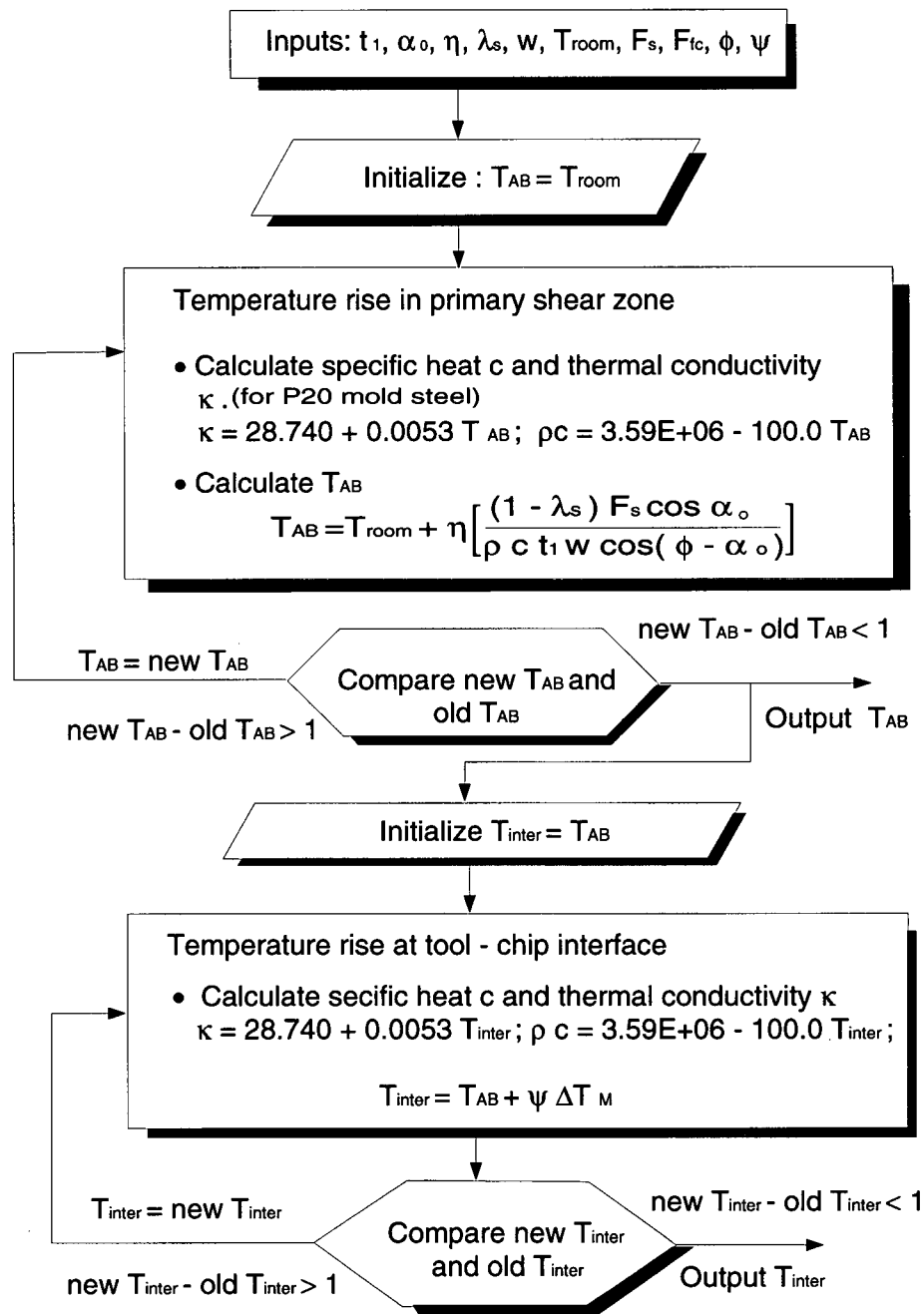


Figure 3.12: An algorithm of the cutting temperature estimation

Table 3.6: Flow stress σ_1 , strain hardening index n , cutting temperature T_{AB} obtained from machining test data

t_1 (mm)	V_w (m/min)	w (mm)	n	σ_1 (MPa)	T_{AB} (°C)	T_{mod} (K)	γ_{AB}	$\dot{\gamma}_{AB}$ (1/s)
0.02	100.0	3.60	0.25	594.35	186.05	259.25	4.39	118733.70
0.02	240.0	3.60	0.195	911.63	242.55	263.94	2.97	458321.87
0.02	380.0	3.60	0.153	1004.5	274.58	268.31	2.76	803442.13
0.02	600.0	3.60	0.108	1144.9	323.37	279.83	2.62	1368179.8
0.04	100.0	3.60	0.181	907.35	270.13	316.26	3.56	75792.602
0.04	240.0	3.60	0.130	1156.8	309.31	309.02	2.56	283897.34
0.04	380.0	3.60	0.101	1342.7	351.55	317.33	2.39	505902.38
0.04	600.0	3.60	0.019	1188.3	330.12	295.30	2.37	812019.50
0.06	100.0	3.60	0.146	1048.1	292.29	333.29	2.99	62882.582
0.06	240.0	3.60	0.095	1245.4	321.12	321.11	2.34	220972.19
0.06	380.0	3.60	0.083	1341.9	354.65	327.56	2.33	355570.53
0.06	600.0	3.60	0.033	1272.9	352.45	314.94	2.31	568470.81
0.08	100.0	3.60	0.112	1109.3	300.07	340.86	2.68	55045.316
0.08	240.0	3.60	0.088	1268.9	331.53	333.10	2.32	168772.91
0.08	380.0	3.60	0.081	1309.9	353.61	334.07	2.26	266665.50
0.08	600.0	3.60	0.003	1199.8	340.25	315.12	2.28	436658.88
0.10	100.0	3.60	0.096	1131.8	308.48	349.37	2.57	47182.918
0.10	240.0	3.60	0.072	1149.7	302.42	321.02	2.27	141523.42
0.10	380.0	3.60	0.061	1319.6	352.76	337.22	2.24	230122.25
0.10	600.0	3.60	0.003	1261.6	351.16	324.16	2.20	379428.41

the effect of strain rate and cutting temperature on the flow stress σ_{inter} at the tool-chip interface zone.

The velocity modified temperature in tool-chip interface zone T_{modint} is given by

$$T_{modint} = (T_{inter} + 273.0)(1 - \nu \log_{10} \dot{\epsilon}_{inter}) \quad (K) \quad (3.56)$$

where T_{inter} is temperature rise in secondary deformation zone at the tool-chip interface, and ν is material constant. For the steels, MacGregor and Fisher [20] found that ν is about 0.09. $\dot{\epsilon}_{inter}$ is strain rate in the secondary deformation zone. $\dot{\epsilon}_{inter}$ is equal to $\dot{\gamma}_{inter} / \sqrt{3}$ as explained before.

Flow stresses (σ_1 and σ_{inter}), strain hardening index n , strain rate ($\dot{\gamma}_{AB}$ and $\dot{\gamma}_{inter}$), and cutting temperature (T_{AB} and T_{inter}) are identified from machining test data as shown in tables 3.6 and 3.7. Flow stress exerted along the tool-chip interface is given by

$$k_{inter} = \frac{4 F_{fc}}{3 l_c w} \quad (3.57)$$

where F_{fc} is mean friction force acting along the tool-chip interface. F_{fc} is found by

$$F_{fc} = R_s \sin \beta = \frac{k_{AB} l_{AB} w \sin \beta}{\cos \theta} \quad (3.58)$$

The empirical constitutive equations obtained from machining data will be used to determine flow stress associated with cutting process in the following sections. For the machining process, most of cutting energy is consumed in the primary shear deformation zone. The strain γ_{AB} and strain rate $\dot{\gamma}_{AB}$ are found to vary with the scale and speed of deformation defined by the undeformed chip thickness t_1 and cutting speed V_w (see the table 3.4). It is reasonably assumed that flow stress σ_1 is mainly affected by the strain and strain rate in the primary shear deformation zone. Therefore, empirical equations to establish the mapping of flow stress σ_1

Table 3.7: Flow stress σ_{inter} , cutting temperature T_{inter} obtained from machining test data

t_1 (mm)	V_w (m/min)	w (mm)	$\dot{\gamma}_{inter}$ (1/s)	σ_{inter} (MPa)	T_{inter} (°C)	T_{modint} (K)
0.02	100.0	3.60	97003.532	147.98	246.62	297.56
0.02	240.0	3.60	602239.75	141.54	335.92	305.24
0.02	380.0	3.60	1168867.0	199.58	447.54	342.52
0.02	600.0	3.60	2146715.8	300.64	654.88	419.04
0.04	100.0	3.60	79053.859	365.98	466.98	429.67
0.04	240.0	3.60	462147.88	257.86	543.37	417.68
0.04	380.0	3.60	926871.06	283.66	682.01	462.65
0.04	600.0	3.60	1512345.8	433.33	1007.5	595.82
0.06	100.0	3.60	81624.687	330.48	532.48	466.70
0.06	240.0	3.60	419976.19	309.30	637.36	469.19
0.06	380.0	3.60	686797.43	353.41	808.78	536.04
0.06	600.0	3.60	1111797.8	294.12	992.46	604.04
0.08	100.0	3.60	83395.046	355.94	597.27	503.51
0.08	240.0	3.60	326658.25	332.21	714.75	518.76
0.08	380.0	3.60	515050.09	408.96	898.93	594.64
0.08	600.0	3.60	874647.00	435.72	1257.1	744.68
0.10	100.0	3.60	76591.242	355.32	644.67	533.98
0.10	240.0	3.60	287114.31	348.74	725.04	529.20
0.10	380.0	3.60	479449.68	364.72	932.14	614.87
0.10	600.0	3.60	825501.56	351.53	1221.3	730.66

and strain hardening index n from strain and strain rate in the primary shear zone are obtained as shown in Appendix B.

Since temperature at the tool-chip interface is very high when cutting speed reaches certain value, strain hardening becomes insignificant in this zone. Oxley et al. [6], [36] also suggested that the strain hardening can be neglected due to very high strain existing at tool-chip interface. In this thesis, the mapping flow stress at the tool-chip interface σ_{inter} from the velocity modified temperature T_{modint} is proposed, see Appendix B.

Figure 3.13 (data from tables 3.6, 3.7) reveals the variations of experimental strain γ_{AB} , strain hardening index n , strain rate $\dot{\gamma}_{AB}$, flow stress σ_1 , and temperature rise in the primary shear deformation zone T_{AB} and the tool-chip interface zone T_{inter} with the cutting speed V_w and undeformed chip thickness t_1 in machining of P20 mold steel.

From figure 3.13, the following features are observed

- For the increase of cutting speed V_w , this involves a increase of deformation speed. Therefore, the strain rate is directly proportional to the cutting speed, so does the cutting temperature at the tool-chip interface. Temperature rise in the primary shear deformation zone show a slight increase due to the effect of adiabatic. Temperature rise in both primary shear and tool-chip secondary deformation zones causes strain softening. Strain hardening index n in the primary shear zone tends to decrease with the increase of cutting speed.
- For the increase of undeformed chip thickness t_1 , this involves the increase deformation scale. flow stress is seen to increase. As a result, strain γ_{AB} , strain rate $\dot{\gamma}_{AB}$, and strain hardening index n decrease since the increase of temperature also leads to reduce strain hardening.

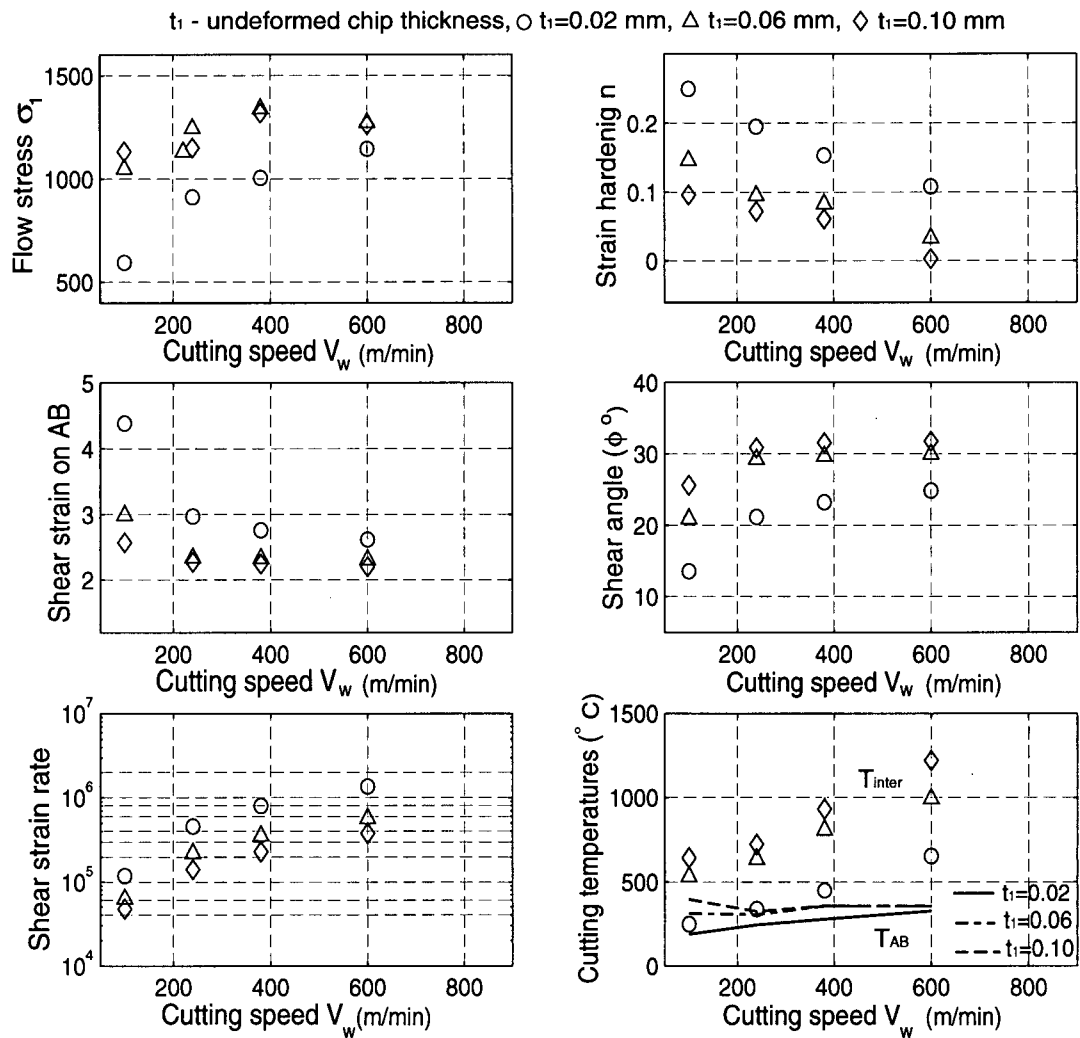


Figure 3.13: Flow stress, strain hardening index, shear strain, shear strain rate, and cutting temperature versus different cutting conditions

3.4 Prediction of Cutting Process with Sharp Tools

Oxley et al. [36] initiated the analysis of machining process from work material properties and cutting conditions. Their theory accounts for the influence of cutting conditions on the flow stress, strain hardening, and strain rate. However, the determination of material properties under large plastic deformations are difficult to obtain from the standard material tests. Especially, high speed machining is characterized by very high strain rate and high temperature, which is hardly to evaluate from the conventional material tests. There are very few material test data under high strain rate and high temperature for P20 mold steel available in the literature. In this thesis, material constitutive relation for P20 work material is modeled through high speed orthogonal machining tests as demonstrated in the previous section. The Minimum Energy Principle is applied to predict shear angle for given cutting conditions and tool geometry through the model development. This section illustrates the procedures for the prediction of cutting process with sharp tools in detail.

3.4.1 A Minimum Energy Approach

The analysis of plastic deformations presented in the previous sections enables this model to obtain cutting energy associated with the machining process. The energy consumed in the primary shear and secondary deformation zones are superposed as the total cutting energy. Therefore, the prediction of shear angle is evaluated by comparing cutting energy from a set of trial shear angles. The true shear angle is found when cutting energy reaches the minimum. Figure 3.14 shows a generalized procedures of predicting shear angle ϕ , cutting energy E_c , cutting forces F_c and F_t , and cutting temperature rise in the primary shear deformation zone T_{AB} and in tool-chip interface zone T_{inter} . As seen in figure 3.14, the input data consists of undeformed chip thickness t_1 , width of cut w , cutting speed V_w , tool rake angle α_o , and room temperature T_{room} . Then, the outputs from this model are the predicted shear angle ϕ ,

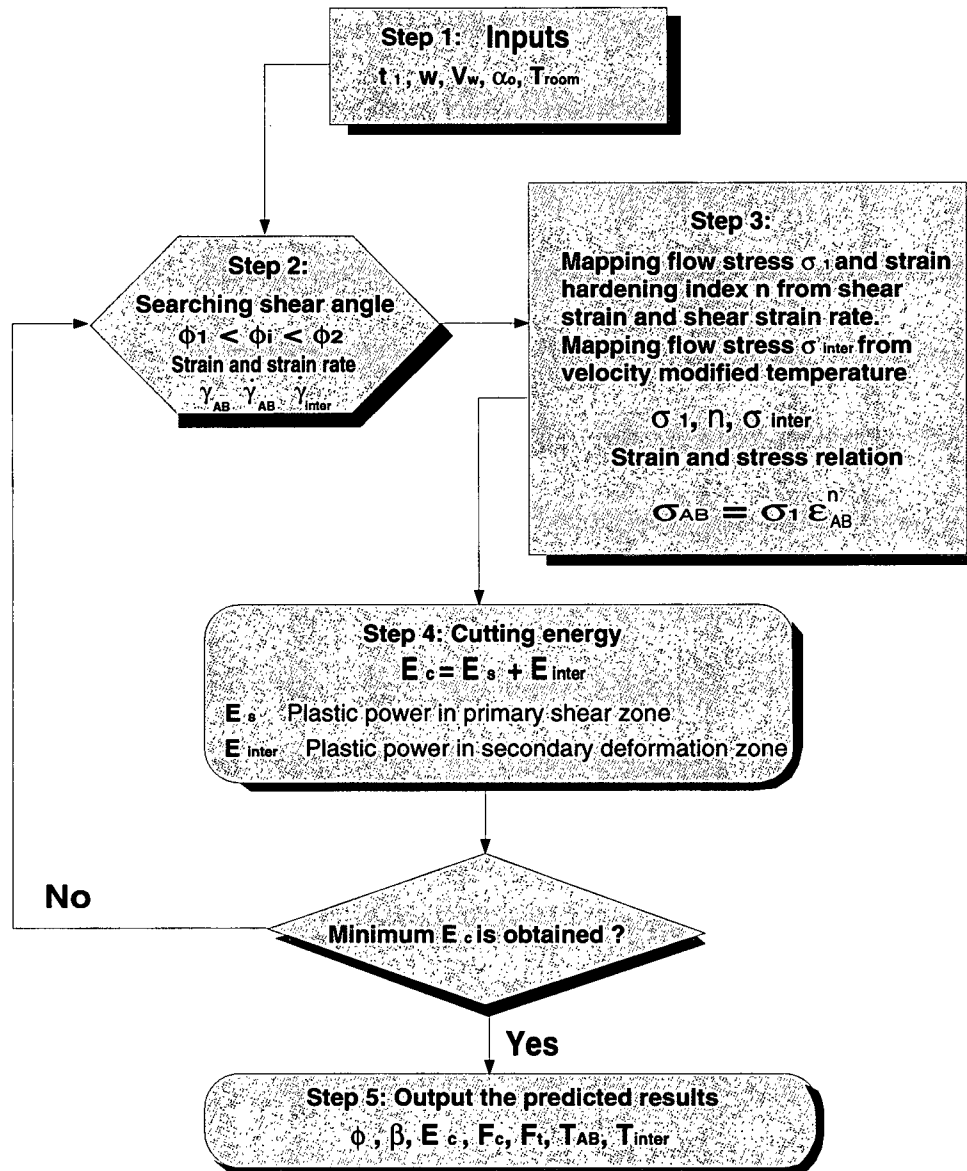


Figure 3.14: A generalized cutting process evaluation algorithm for cutting with sharp edge tools

friction angle β , cutting force F_c , feed force F_t , cutting energy per unit volume E_c , and cutting temperature rise in the primary shear zone T_{AB} and cutting temperature rise at the tool-chip interface T_{inter} . The procedures for the prediction will be explained as follows.

In step 2, a trial shear angle ϕ_i for each iteration is selected first between ϕ_1 and ϕ_2 . ϕ_1 and ϕ_2 are scanned from 5° and 45° , respectively. Shear strain γ_{AB} and shear strain rate $\dot{\gamma}_{AB}$ in the primary shear zone are calculated. Similarly, shear strain rate at tool-chip interface is also calculated.

$$\left. \begin{aligned} \gamma_{AB} &= \frac{\cos \alpha_o}{\sin \phi_i \cos(\phi_i - \alpha_o)} \\ \dot{\gamma}_{AB} &= \frac{S_c V_s}{l_{AB}} \\ \dot{\gamma}_{inter} &= \frac{V_c}{\delta t_2} \\ V_s &= \frac{V_w \cos \alpha_o}{\cos(\phi_i - \alpha_o)} \\ V_c &= \frac{V_w \sin \phi_i}{\cos(\phi_i - \alpha_o)} \\ l_{AB} &= \frac{t_1}{\sin \phi_i} \\ t_2 &= \frac{t_1 \cos(\phi_i - \alpha_o)}{\sin \phi_i} \end{aligned} \right\} \quad (3.59)$$

In step 3, flow stress σ_1 and strain hardening index n for the plastic deformation in primary shear zone are mapped from γ_{AB} and $\dot{\gamma}_{AB}$, which are evaluated using equations. 3.59 in step2. Then, flow stress σ_{AB} in the primary shear zone is evaluated by

$$\left. \begin{aligned}
 \sigma_{AB} &= \sigma_1 (\epsilon_{AB})^n \\
 \mathbf{k}_{AB} &= \frac{\sigma_{AB}}{\sqrt{3}} \\
 \epsilon_{AB} &= \frac{\gamma_{AB}}{\sqrt{3}} \\
 R_s &= \frac{F_s}{\cos(\phi_i + \beta_i - \alpha_o)} \\
 \beta_i &= \theta_i - \phi_i + \alpha_o \\
 F_s &= \mathbf{k}_{AB} l_{AB} w \\
 T_{AB} &= T_w + \eta \left[\frac{(1 - \lambda_s) F_s \cos \alpha_o}{\rho c t_1 w \cos(\phi_i - \alpha_o)} \right]
 \end{aligned} \right\} \quad (3.60)$$

$$\left. \begin{aligned}
 T_{inter} &= T_{AB} + \psi \Delta T_M \\
 F_{fc} &= R_s \sin \beta_i = \frac{\mathbf{k}_{AB} t_1 w \sin \beta_i}{\sin \phi_i \cos \theta_i} \\
 \Delta T_c &= \frac{F_{fc} \sin \phi}{\rho c t_1 w \cos(\phi - \alpha_o)} \\
 \log_{10} \left(\frac{\Delta T_M}{\Delta T_c} \right) &= 0.06 - 0.195 \delta \sqrt{\frac{R_T t_2}{l_c}} + 0.5 \log_{10} \left(\frac{R_T t_2}{l_c} \right) \\
 \dot{\epsilon}_{inter} &= \frac{\dot{\gamma}_{inter}}{\sqrt{3}} \\
 T_{modint} &= (T_{inter} + 273.0)(1 - 0.09 \log_{10} \dot{\epsilon}_{inter})
 \end{aligned} \right\} \quad (3.61)$$

where η , ψ , and λ_s are given in Appendix A. R_s is the resultant force acting on the slip-line \overline{AB} . θ_i and β_i are angle between resultant force and slip-line \overline{AB} and friction angle at the tool-chip interface corresponding to trial shear angle ϕ_i , respectively. Temperature rise for both in the primary shear zone T_{AB} and in secondary deformation zone T_{inter} are calculated as shown in figure 3.12. Once the velocity modified temperature T_{modint} is obtained, the flow stress σ_{inter} exerted at tool-chip interface is identified from equations shown in Appendix B.

In step 4, the total cutting energy is evaluated iteratively for each corresponding trial shear angle ϕ_i . Once the flow stresses σ_1 and σ_{inter} and strain hardening index n are identified for the corresponding trial shear angle ϕ_i , superposing energy dissipation in the primary shear deformation zone E_s from Eqn. 3.35 and energy dissipation in the tool-chip interface zone E_{inter} from Eqn. 3.39 yields the total cutting energy per unit volume (E_c)

$$E_c = \frac{\sigma_1}{n+1} \left[\frac{\cos \alpha_o}{\sqrt{3} \sin \phi_i \cos(\phi_i - \alpha_o)} \right]^{n+1} + \frac{3\sigma_{inter} l_c \sin \phi_i}{4\sqrt{3} t_1 \cos(\phi_i - \alpha_o)} \quad (3.62)$$

where the contact length l_c is estimated from equation 3.45. The total cutting energy per unit volume E_c is compared iteratively for the different trial shear angles ϕ_i . Iteration continues until the E_c reaches the minimum.

In step 5, the shear angle ϕ_s is predicted once the corresponding total cutting energy E_c is found to be the minimum. Again, shear stress on the slip-line \overline{AB} in the primary shear deformation zone (\mathbf{k}_{AB}), friction angle β , cutting temperatures T_{AB} and T_{inter} are predicted as well when the identified shear angle ϕ_s is used in step 3. Therefore, cutting forces are predicted. Noted that the total predicted cutting forces F_c and F_t are obtained by summing up the forces contributed from the primary shear zone (F'_c, F'_t) and the edge forces generated by the flank-finish surface contact (F_{ce}, F_{te}) from equations C.11 in Appendix C. This approach is validated by Budak, Altintas, and Armarego [1].

$$\left. \begin{aligned}
 \beta &= \theta - \phi_s + \alpha_o \\
 F_c' &= \frac{F_s \cos(\beta - \alpha_o)}{\cos(\phi_s + \beta - \alpha_o)} \\
 F_t' &= \frac{F_s \sin(\beta - \alpha_o)}{\cos(\phi_s + \beta - \alpha_o)} \\
 F_c &= F_c' + F_{ce} \\
 F_t &= F_t' + F_{te}
 \end{aligned} \right\} \quad (3.63)$$

3.4.2 Model Verification

The model developed in this chapter aims to predict shear angle, mean friction angle on the tool rake face, cutting forces, temperature, strain rate in the primary shear and secondary deformation zones. This model mainly deals with machining with conventional sharp tools. Since machining removal rate is directly proportional to the undeformed chip thickness t_1 and cutting speed V_w , it is of interest to evaluate cutting performance associated with various t_1 and V_w . The effect of undeformed chip thickness t_1 and cutting speed V_w is analyzed by the proposed model in this chapter. The ranges of undeformed chip thickness $t_1 : 0.02 \sim 0.11 \text{ mm}$ and cutting speed $V_w : 90 \sim 700 \text{ m/min}$ are used in all model simulations. The experimental test ranges for t_1 are 0.02, 0.04, 0.06, 0.08, 0.10 mm. The experimental test ranges for cutting speed V_w are 100, 240, 380, 600 m/min, respectively. Cutting tools used in experiments are all SANDVIK S10 carbide tools with zero rake angle and 10° clearance angle.

Shear Angle ϕ

For the prediction of shear angle in machining process, first attempt was made to compare

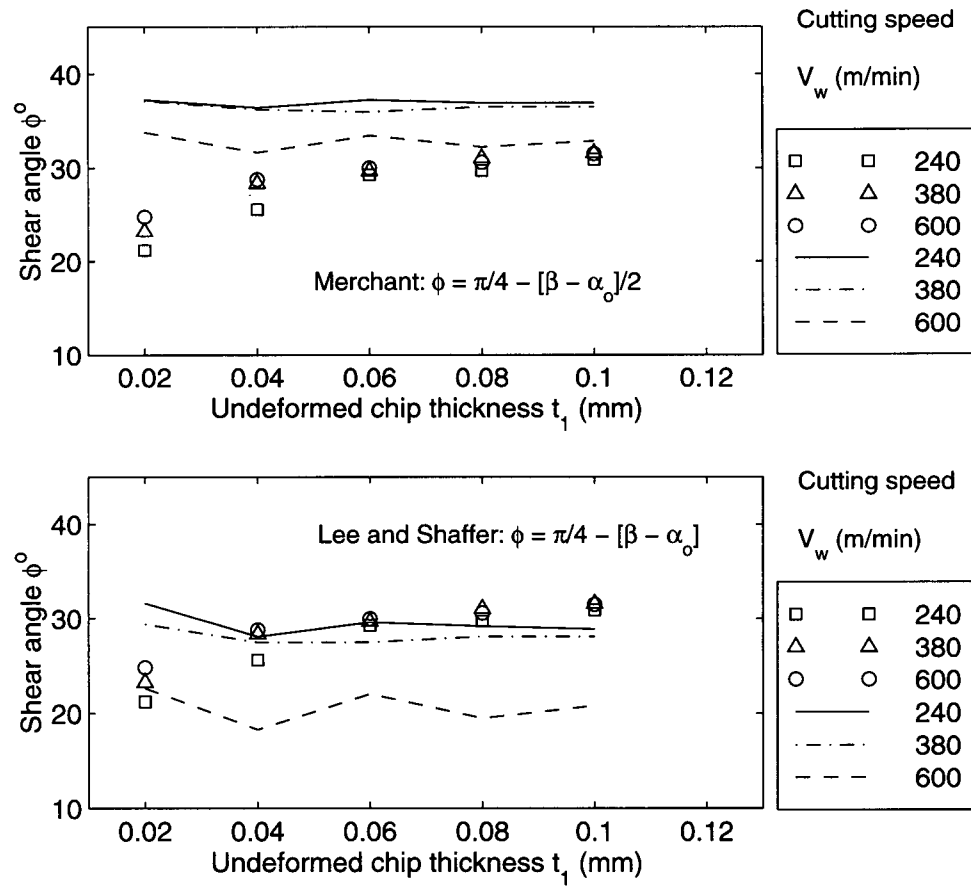


Figure 3.15: Predicted shear angles by Merchant's [21] and Lee and Shaffer's [22] shear angle solutions

the shear angles predicted by Merchant's [21] and Lee and Shaffer's [22] solutions with those evaluated from experiments. Figure 3.15 shows the prediction of shear angles applying the equations 2.9 and 2.11 proposed by Merchant and Lee and Shaffer. As Kobayashi et al. [24] pointed out, the agreement between the experimental shear angle and predicted results by their solution is poor. The predicted shear angles by Merchant's solution are close to experimental ones only when cutting speed V_w is very high with large undeformed chip thickness t_1 . The predicted shear angles by Lee and Shaffer's solution are close to experimentally evaluated shear angles as cutting speed is low. In figure 3.15, predicted shear angles by lines stand for the shear angle solutions obtained by Merchant [21] and Lee and Shaffer [22], respectively. Symbols represent the experimentally measured shear angles.

Figure 3.16 shows the predicted shear angles by proposed model and shear angles obtained experimentally versus various undeformed chip thickness t_1 under three different cutting speeds, V_w , 240, 380, 600 m/min. The predicted results show good agreement with experimental results except when $t_1 < 0.04\text{mm}$. The predicted shear angles versus various cutting speeds are shown in figure 3.17. It can be seen that the predicted shear angles from the proposed model are better than that predicted by Merchant's and Lee and Shaffer's solutions as shown in figure 3.15 compared with experimentally measured shear angles. Both experimental and predicted shear angles show that shear angle changes insignificantly as undeformed chip thickness t_1 is larger than 0.05 mm and cutting speed V_w is higher than 240 m/min.

Friction Effects

As seen in figure 2.5, friction state affects the orientation of resultant force R_s exerted on the tool rake face. Friction state is observed to be varied with different cutting conditions. Figure 3.18 shows the variation of experimentally evaluated friction angles (equation 3.44) and measured contact length with various cutting speeds.

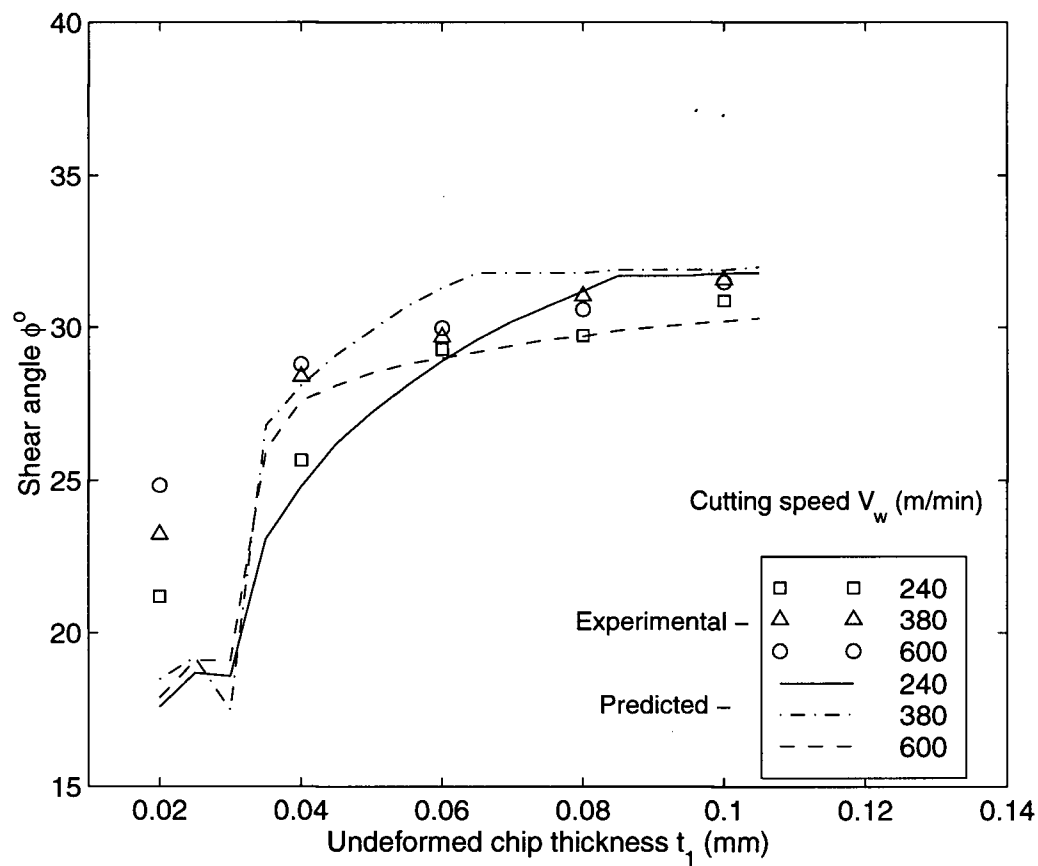


Figure 3.16: Comparison of predicted shear angles by the proposed model with experimentally evaluated shear angles, $w=3.6$ mm, $\alpha_o = 0^\circ$, V_w : 240, 380, 600 m/min.

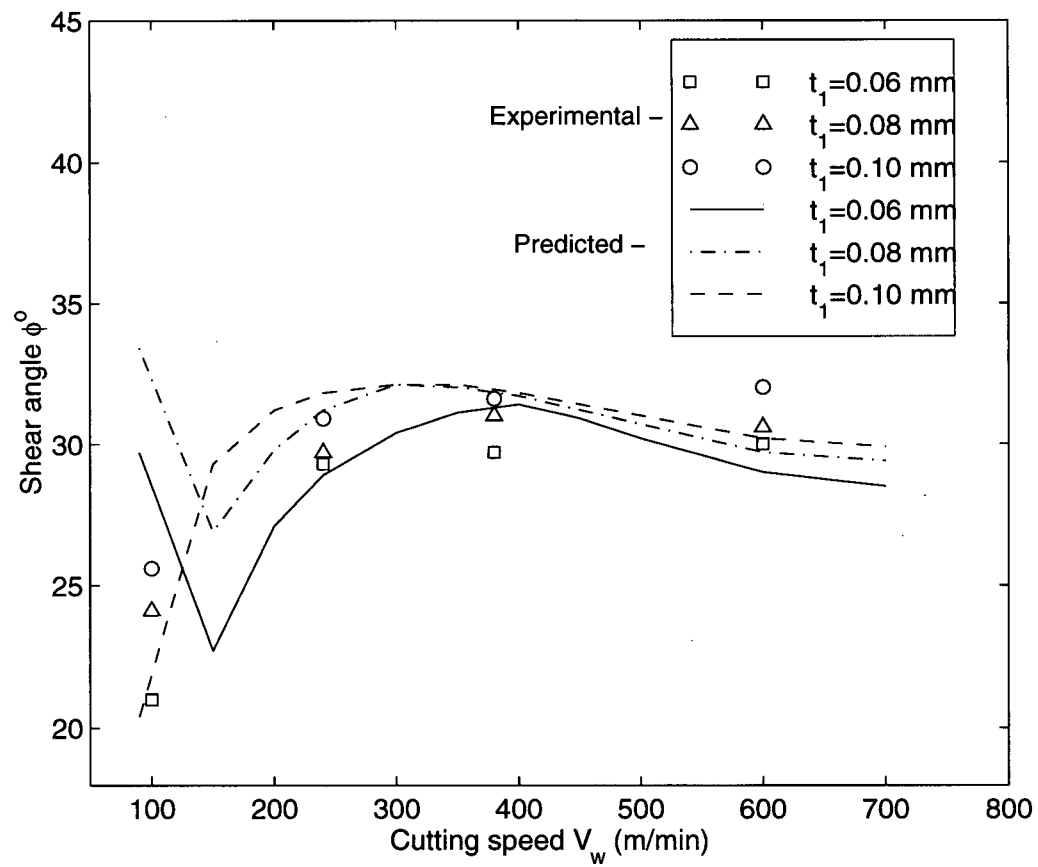


Figure 3.17: Comparison of predicted shear angles by the proposed model with experimentally evaluated shear angles, $w=3.6$ mm, $\alpha_o = 0^\circ$, t_1 : 0.06, 0.08, 0.10 mm.

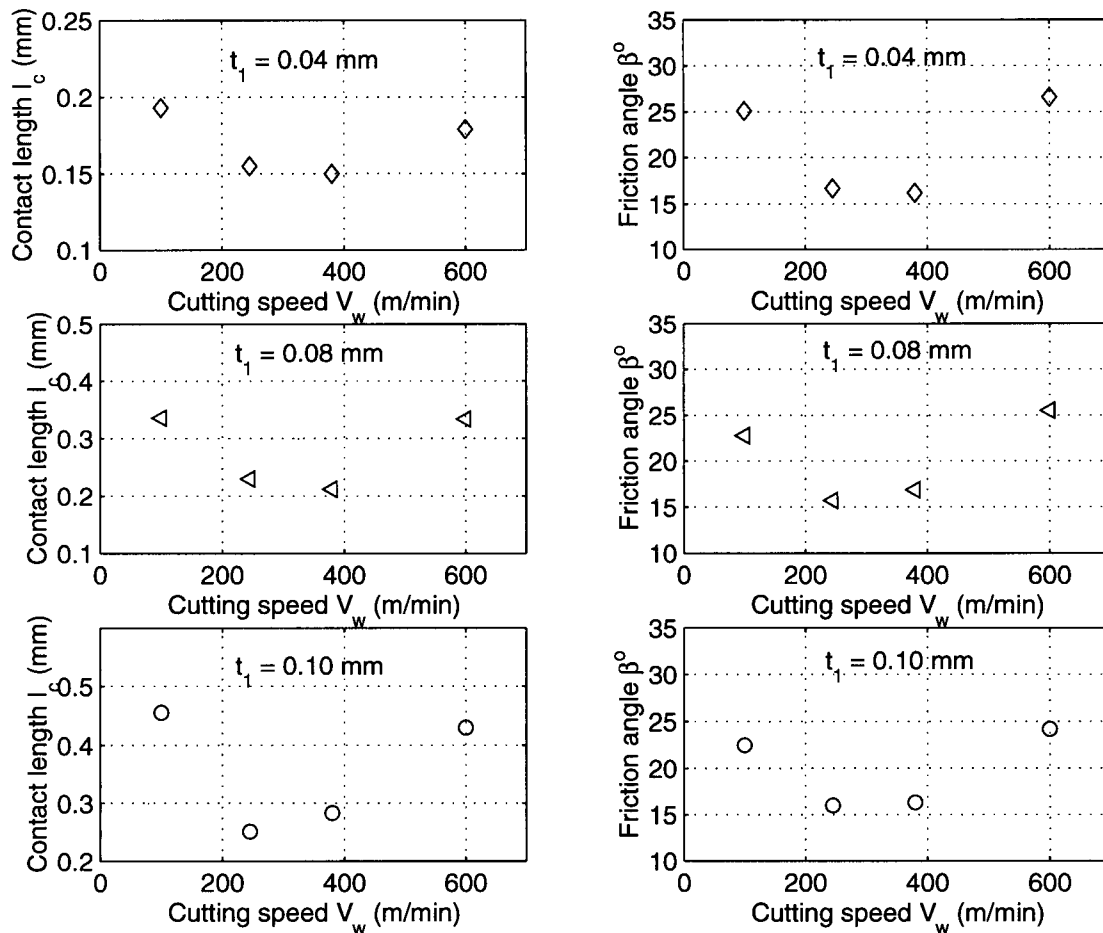


Figure 3.18: Variation of experimentally measured contact length l_c and friction angle β with cutting speed V_w .

It can be seen that the variation of contact length l_c and friction angle β with cutting speed V_w shows a similar pattern. Both contact length l_c and friction angle β are relatively high when cutting speed is relatively low. l_c and β decrease with increasing of cutting speed. Again, further increase of cutting speed causes l_c and β to increase. This event indicates that contact length l_c is one of the most important factors which control friction states at the tool-chip interface. To explain this pattern, it is of interest to analyze the effects of shear flow stress k_{inter} along the tool-chip interface on the friction state. Since the resultant force (R_s) acting on the slip-line \overline{AB} in the primary shear zone is in equilibrium with the resultant force (R_s') on the tool rake face.

$$\left. \begin{aligned} R_s &= R_s' \\ \frac{k_{AB} t_1 w}{\sin\phi \cos\theta} &= \frac{3 k_{\text{inter}} l_c w}{4 \sin\beta} \\ \sin\beta &= \frac{3 k_{\text{inter}} l_c \sin\phi \cos\theta}{4 k_{AB} t_1} \end{aligned} \right\} \quad (3.64)$$

As shown in equation 3.64, the mean friction angle at the tool-chip interface β is proportional to the contact length l_c along the tool-chip interface. When the cutting speed increases up to certain value, the flow stress k_{inter} tends to decrease due to the effect of high temperature T_{inter} . Oxley et al. [6] also supported that the decrease of k_{inter} is caused by the increase in T_{inter} . The reason for the increase of friction angle at relatively high cutting speed may be attributed to the chipping of tool edge and fast tool wear.

Figure 3.19 shows the variation of predicted and experimentally calculated friction angles against cutting speeds. The variation of friction angles with cutting speed follows similar pattern aforementioned. But the deviation between the predicted values and experimental values is large. Possible reasons are the inaccurate prediction of resultant force angle θ and shear angle

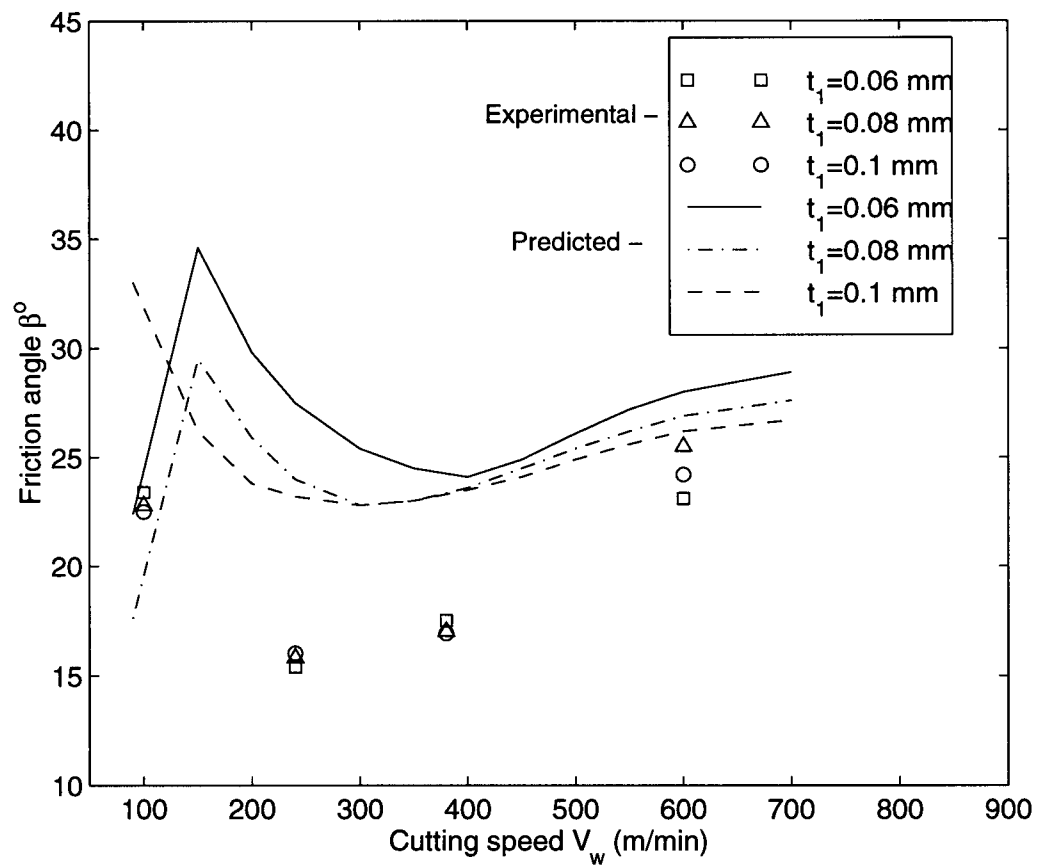


Figure 3.19: Predicted and experimentally determined friction angles versus various cutting speeds, $w=3.6$ mm, $\alpha_o = 0^\circ$, t_1 : 0.06, 0.08, 0.10 mm.

ϕ , which are used to predict friction angle from equation 3.63.

Figure 3.20 shows the predicted and experimental friction angles against various undeformed chip thickness. The predicted results show good agreement with those obtained experimentally at cutting speed $V_w = 600$ m/min. From experimental values, it seems that friction angle show little variation with undeformed chip thickness. Again, the deviation between experimentally evaluated friction angles and predicted is possibly due to the inaccurate measurement of contact length along the tool rake face.

Cutting Energy E_c

In machining process, the efficiency of the machining under certain cutting conditions can be evaluated by using the cutting energy per unit volume E_c (J/mm³). The predicted cutting energy from the proposed model is determined from equation 3.62. The cutting energy per unit volume E_c is evaluated from experiments by

$$E_c = \frac{(F_c - F_{ce}) V_w}{V_w t_1 w} = \frac{F_c - F_{ce}}{t_1 w} \quad (3.65)$$

The variation of predicted and experimentally determined cutting energy per unit volume of cut with cutting speed is shown in figure 3.21. The predicted cutting energy E_c shows good agreement with experimental cutting energy. It seems that the cutting energy E_c shows the same trend as the variation of contact length l_c and friction angle β with cutting speed. Cutting energy per unit volume tends to be higher when cutting speed is relatively low and high. The results from tool wear tests suggest that the tool wear in terms of flank wear V_B is relatively low at the cutting speed of 240 m/min among a range of cutting speeds $V_w : 60, 120, 240, 380, 600$ m/min ($t_1 = 0.06$ mm).

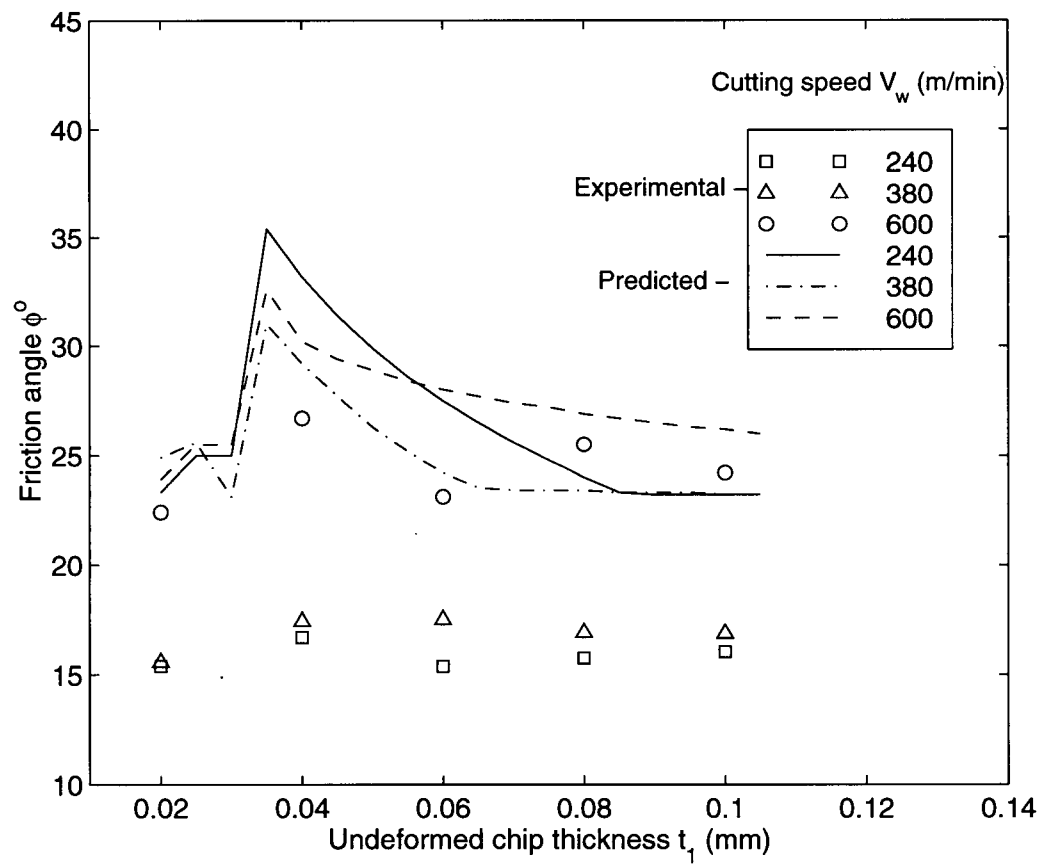


Figure 3.20: Predicted and experimentally determined friction angles versus various undeformed chip thickness, $w=3.6$ mm, $\alpha_o = 0^\circ$, V_w : 240, 380, 600 m/min.

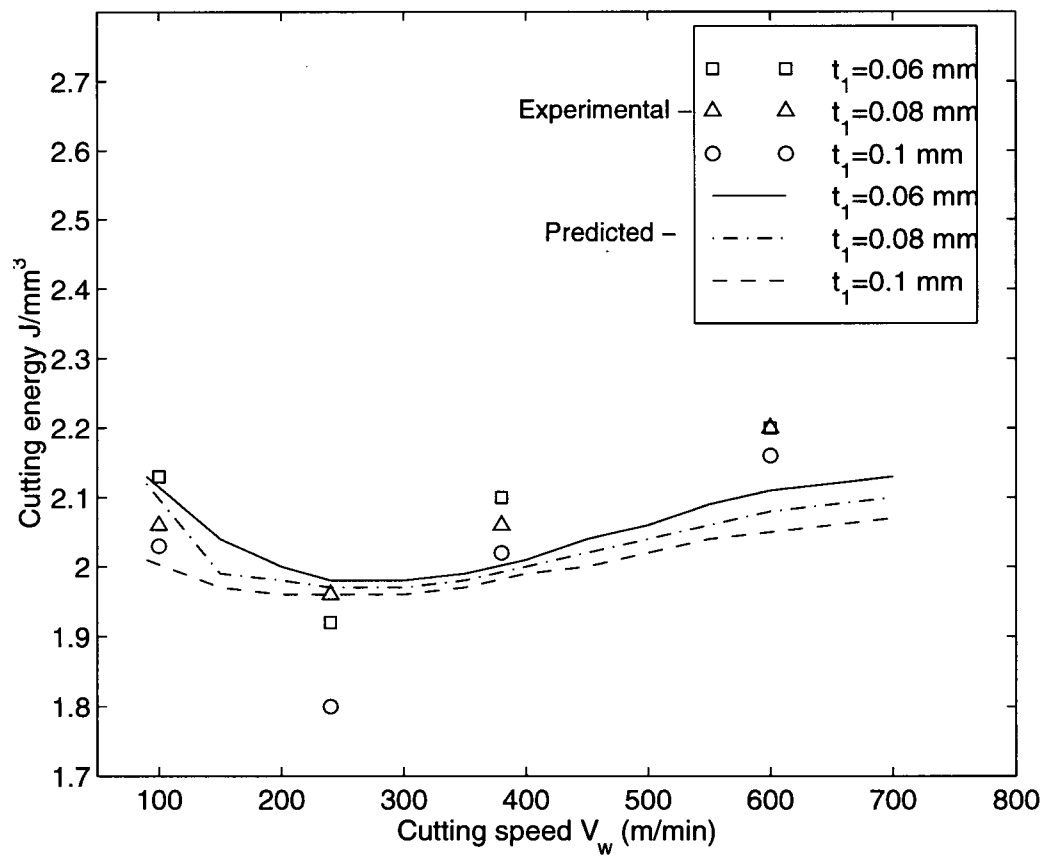


Figure 3.21: Predicted and experimentally determined cutting energy per unit volume of cut, $w=3.6$ mm, $\alpha_o = 0^\circ$, t_1 : 0.06, 0.08, 0.10 mm.

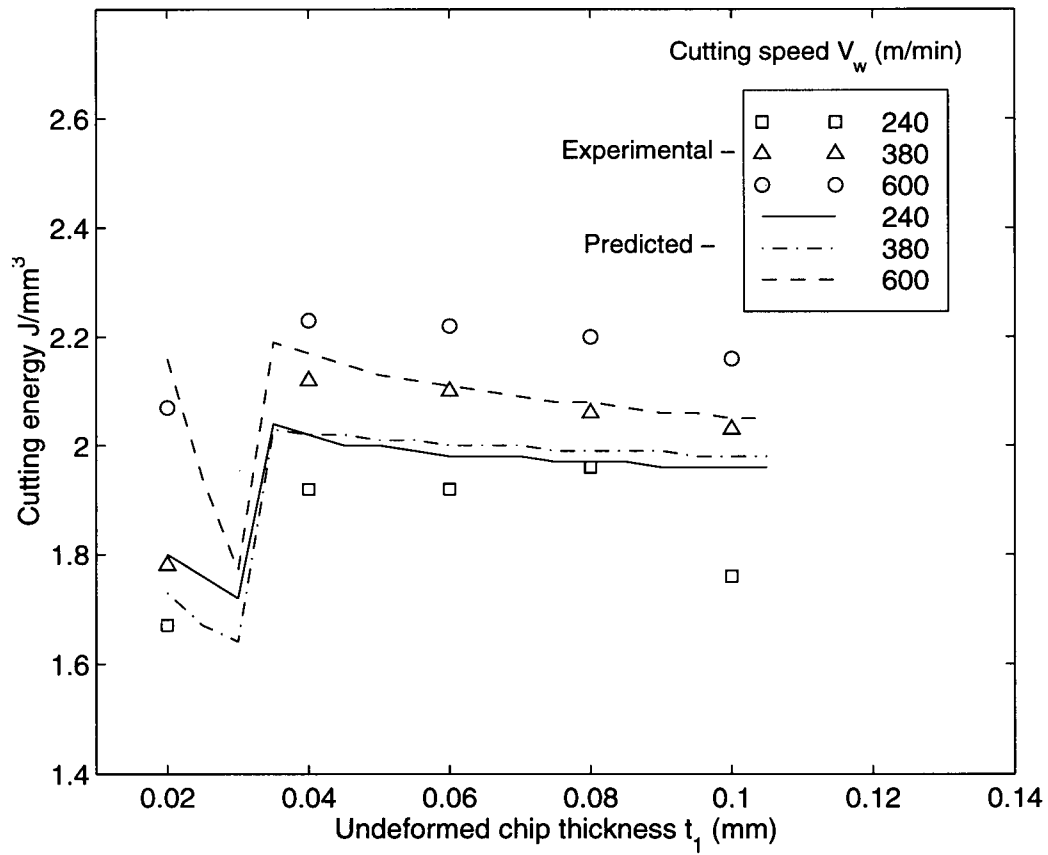


Figure 3.22: Predicted and experimentally determined cutting energy per unit volume of cut, $w=3.6$ mm, $\alpha_o = 0^\circ$, V_w : 240, 380, 600 m/min.

Figure 3.22 shows the variation of predicted and experimentally determined cutting energy per unit volume of cut with undeformed chip thickness t_1 . The predicted results are close to the experimental results.

Cutting Temperatures T_{AB} and T_{inter}

The energy consumed in cutting process is largely converted into heat in the primary shear deformation and the tool-chip interface zones. In fact, tool wear is mainly attributed to the high compressive stress and high temperature exerted on the cutting tool. Trent [45] suggested that tool wear of carbide tools show less sensitivity to the cutting temperature rise at the tool-chip interface up to $1200^\circ C$. Cutting temperature rise in the primary shear zone T_{AB} is predicted from equation 3.60. Temperature at the tool-chip interface T_{inter} from equation 3.61.

The predicted cutting temperatures T_{AB} and T_{inter} against cutting speed is shown in figure 3.23. The cutting temperature T_{AB} in the primary shear zone shows the less dependency on the changes of cutting speeds. For a range of cutting speeds ($100 \sim 600 m/min$), the variation of T_{AB} is about $300^\circ C \sim 400^\circ C$. Oxley and Stevenson [62] explained that T_{AB} rises rapidly at low cutting speed V_w due to rapidly changing the ratio λ_s (see in Appendix A). The temperature rise tends to be adiabatic with little heat conducted into the work material when cutting speed is higher. Therefore, T_{AB} remains approximately constant. The strain rate increases approximately linearly with cutting speed and strain hardening decreases with the increase of cutting speed as seen in figure 3.13. Cutting temperature T_{AB} reaches adiabatic state as result of high cutting speed. For the temperature rise at tool-chip interface T_{inter} , it can be seen that T_{inter} is almost proportional to the cutting speed. It is apparent that the friction is much more severe along the tool-chip interface when cutting speed gets higher.

Figure 3.24 show the variation of predicted cutting temperatures T_{AB} and T_{inter} with undeformed chip thickness t_1 . Since heat generated in the primary shear deformation zone

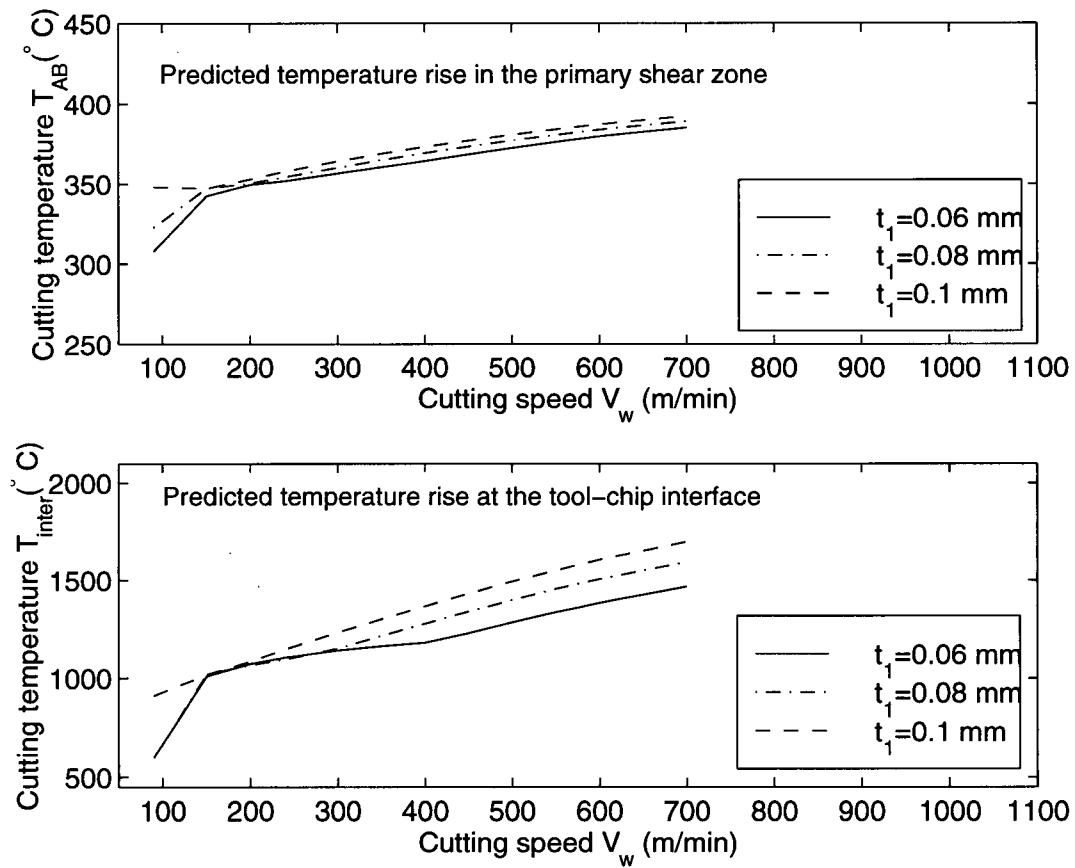


Figure 3.23: Predicted cutting temperatures rise in the primary shear zone and the tool-chip interface zone versus cutting speed, $w=3.6$ mm, $\alpha_o = 0^\circ$, t_1 : 0.06, 0.08, 0.10 mm.

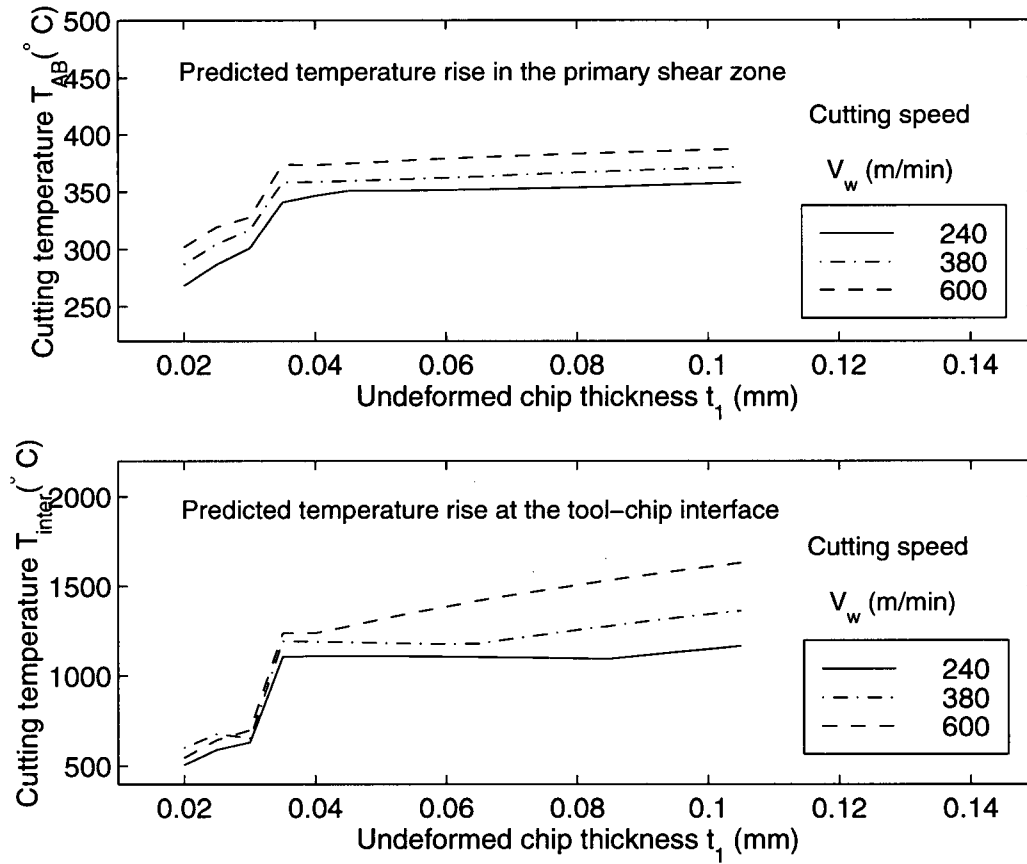


Figure 3.24: Predicted cutting temperatures rise in the primary shear zone and the tool-chip interface zone versus undeformed chip thickness t_1 , $w=3.6$ mm, $\alpha_o = 0^\circ$, V_w : 240, 380, 600 m/min.

is proportional to the strain energy E_s , predicted temperature rise in the primary shear zone shows less variation with the undeformed chip thickness. The temperature rise at the tool-chip interface T_{inter} increases slowly with the increase of t_1 at low cutting speeds. However, T_{inter} changes rapidly with the increase of undeformed chip thickness t_1 at high cutting speed.

The comparison between tool wear rate observed from experiments and corresponding predicted cutting temperature in the primary shear and secondary deformation zones under a range of cutting speed is shown in figure 3.25. It can be seen that cutting tool gets worn rapidly once cutting speed is higher than 240 m/min. Predicted cutting temperature at the tool-chip interface indicates that temperature reaches diffusion point of Cobalt binding material used S10 carbide tools when cutting speed increases beyond 240 m/min. It is found that cutting speed $V_w=240$ m/min, corresponds to the minimum wear rate. SEM analysis indicated that adhesion is dominant under the cutting speed lower than $V_w=240$ m/min and diffusion is active above the cutting speed $V_w=240$ m/min.

Cutting Force F_c and F_t

The surface finish, cutting temperatures, and tool life are directly influenced by the cutting forces. The variation of predicted cutting forces (F_c , F_t) with cutting speed and undeformed chip thickness are compared with those measured from experiments.

The predicted cutting force F_c and feed force F_t are found from equation 3.61. Figure 3.26 shows the predicted and experimentally measured cutting forces versus various cutting speed. The equation 3.61 indicates that the decrease of cutting forces F_c and F_t are due to the increase of shear angle as the cutting speed is changed from 90 to 240 m/min. Further increase of cutting speed V_w does not lead to significant reduction of cutting forces. Predicted results show close agreement with experimentally measured forces.

Figure 3.27 shows the variation of predicted and experimentally measured cutting forces

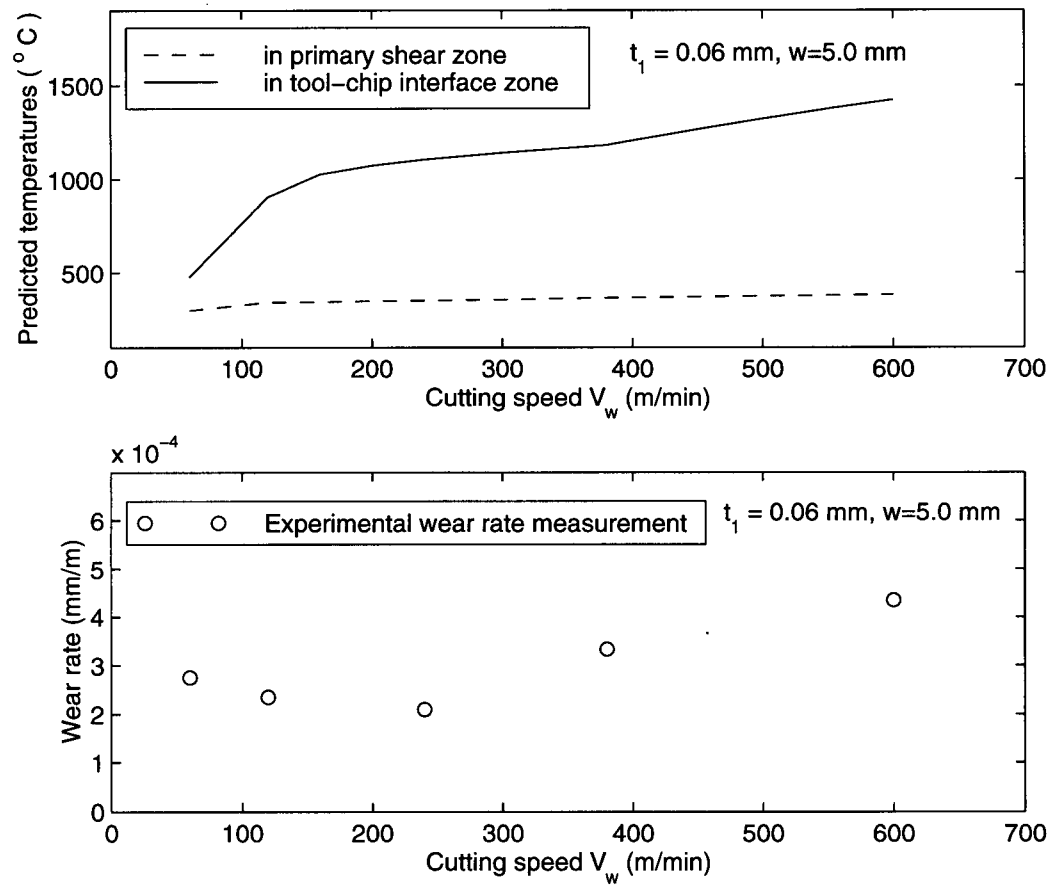


Figure 3.25: Plot of predicted cutting temperatures T_{AB} and T_{inter} and experimentally measured wear rate versus cutting speed, $w = 5.0$ mm, $\alpha_o = 0^{\circ}$, $t_1 = 0.06$ mm.

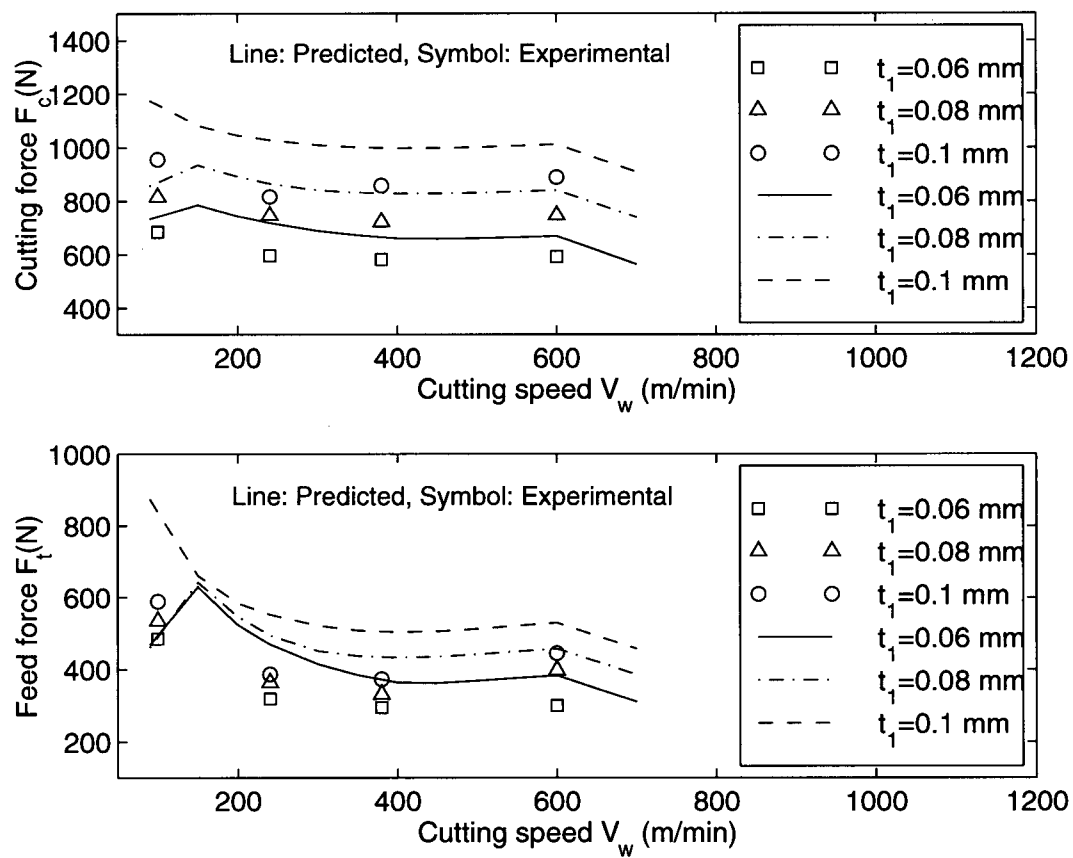


Figure 3.26: Predicted and experimental measured cutting forces versus cutting speed, $w=3.6$ mm, $\alpha_o = 0^\circ$, t_1 : 0.06, 0.08, 0.10 mm.

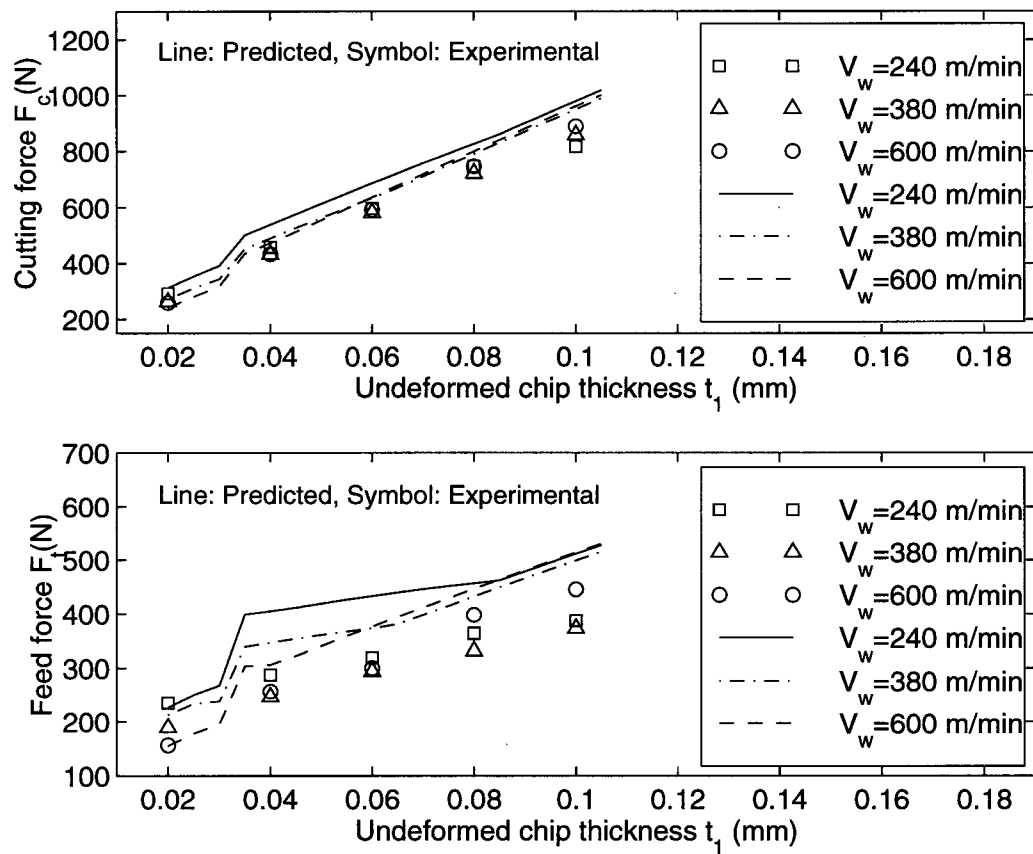


Figure 3.27: Predicted and experimentally measured cutting forces versus undeformed chip thickness t_1 , $w=3.6$ mm, $\alpha_o = 0^\circ$, V_w : 240, 380, 600 m/min.

against undeformed chip thickness t_1 . The cutting force component F_c is close to experimental cutting force component. There exists some deviation especially for the feed force component F_t . Possible errors may come from inaccurate analytical prediction of friction angle β from equations 3.61.

Shear stress in the primary shear zone

Figure 3.28 shows the predicted and experimentally calculated shear stresses versus cutting speed. The experimental shear stress is evaluated from the measured cutting forces and experimental shear angle using the equation 3.46. The predicted shear stress is found from the equation 3.60 when shear angle is predicted from given cutting conditions. The predicted shear stress shows close agreement with that evaluated from experiments except at cutting speed $V_w < 150 \text{ m/min}$. The comparison between the predicted shear stress and experimental shear stress against undeformed chip thickness is shown in figure 3.28. The predicted shear stress also shows close agreement with experimentally evaluated shear stress. One can note that the accurate prediction of shear stress is needed in order to predict cutting forces accurately.

3.5 Summary

A model for high speed orthogonal machining with conventional sharp tools is presented in this chapter. The proposed model involves establishing P20 material constitutive relation under high strain rate and high temperature through orthogonal machining test and analyzing plastic deformation in the primary shear and the tool-chip interface zones. Strain, strain rate, stress, and temperature are evaluated using the model proposed by Oxley et al. [6], [36]. The energy dissipation in the primary shear and the tool-chip interface zones are formulated. The Minimum Energy Principle is applied to predict shear angle in machining process. By

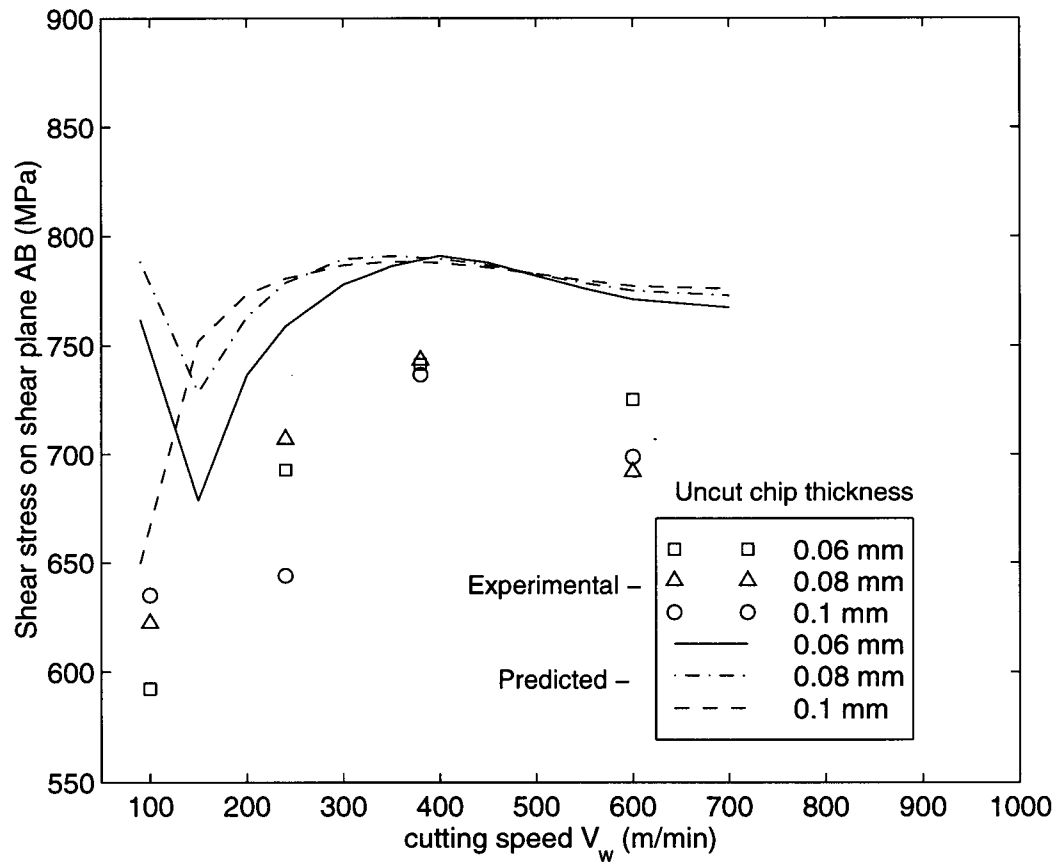


Figure 3.28: Predicted and experimentally evaluated shear stress in the primary shear zone versus cutting speed, $w=3.6$ mm, $\alpha_o = 0^\circ$, t_1 : 0.06, 0.08, 0.10 mm.

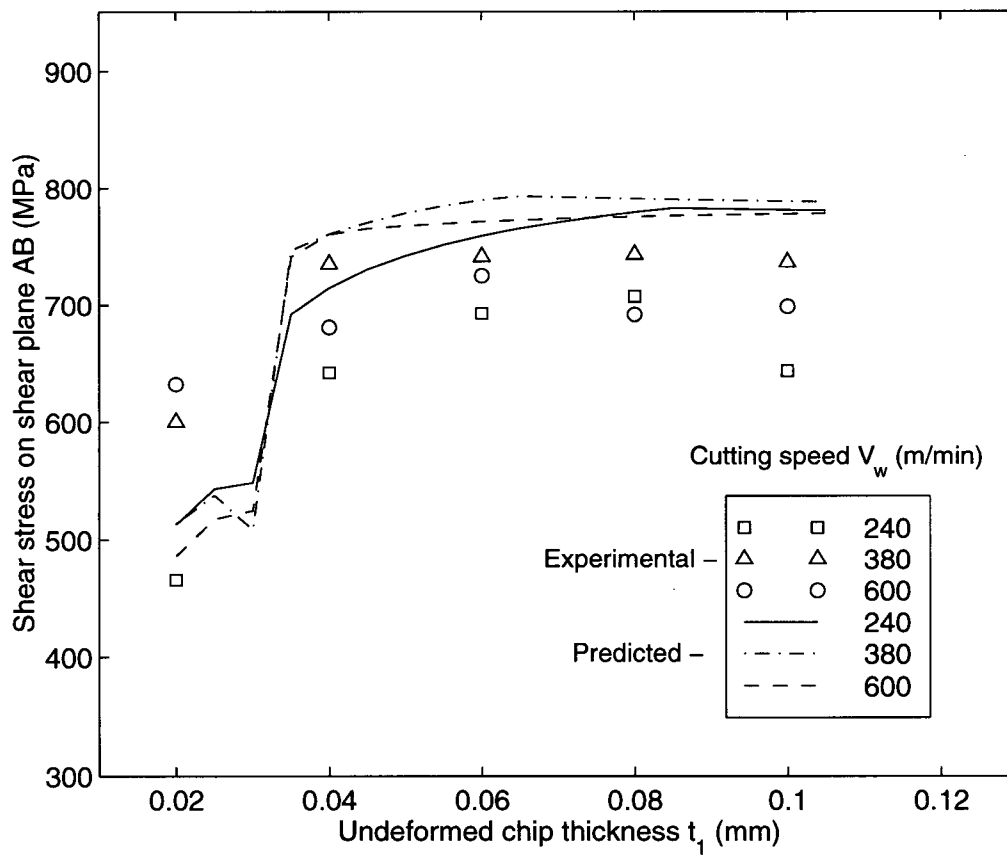


Figure 3.29: Predicted and experimentally evaluated shear stress in the primary shear zone versus undeformed chip thickness t_1 , $w=3.6$ mm, $\alpha_o = 0^\circ$, V_w : 240, 380, 600 m/min.

inputting the undeformed chip thickness, cutting speed, width of cut, main rake angle, and room temperature, this model enables process planer to estimate forces and temperature for cutting P20 mold steel under a different cutting conditions.

Chapter 4

Modeling of Machining with Chamfered Tools

4.1 Introduction

In practice, machining process is optimized based on some variables, such as the tool wear rate, cutting temperature, cutting forces or power, chatter, surface finish, and dimensional errors left on the workpiece. The quest for low costs and high productivity has led to the high speed machining and intelligent machining process control. High speed machining means high material removal rate. In the high speed machining of dies and molds, tool wear is one of the major concerns. The performance of a cutting tool, or the machinability, is measured in terms of tool life, surface finish, and metal removal rate as a function of tool geometry, feed and cutting speed, and work material properties. The machinability study is usually carried out by conducting series of cutting tests and tool life measurements in industry. Tool geometry plays an important part in the cutting performance. In general, negative rake geometry enables the brittle cutting tool to sustain heavy cutting and strengthens the edge of cutting tool. However, negative rake geometry leads to larger cutting forces than positive rake, and consequently results in higher temperatures. High positive rake angle has the advantage of reducing cutting forces at the expense of weakening cutting edge of the tool. Since the tool starts wearing from the cutting edge, optimizing the edge geometry is also an avenue to improve cutting performance. Unfortunately, conventional tool geometry design is often carried out by trial and error methods. The aim of fundamental research in cutting mechanics is to minimize the number of costly machining tests, and narrow the optimal tool geometry design and cutting conditions by

predicting them analytically. Such an attempt is made in high speed machining of hardened P20 mold steels with chamfered carbide and CBN tools in this chapter.

There are three basic ways in which the cutting edge is usually prepared: honed radius on the actual corner, a chamfer which breaks the corner, and land, stretching back negatively from the clearance side to various lengths on to the insert face [63]. In modern machining practice, cutting inserts with designed chamfered cutting edge are commonly introduced by cutting tool industry to enhance the cutting tool performance under certain circumstances. The investigations of cutting with chamfered edge tools have been carried out by some researchers [39], [46], [47], [3], [50]. However, a comprehensive understanding about the insight into the machining with chamfered tools is still not available.

In this chapter, a comprehensive analytic model of the process is developed. The plastic deformation is separated into the primary shear, dead metal zone created by the chamfer, and the secondary deformation zone where the chip moves over the regular rake face of the tool. Oxley's [6] slip-line field with strain, strain rate and temperature dependent flow stress model is extended to model primary and secondary deformation zones. The flow stress of the material is calibrated as a function of strain, strain rate and temperature from orthogonal machining tests with sharp tools, as opposed to high-speed compression tests. The dead metal zone is modeled as an extrusion process, where the dead metal boundary is assumed to act like the wall of a die. The total contact length between the chip and the regular face of the cutting tool rake was expressed as an empirical function of uncut chip thickness, and calibrated from experimental observations. The sticking and sliding chip contact lengths are considered to be equal in modeling the total friction force on the rake. The shear angle is estimated by minimizing the energy consumed in the three deformation zones. The proposed model predicts the shear angle, cutting forces, and cutting temperature from given cutting conditions. The proposed model is verified with high speed orthogonal cutting tests using both ISO S10 carbide and CBN tools applied on P20 mold steel work material. It is shown that the proposed model is able to identify the most

optimal chamfer angle and cutting speed, which yields lowest tool wear and relatively lower cutting forces.

4.2 Modeling of Plastic Deformation for Cutting with Chamfered Tools

In high speed machining with chamfered tools, plastic deformation under the chamfered edge must be taken into account since a chamfered tool has different mechanics than a sharp edge tool concerning the chip formation as presented in chapter 3. To analyze the chip formation for such tools, a cutting mechanics model is proposed as shown in figure 4.1. The proposed model assumes that a surface layer of work material defined by the undeformed chip thickness t_1 flows into the primary shear deformation zone, and separates at a stagnant point B, see figure 4.1. The velocities of workpiece, shear and chip are indicated as V_w , V_s , and V_c , respectively. From point B, some of the material is trapped in the dead zone created by the chamfer, where the material flows over towards the regular rake face and forms the chip. Chamfer geometry is defined by the length of chamfer edge (b_{cf}) and chamfer angle (second rake angle α_1). The proposed slip line field is used to form energy equations for primary shear zone (AB), chamfered zone (OH) and secondary deformation zone where the chip flows over the regular rake face (HG). The energy equations are used to predict the shear angle, force and temperature while considering the flow stress, strain, strain rate and temperature effects. Again, plane strain, steady-state continuous chip formation are assumed in this model.

Following the similar approach presented in chapter 3, the analysis of strain, strain rate, temperature, and energy dissipation in the primary shear, dead metal and secondary deformation zones is carried out as follows.

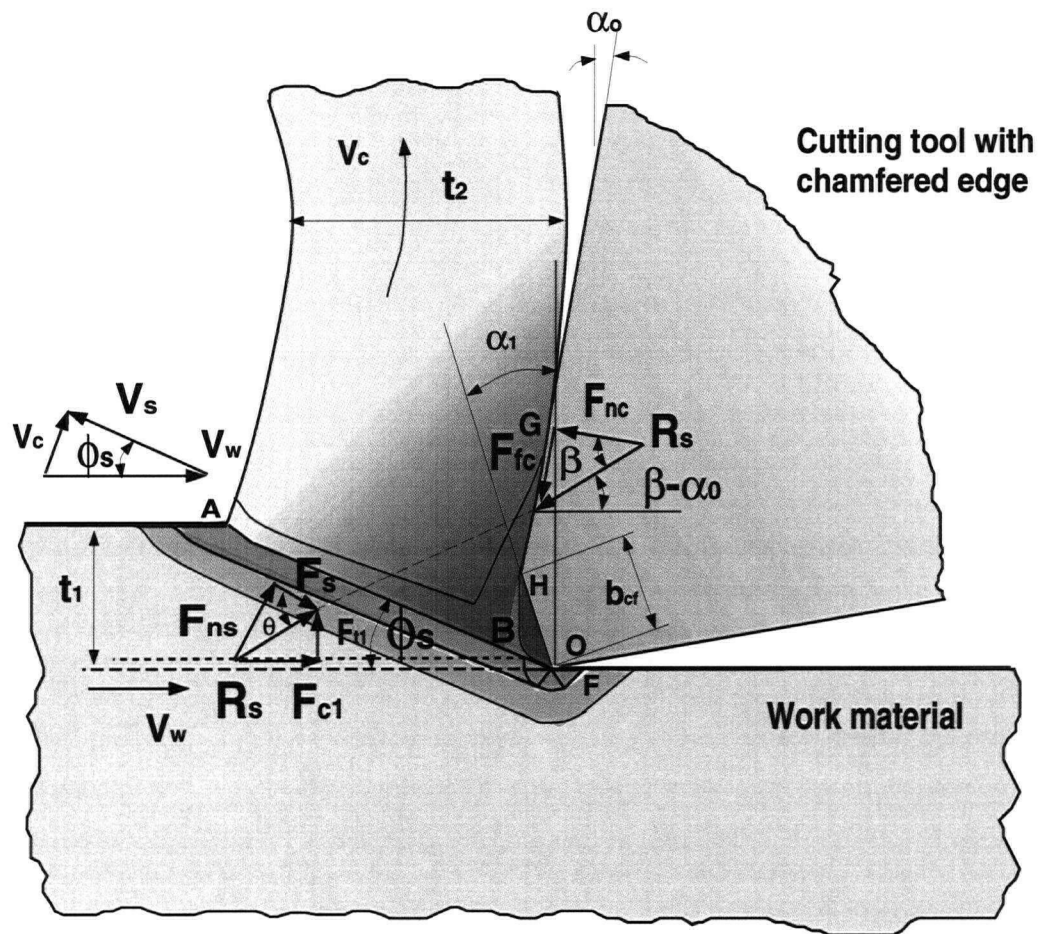


Figure 4.1: A proposed chip formation model for cutting with chamfered tools

4.2.1 Plastic Deformation in the Primary Shear Zone

The same method to determine strain and strain rate presented in chapter 3 is applied here. Slip-line \overline{AB} in the primary shear zone is assumed to be the line of maximum shear strain and shear strain rate as proposed by Oxley et al. [6], [36], see figure 4.1.

Shear strain γ_{AB} and shear strain rate $\dot{\gamma}_{AB}$ in the primary shear deformation zone are given by the following equations

$$\left. \begin{aligned} \gamma_{AB} &= \frac{\cos \alpha_o}{\sin \phi_i \cos(\phi_i - \alpha_o)} \\ \dot{\gamma}_{AB} &= \frac{\gamma_{AB}}{\Delta t} = \gamma_{AB} \frac{V_s}{l_{AB}} = S_c \frac{V_s}{l_{AB}} \\ V_s &= \frac{V_w \cos \alpha_o}{\cos(\phi_i - \alpha_o)}, \quad l_{AB} = \frac{t_1}{\sin \phi_i} \end{aligned} \right\} \quad (4.1)$$

where α_o , ϕ_i , l_{AB} , V_s are main rake angle of cutting tool, shear angle, length of shear line \overline{AB} , and shear velocity along \overline{AB} . S_c is taken to be about 6.0 as explained in chapter 3.

From Von-Mises yield criterion, shear flow stress (\mathbf{k}_{AB}) distributed along AB in the primary shear zone is found by

$$\left. \begin{aligned} \sigma_{AB} &= \sigma_1 \epsilon_{AB}^n \\ \epsilon_{AB} &= \frac{\gamma_{AB}}{\sqrt{3}} \\ \mathbf{k}_{AB} &= \frac{\sigma_{AB}}{\sqrt{3}} = \frac{\sigma_1 \epsilon_{AB}^n}{\sqrt{3}} \\ F_s &= \mathbf{k}_{AB} l_{AB} w = \frac{\sigma_1 \epsilon_{AB}^n}{\sqrt{3}} l_{AB} w \end{aligned} \right\} \quad (4.2)$$

where σ_{AB} , n , and F_s are flow stress, strain hardening index, and shear force along the slip-line \overline{AB} , respectively. σ_1 and n are found by evaluating the shear stress, shear strain and strain rate (equations 4.1) from a set of orthogonal cutting tests, see equations B.5 in Appendix B.

As proposed by Oxley et al. [6], [36] and Boothroyd [19], the temperature rise in the primary shear zone is predicted by

$$T_{AB} = T_{room} + \eta \left[\frac{(1 - \lambda_s) F_s \cos \alpha_o}{\rho c t_1 w \cos(\phi_s - \alpha_o)} \right] \quad (4.3)$$

The procedure to calculate temperature in the primary shear zone is shown in the Appendix A.

Again, the energy dissipation in the primary shear deformation zone is determined as expressed by

$$\begin{aligned}
 E_s &= \int_0^{\epsilon_{AB}} \sigma d\epsilon \\
 &= \frac{\sigma_1}{n+1} (\epsilon_{AB})^{n+1} \\
 &= \frac{\sigma_1}{n+1} \left[\frac{\cos \alpha_o}{\sqrt{3} \sin \phi_i \cos(\phi_i - \alpha_o)} \right]^{n+1}
 \end{aligned} \tag{4.4}$$

4.2.2 Plastic Deformation in the Chamfered Edge Zone

This section explains the modeling of plastic deformation due to the chamfer based on the analysis of strain, strain rate, temperature converted by the plastic work, and energy dissipation in chamfered edge zone.

Figure 4.2 illustrates a postulated slip-line field for cutting with chamfered tools. The primary shear deformation zone (AB) is connected to the slip-line field in the chamfered edge zone by a central fan BCI, see figure 4.2. Similar to extrusion process, the initial undeformed work geometry before entering the chamfered edge zone (h_o) plastically deforms and leaves the edge with a thickness of h_f . It is assumed that the dead metal trapped in the chamfered zone forms a slope identical to the primary shear angle, i.e. $\phi_{cf} = \phi_s$. Slip-line \overline{EF} meets free boundary surface at $\frac{\pi}{4}$. The velocity field corresponding to a slip-line field can be represented by a hodograph. If a valid hodograph, which satisfies the velocity boundary conditions, can be constructed for a field with the non-negative rate of energy dissipation throughout the field, the slip-line field is kinematically admissible [26]. The analysis of slip-line field is based on

a deformation field that is geometrically consistent with the shape change. Furthermore, the stress within the field are statically admissible.

The proposed model mainly focuses on the analysis of energy consumption in two aspects, which consist of the strain energy in the chamfered zone and the frictional energy along the dead metal interface.

From geometrical relation of slip-line field in the chamfered edge zone, the mean plastic strain and strain rate are formulated as

$$\left. \begin{aligned} \epsilon_{cf} &= \frac{h_o - h_f}{h_o} = 1 - \frac{b_{cf} \sin \alpha_1}{b_{cf} \sin \alpha_1 (1 + \tan \phi_s)} \\ \epsilon_{cf} &= 1 - \frac{1}{1 + \tan \phi_s} = \frac{\tan \phi_s}{1 + \tan \phi_s} \\ h_f &= b_{cf} \sin \alpha_1 \\ h_o &= b_{cf} \sin \alpha_1 (1 + \tan \phi_s) \\ \dot{\epsilon}_{cf} &= \frac{\epsilon_{cf} V_w \tan \phi_s}{b_{cf} \sin \alpha_1 \tan \phi_s} = \frac{\epsilon_{cf} V_w}{b_{cf} \sin \alpha_1} \end{aligned} \right\} \quad (4.5)$$

The energy dissipated in the chamfered edge zone is contributed by the plastic work (E_i) in extruding the material from thickness h_o to h_f and the friction energy (E_f) consumed at the dead metal interface (\overline{BO}). Similar to extrusion process, the “Dead Metal Zone” under the chamfered edge during cutting acts as a die. The plastic energy per unit volume consumed in the chamfered edge zone E_i is

$$E_i = \sigma_{cf} \epsilon_{cf} \quad (4.6)$$

where σ_{cf} is flow stress which varies with strain, strain rate, and temperature rise in the chamfered edge zone, see equations B.6 in Appendix B.

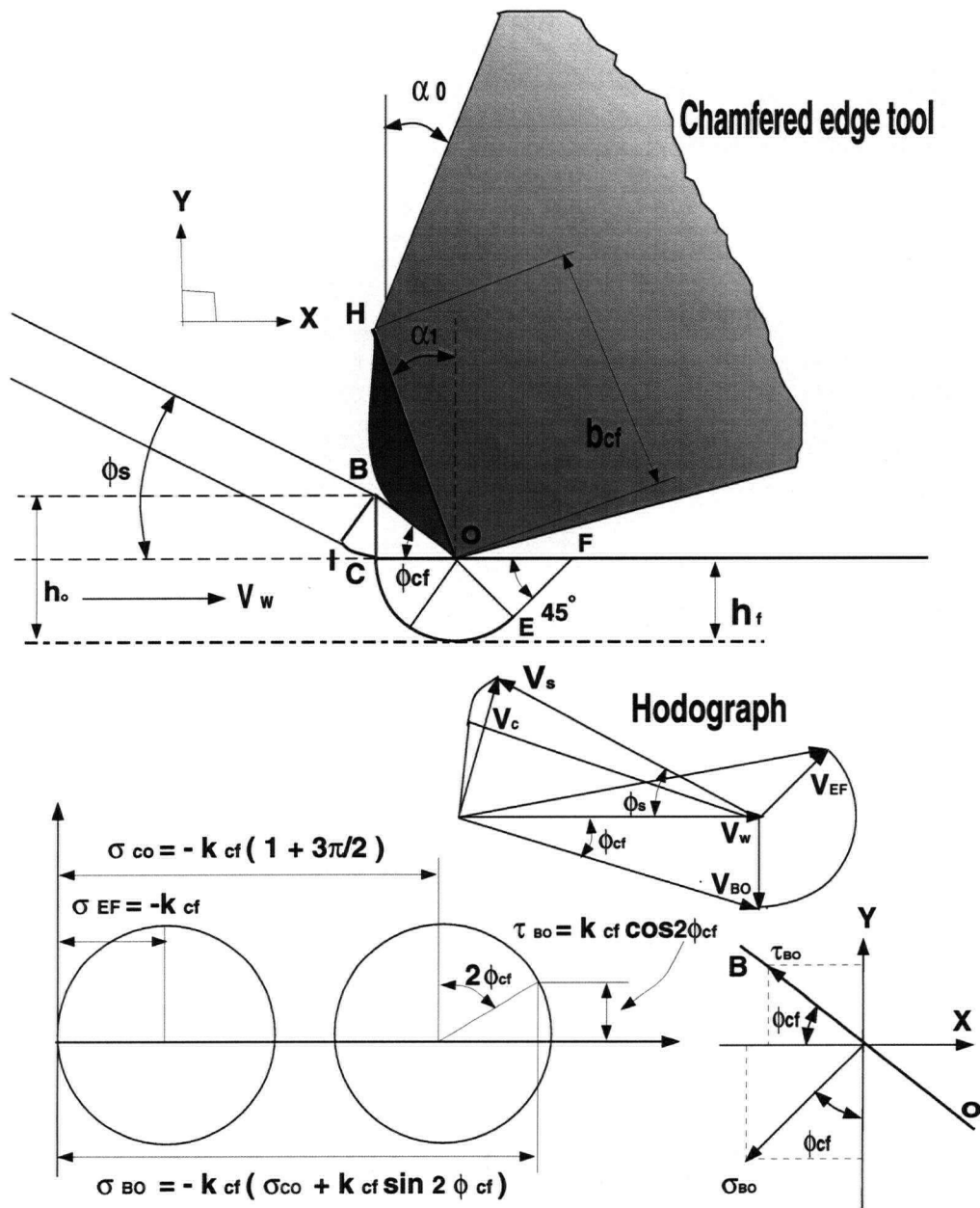


Figure 4.2: A proposed slip-line field for cutting with chamfered tools

Similar to extrusion process, the “ Dead Metal Zone ” under the chamfered edge during cutting acts as a die. \overline{BO} is the boundary to separate deforming work material and die surface. The energy per unit volume E_f by friction work done at interface \overline{BO} is mainly affected by the product of friction force F_{BO} and shearing velocity V_{BO} along the interface \overline{BO} .

$$\left. \begin{aligned} F_{BO} &= \frac{\tau_{BO} b_{cf} \sin \alpha_1 w}{\cos \phi_s} \\ V_{BO} &= \frac{V_w}{\cos \phi_s} \\ \tau_{BO} &= \cos 2\phi_s k_{cf} \\ k_{cf} &= \frac{\sigma_{cf}}{\sqrt{3}} \end{aligned} \right\} \quad (4.7)$$

where τ_{BO} and k_{cf} is shear stress exerted along interface \overline{BO} and shear flow stress along slip-line \overline{CO} in the chamfered edge zone, respectively. τ_{BO} is found from Mohr circle as shown in 4.2. The energy per unit volume E_f by friction work done at interface \overline{BO} is formulated by

$$\left. \begin{aligned} E_f &= \frac{F_{BO} V_{BO}}{V_w h_o w} \\ &= \frac{\tau_{BO} b_{cf} \sin \alpha_1 w V_{BO}}{V_w h_o w \cos \phi_s} \\ &= \frac{\cos 2\phi_s k_{cf}}{\cos^2 \phi_s (1 + \tan \phi_s)} \\ &= \frac{\cos 2\phi_s \sigma_{cf}}{\sqrt{3} \cos^2 \phi_s (1 + \tan \phi_s)} \end{aligned} \right\} \quad (4.8)$$

Hence, the total energy consumed in the chamfered edge zone E_{cf} is determined by superposing strain energy E_i and friction energy E_f .

$$E_{cf} = E_i + E_f$$

$$= \sigma_{cf} \epsilon_{cf} + \frac{\sigma_{cf} \cos 2\phi_s}{\sqrt{3} \cos^2 \phi_s (1 + \tan \phi_s)} \quad (4.9)$$

Heat generated by the plastic energy E_{cf} causes temperature rise in the chamfered zone. Temperature rise in the chamfered zone T_{cf} is given by

$$T_{cf} = T_{AB} + \frac{E_{cf}}{\rho c} \quad (4.10)$$

4.2.3 Plastic Deformation in the Tool-Chip Interface Zone

In the modeling of machining with chamfered tools, the evaluation of strain rate, temperature, and energy dissipation in the secondary deformation zone is carried out using the same approach as presented in chapter 3.

The strain rate ($\dot{\gamma}_{inter}$) at the tool-chip interface is approximated by Oxley et al. [6], [36] as

$$\left. \begin{aligned} \dot{\gamma}_{inter} &= \frac{V_c}{\delta \cdot t_2} \\ V_c &= \frac{V_w \sin \phi_s}{\cos(\phi_s - \alpha_o)} \\ t_2 &= \frac{t_1 \cos(\phi_s - \alpha_o)}{\sin \phi_s} \end{aligned} \right\} \quad (4.11)$$

where V_c and t_2 are the rigid chip velocity and the chip thickness, respectively. δ is the ratio of thickness of plastic deformation zone at the tool-chip interface to the chip thickness t_2 . δ is taken to be 0.05 as explained in chapter 3.

Both thermal and energy analysis in tool-chip interface zone require the tool-chip contact length l_c as a known parameter. Gad and Armarego et al. [35] reviewed several approaches to determine tool-chip contact length in the literature. They concluded that the most adequate method of contact length estimation is to use empirical equations obtained from measurements

in machining tests. In this model, the following relationship is assumed between the contact length (l_c) and uncut chip thickness (t_1)

$$l_c = m_1 t_1 \quad (4.12)$$

where m_1 is an empirical constant evaluated from orthogonal machining tests on P20 mold steel. m_1 is found to be about 3.20 for S10 carbide tools and 1.3 for MB820 CBN tools, respectively.

The temperature rise (T_{inter}) at the tool-chip interface for chamfered tools is given by

$$T_{inter} = T_{cf} + \psi \Delta T_M \quad (^\circ C) \quad (4.13)$$

where T_{cf} is temperature in the chamfered zone. The determination of ΔT_M is explained in Appendix A.

Once temperature at the tool-chip interface T_{inter} is evaluated. The velocity modified temperature T_{modint} at the tool-chip interface is evaluated by

$$T_{modint} = (T_{inter} + 273.0)(1 - 0.09 \log_{10}(\frac{\dot{\gamma}_{inter}}{\sqrt{3}})) \quad (4.14)$$

Then, the flow stress at tool-chip interface is mapped from velocity modified temperature $T_{modinter}$ as shown in Appendix B.

As flow stress σ_{inter} and contact length l_c are identified, the energy per unit volume dissipated in tool-chip interface zone E_{inter} is found by

$$\left. \begin{aligned} E_{inter} &= \frac{F_{fc} V_c}{V_w t_1 w} \\ &= \frac{3 \sigma_{inter} l_c w V_c}{4 V_w t_1 w} \\ &= \frac{3 \sigma_{inter} l_c \sin \phi_i}{4 t_1 \cos(\phi_i - \alpha_o)} \end{aligned} \right\} \quad (4.15)$$

4.2.4 Prediction of Cutting Process with Chamfered Tool

Similar to the model development in chapter 3, the inputs here are cutting conditions, tool geometrical parameters (including chamfer geometry), and work material mechanical properties. The outputs are the predicted shear angle, cutting forces, strain and strain rate, and temperature in the primary shear and the tool-chip interface zones.

The total cutting energy per unit volume E_c is obtained by summing up the energy dissipated in the three plastic deformation zones (equations 4.4, 4.9, 4.15).

$$E_c = \frac{\sigma_1}{n+1} \left[\frac{\cos \alpha_o}{\sqrt{3} \sin \phi_s \cos(\phi_s - \alpha_o)} \right]^{n+1} + \sigma_{cf} \epsilon_{cf} + \frac{\sigma_{cf} \cos 2\phi_s}{\sqrt{3} \cos^2 \phi_s (1 + \tan \phi_s)} + \frac{3\sigma_{inter} l_c \sin \phi_s}{4\sqrt{3} t_1 \cos(\phi_s - \alpha_o)} \quad (4.16)$$

The total energy is dependent on the shear angle, tool-chip contact length, flow stress in each plastic work zone, rake angle and chamfer geometry. However, the flow stress in each zone is also dependent on the local shear strain, strain rate and temperature, which are in turn dependent on the shear angle. It is proposed that applying the minimum energy principle can solve such a complex deformation process. The iterative solution procedure is summarized in figure 4.3, where the input data contains cutting speed, width of cut, uncut chip load, tool-chip contact length and tool geometry.

The iteration starts with an initial guess value of shear angle. The corresponding temperature, shear strain, strain rate and flow stresses in the three plastic zones are evaluated from orthogonal cutting database. The flow stress of the material is modified as a function of temperature, strain and strain rate as explained before. The total cutting energy is then evaluated from Eqn. 4.16. The iteration is repeated by scanning the realistic shear angle range ($\phi_1 = 5^\circ$

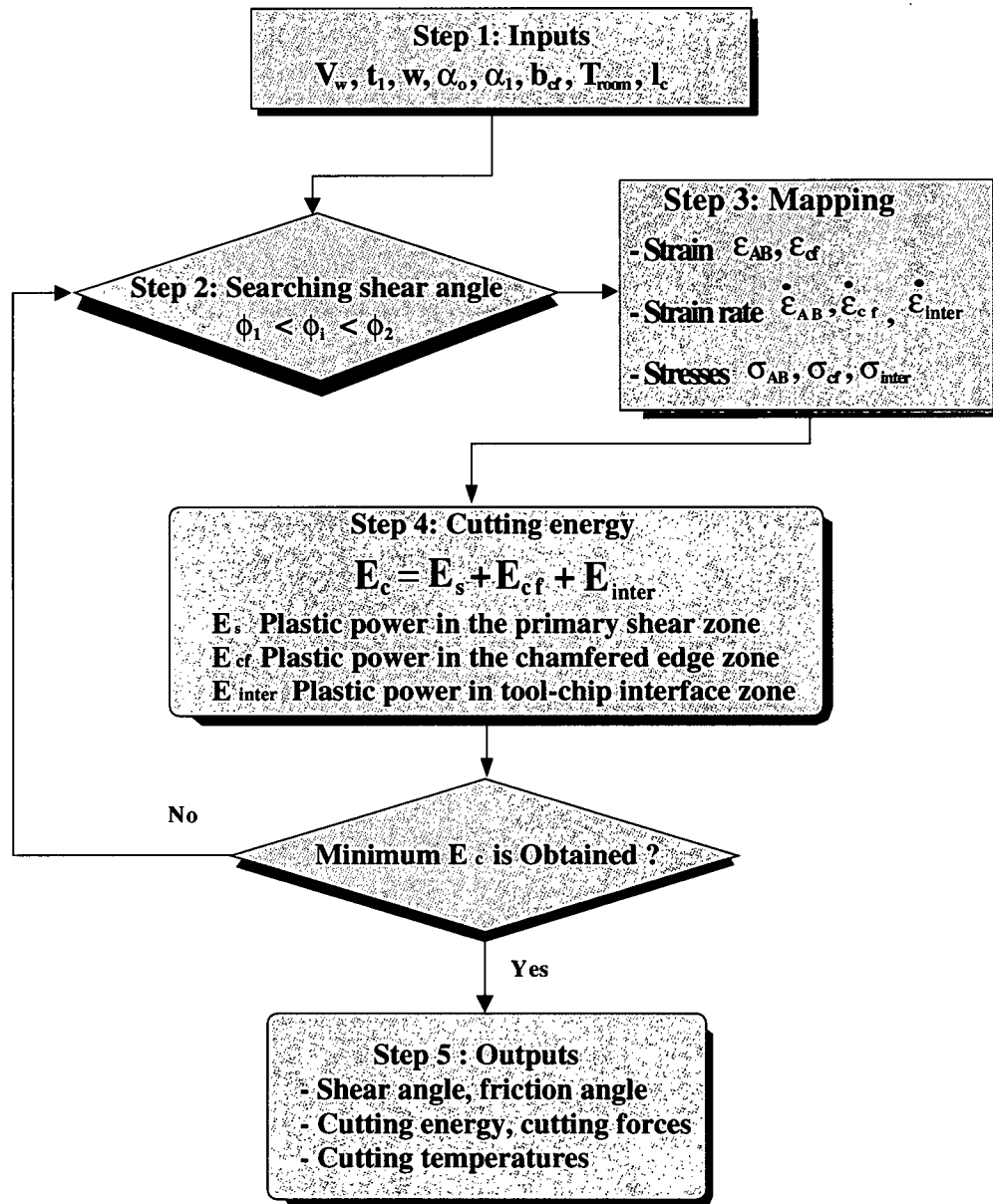


Figure 4.3: A generalized prediction algorithm for cutting with chamfered tools

to $\phi_2 = 45^\circ$), and the shear angle which corresponds to the minimum energy is accepted as a solution. The minimum energy principle was first applied by Merchant [21] for orthogonal cutting without strain and thermal affects. Shamato and Altintas [2] applied the same principle to oblique cutting, again without strain and thermal affects. However, they used shear stress and friction coefficients evaluated from orthogonal cutting tests, which improved the prediction accuracy significantly. The past studies considered only cutting with sharp edge tools. Unfortunately, the same approaches can not be applied due to the chamfer. Furthermore, the aim of the work is to predict the behavior of cutting process at high cutting speed range where the thermal softening and strain - strain rate dependent flow stress play an important role, which are considered in the proposed model.

Similar to the analysis of temperature for a sharp tool model presented in chapter 3. An iterative procedure is applied to evaluate temperature in three characterized plastic deformation zones as illustrated in figure 4.4.

For each selected trial shear angle ϕ_i , the inputs to calculate cutting temperature in three zones consist of undeformed chip thickness t_1 , tool main rake angle α_o , width of w , room temperature T_{room} , shear force F_s , friction force F_{fc} , and energy consumption in the chamfered edge zone E_{cf} , respectively. Thermal conductivity (κ) and specific heat (c) as a function of corresponding temperature evaluated in each plastic deformation zone are given in Appendix A. The empirical factor, the proportion of heat conducted into work material (λ_s), is given in Appendix A. The initial temperature of work material or room temperature is assigned to calculate the temperature in the primary shear zone as proposed by Boothroyd [19] and Oxley et al. [6], [36]. The temperature at the tool-chip interface is expressed approximately by summing up the temperature rise in the chamfered zone T_{cf} and maximum temperature rise in the chip material on passing along the tool rake face ΔT_M .

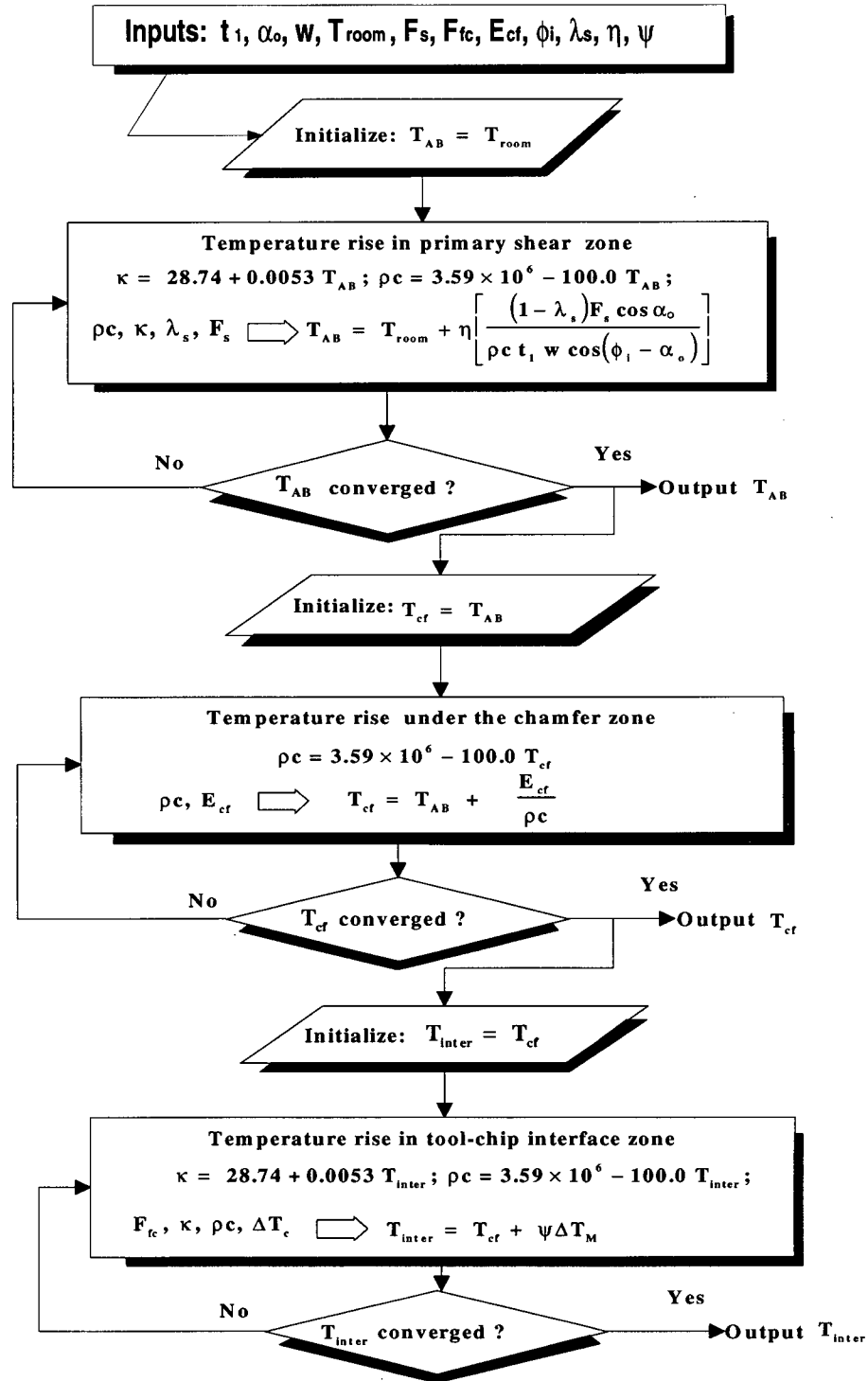


Figure 4.4: A procedure to estimate cutting temperatures for cutting with chamfered tools.

Once the shear angle is identified, the friction angle at tool-chip interface is predicted by

$$\left. \begin{aligned} \beta &= \theta - \phi_s + \alpha_o \\ \tan\theta &= [1 + 2(\frac{\pi}{4} - \phi_s)] - S_c n \end{aligned} \right\} \quad (4.17)$$

where θ defines the inclination between the resultant force vector R_s and slip-line \overline{AB} (see Fig. 4.1). S_c is taken as $S_c \approx 6.0$. The total tangential (F_c) and feed (F_t) cutting forces are in the direction of cutting velocity V_w and perpendicular to it. They are obtained by resolving the forces contributed from primary shear zone (F'_c, F'_t), chamfered zone (F_{c-cf}, F_{t-cf}) and edge forces generated by the flank-finish surface contact (F_{ce}, F_{fe}) in the two directions aforementioned.

$$\left. \begin{aligned} F_c &= F'_c + F_{c-cf} + F_{ce} \\ F_t &= F'_t + F_{t-cf} + F_{te} \end{aligned} \right\} \quad (4.18)$$

The cutting forces generated in each deformation zone are evaluated as follows. The edge forces are identified from machining tests by extrapolating the cutting forces at zero chip thickness (Budak, Altintas, and Armarego,[1]). The shear force on shear plane (AB) is evaluated from equations 4.2, which leads to resultant force $R_s = F_s / \cos\theta$. Note that the resultant force (R_s) does not contain the forces contributed by the chamfered zone, but it is counterbalanced by the forces acting on the regular part of the tool rake face (HG), see figure 4.1. The contributions of primary shear zone to tangential and feed forces (F'_c, F'_t) are given from the geometrical relations

$$\left. \begin{aligned} F'_c &= \frac{F_s \cos(\beta - \alpha_o)}{\cos(\phi_s + \beta - \alpha_o)} \\ F'_t &= \frac{F_s \sin(\beta - \alpha_o)}{\cos(\phi_s + \beta - \alpha_o)} \end{aligned} \right\} \quad (4.19)$$

The force components F_{c-cf} and F_{t-cf} generated at the chamfered zone are evaluated from the normal and tangential stresses distributed along the dead metal interface \overline{BO} . Using Hencky's equations (Johnson et al. [26]) with Mohr circle shown in figure 4.2

$$\left. \begin{aligned} \sigma_{EF} &= -k_{cf} && \text{along } \overline{EF} \\ \sigma_{CO} &= -k_{cf}(1 + \frac{3\pi}{2}) && \text{along } \overline{EC} \\ \sigma_{BO} &= -(\sigma_{CO} + k_{cf} \sin 2\phi_s) && \text{along } \overline{BO} \\ \tau_{BO} &= \cos 2\phi_s k_{cf} && \text{along } \overline{BO} \end{aligned} \right\} \quad (4.20)$$

The corresponding forces in chamfered zone are

$$\left. \begin{aligned} F_{c-cf} &= \left[(\tau_{BO} \cos \phi_s + \sigma_{BO} \sin \phi_s) \frac{b_{cf} \sin \alpha_1 w}{\cos \phi_s} \right] \\ F_{t-cf} &= \left[(\sigma_{BO} \cos \phi_s - \tau_{BO} \sin \phi_s) \frac{b_{cf} \sin \alpha_1 w}{\cos \phi_s} \right] \end{aligned} \right\} \quad (4.21)$$

Where b_{cf} , α_1 , and w are the length of chamfer, chamfer angle (second rake angle), and width of cut, respectively. Note that the cutting forces are predicted from the shear angle evaluated from the minimum energy principle, and the fundamental properties of material while considering the strain, strain rate and temperature. Hence, the proposed model is different than mechanistic models, and it is based on comprehensive extension of analytic approach proposed by Oxley [6].

4.3 Model Verification

This section shows the experimental method and demonstrates estimation of the cutting process variables in high speed machining of P20 mold steel with chamfered tools using the model presented in this chapter. The cutting model developed for the chamfered tools provides

the prediction of cutting process, such as shear angle ϕ , friction angle β , cutting energy E_c , cutting forces F_c and F_t , and cutting temperature in the primary shear T_{AB} and the tool-chip interface T_{inter} zones.

4.3.1 Chamfer Tools Used in Machining Tests

Two different cutting tool materials are used in the experiments. The first set was blank carbide ISO S10 tools from SANDVIK (N151.2-650-50-3B). They were ground to have different chamfer angle (α_1) and width (b_{cf}) as listed in Table 4.1. Although a range of cutting speed was tried, two key cutting speeds ($V_w = 240, 600 \text{ m/min}$) are reported with $t_1 = 0.1 \text{ mm/rev}$ chip load. The second set is MITSUBISHI MB820 Cubic Boron Nitride (CBN) with chamfered edges, see Table 4.2 for tool geometry and cutting conditions. The CBN cutting tests have been conducted at cutting speeds 240, 600, 1000 m/min with a chip load of $t = 0.06 \text{ mm/rev}$.

Table 4.1: Cutting conditions and chamfer geometry for the prepared chamfered edge tools used in machining tests. width of cut $w=3.6 \text{ mm}$, main rake angle $\alpha_o = 0^\circ$. P20 work material: hardness 34 HRC, Composition: C 0.37%, S_i 0.3%, M_n 1.4%, C_r 2.0%, N_i 1.0%, M_o 0.2%. SANDVIK S10 carbide tool: WC 36.1%, T_iC 39.3%, T_aC 8.6%, C_o 11.0%.

Feedrate $t_1=0.1 \text{ mm/rev}$ Cutting speed $V_w=240 \text{ m/min}$			Feedrate $t_1=0.1 \text{ mm/rev}$ Cutting speed $V_w=600 \text{ m/min}$		
Tool number	$b_{cf} \text{ (mm)}$	$\alpha_1 \text{ (deg.)}$	Tool number	$b_{cf} \text{ (mm)}$	$\alpha_1 \text{ (deg.)}$
CFT20-02	0.0902	-10°	CFT20-01	0.0928	-10°
CFT04	0.1660	-15°	CFT02	0.0902	-15°
CFT12	0.0841	-25°	CFT09	0.0896	-25°
CFT15	0.0863	-35°	CFT18	0.8990	-35°

Table 4.2: Cutting conditions and chamfer geometry for the CBN (MITSUBISHI MB820) chamfered edge tools used in machining tests. Average width of cut $w=2.55$ mm, main rake angle $\alpha_o = -5^\circ$. CBN tool material composition: CBN 50%, (TiN and Al_2O_3) 50%.

Tool No.	Cutting speed V_w m/min	Undeformed chip thickness t_1 (mm)	b_{cf} (mm)	α_1 (deg)
CBN01	240	0.06	0.10	-25°
CBN02	600	0.06	0.10	-25°
CBN03	1000	0.06	0.10	-25°

4.3.2 Predicted and Experimental Results

A series of simulations are carried out using the proposed cutting model for chamfered tools. These results are useful to analyzed the effect of chamfer geometry and cutting conditions on the chip formation in high speed machining of P20 mold steel. To verify the proposed model, some experimental results for both chamfered carbide and CBN tools are compared with the predicted results. The cutting performance in terms of tool wear observed from experiments is compared as well.

Effect of Chamfer Angle on Cutting Process

The effect of chamfer angle on the cutting process with S10 chamfered carbide tools is analyzed by the proposed analytic model. The model predicts shear angle, average friction angle on the rake face, and cutting forces, temperature, strain and strain rate in primary, secondary and dead plastic zones. The chamfer length of $b_{cf} = 0.090mm$ is used in all model simulations, which is equal to an average value of prepared chamfered carbide tools. In all simulations, chamfer angle varies from -5° to -40° .

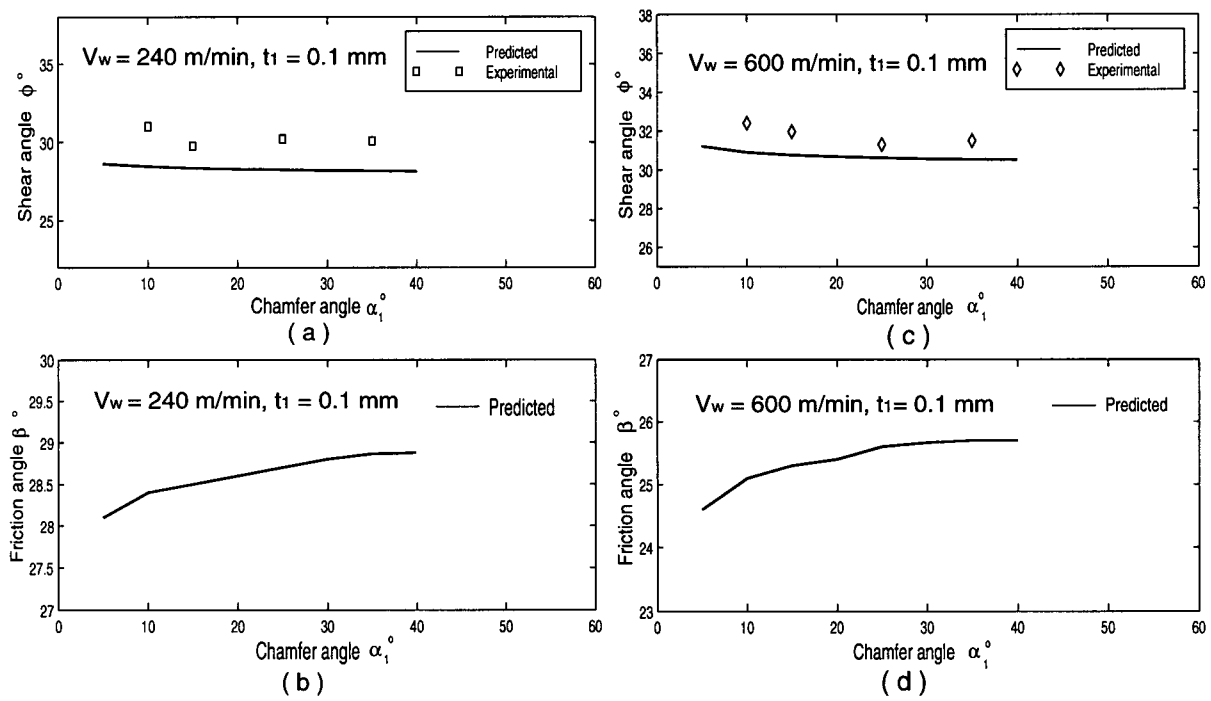


Figure 4.5: Effect of chamfer angle on the predicted and experimental shear angles ϕ (a), (c)) and predicted friction angles β (b), (d) (S10 chamfered carbide tools).

Figure 4.5 shows the predicted shear angles and friction angles versus various chamfer angles at cutting speeds 240, 600 m/min. Experimental shear angle is evaluated from equation 3.43 as demonstrated in chapter 3. Predicted and experimentally evaluated shear angles are in close agreement, and they remain approximately constant regardless of the changes in the chamfer angle. This can be explained by the presence of dead metal zone over the chamfer face, and the dead metal zone forms a shape similar to the sharp cutting edge, which do not change the shearing action in the primary zone. Predicted shear angles show about $2^\circ \sim 3^\circ$ decrease compared to the predicted shear angles for cutting with sharp tools under the same cutting conditions. However, the friction between the dead metal zone and moving chip creates additional forces. This hypothesis is verified by evaluating the friction angle which increases about 28° at cutting speed 240 m/min, and 26° at cutting speed 600 m/min, when the chamfer angle is changed from -5° to -40° at cutting speed (equation 4.17). In the case of cutting with sharp tools, predicted friction angles remain about 24° for both cutting speed at 240 and 600 m/min (chip load $t_1=0.1$ mm/rev).

Figure 4.6 shows the predicted total cutting forces and chamfer forces against different chamfer angles. Total predicted cutting forces (predicted by equation 4.18) are compared with experimentally measured total tangential (F_c) and feed (F_t) forces at cutting speeds 240, 600 m/min. For an analytical prediction, the agreement between the measured and estimated cutting forces is quite acceptable. Hirao and Tlustý [3] observed from machining tests that although the chips obtained with or without chamfer edges were similar, the total cutting forces were quite different. This can be clearly explained by the physic based analytic model, where the chamfer zone forces (given by equations 4.21) increase with the increasing chamfer angle. Since all cutting conditions are identical except the chamfer angles, the increase in the cutting forces is mainly due to forces contributed by the chamfer zone, see figure 4.6. Chamfer forces in the feed direction (F_{t-cf}) have higher amplitudes than the tangential component,

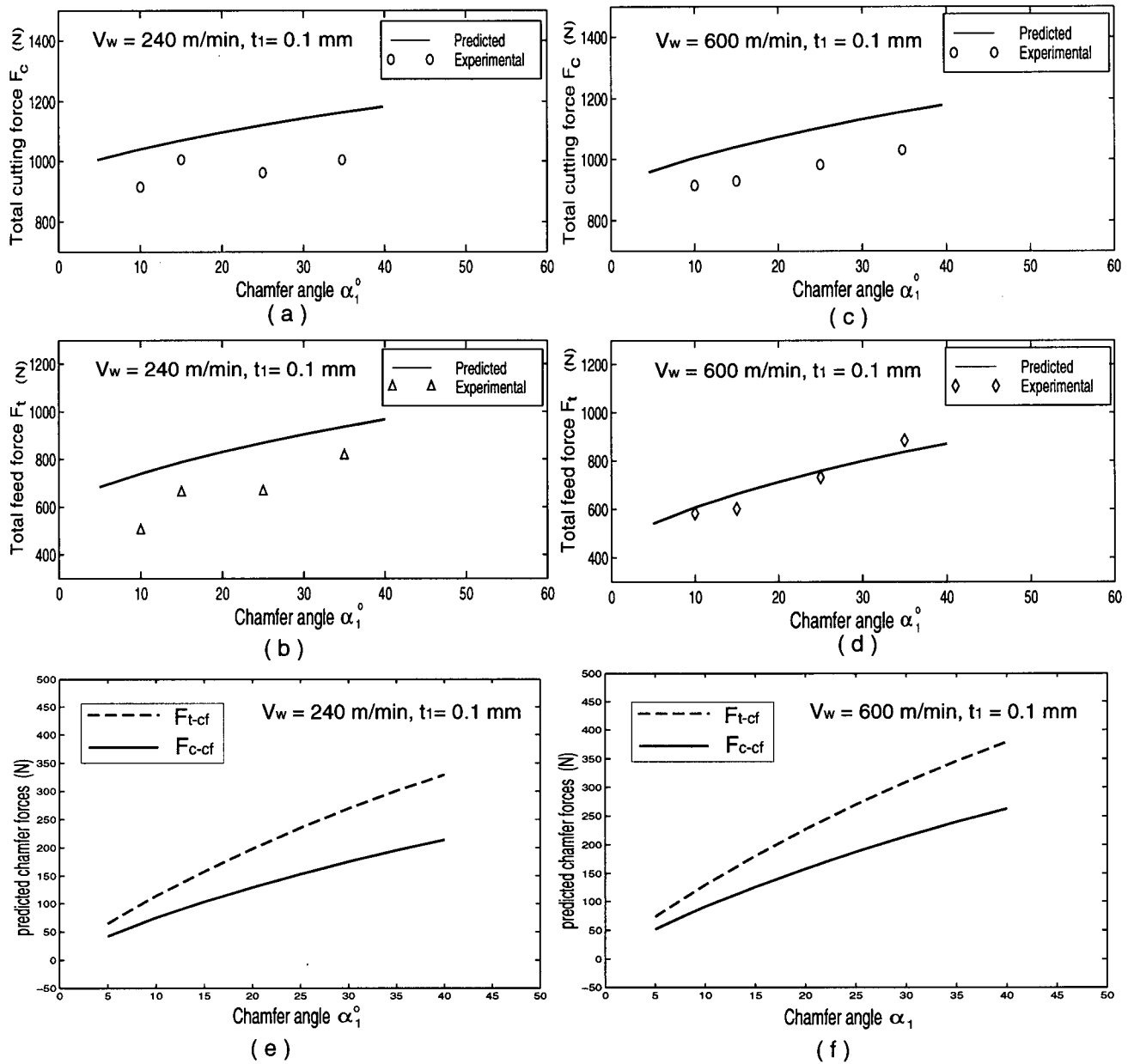


Figure 4.6: Effect of chamfer angle α_1 on the total cutting forces ((a), (b), (c), (d) and chamfer forces ((e), (f)) (S10 chamfered carbide tools).

since the pressure on the chamfer face has stronger component in the feed direction as the chamfer angle increases. For the comparison, the cutting (F_c) and feed (F_t) forces measured from cutting with S10 carbide sharp tools at cutting speed 240 m/min and undeformed chip thickness $t_1 = 0.1 \text{ mm}$ are $F_c=817 \text{ N}$ and $F_t=390 \text{ N}$, respectively. Similarly, experimentally measured cutting and feed forces are $F_c=890 \text{ N}$ and $F_t= 445 \text{ N}$ at cutting speed $V_w=600 \text{ m/min}$ and undeformed chip thickness $t_1=0.1 \text{ mm}$. All the predicted and measured cutting and feed forces for cutting with chamfer tools are higher than those for cutting with sharp tools.

The effect of chamfer angle on the predicted cutting temperature in the primary shear T_{AB} and the tool-chip interface T_{inter} zones is shown in figure 4.7. Both predicted temperature rise in the primary shear and the tool-chip interface zones show little dependency on the variation of chamfer angles. In general, temperature at the tool-chip interface T_{inter} is about $100 \sim 200^\circ\text{C}$ higher than that predicted by sharp tools. Since shear angles and friction angles at the tool-chip interface are not affected by the variation of chamfer angles significantly. Therefore, cutting temperature does not vary with chamfer angle significantly when cutting speed and undeformed chip thickness remain constants.

The predicted and experimentally evaluated cutting energy E_c versus chamfer angle is shown in figure 4.7. Experimentally determined cutting energy per unit volume is found using same equation 3.65 shown in chapter 3. The same trend as the predicted shear angles against chamfer angles can be seen for the predicted cutting energy. Predicted cutting energy E_c shows little dependency on the variation of chamfer angles. The predicted cutting energy E_c shows a close agreement with that evaluated from experiments.

Effect of Cutting Speed on Cutting Process

Since CBN tools are more thermal resistant, they are used to evaluate the influence of

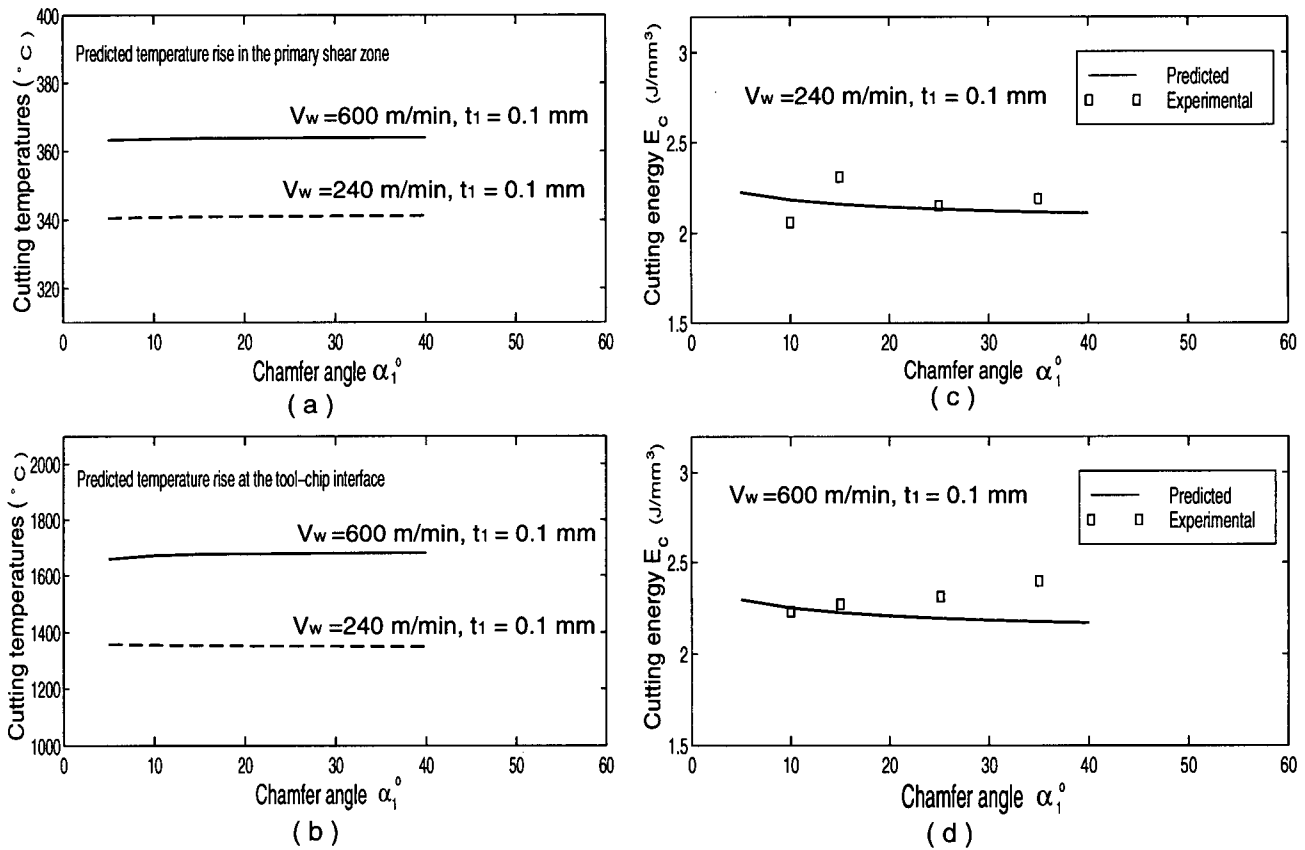


Figure 4.7: Effect of chamfer angle α_1 on the cutting temperature (T_{AB} , T_{inter}) (a), (b) and energy (E_c) (c), (d), (S10 chamfered carbide tools).

cutting speed on cutting process. The tests were conducted at three cutting speeds: 240, 600, and 1000 m/min with a chamfer geometry: $\alpha_1 = -25^\circ$, $b_{cf}=0.1$ mm. In all simulations, cutting speed varies from 240 to 1100 m/min.

Figure 4.8 shows the predicted and experimental shear angles and the predicted friction angles against cutting speed for CBN tools. The predicted and experimentally evaluated shear angles are in close agreement. Again, experimental shear angle is obtained by evaluating the chip ratio as shown in equation 3.43. Both the predicted and experimental shear angles show a slight increase as cutting speed is increased from 240 to 600 m/min. The effect of the further increase of cutting speed on shear angle becomes insignificant. The predicted friction angle decreases from about 19° to 16° when cutting speed is changed from 240 to 1000 m/min. It also can be seen that the predicted friction angle increases from 16° to 19° as cutting speed is increased from 600 m/min to 1000 m/min. Experimental evidence suggests that the similar trend is observed for the measured contact length along the tool-chip interface.

Figure 4.9 shows the effect of cutting speed on the predicted and experimentally measured cutting forces (F_c , F_t) and the predicted chamfer forces (F_{c-cf} , F_{t-cf}). The predicted cutting forces (F_c , F_t) show a good agreement with those measured from experiments. The cutting forces F_c and F_t measured from cutting tests show a little variation with the cutting speed since the friction at the tool-chip interface varies with cutting speed insignificantly within the cutting speeds V_w : 240 ~ 1000 m/min. Turning tests with MITSUBISHI chamfered CBN tools at cutting speeds 400, 600, 800 m/min also show the similar trend in the machining of P20 mold steel ([70]). The predicted chamfer forces (F_{c-cf} , F_{t-cf}) indicates that chamfer forces seem to remain constants when cutting speed is changed from 240 to 1000 m/min. Chamfer forces are predicted by equations 4.21. Again, the predicted chamfer forces (F_{t-cf}) in feed direction are higher than those in cutting direction (F_{c-cf}). Machining tests with both chamfered carbide

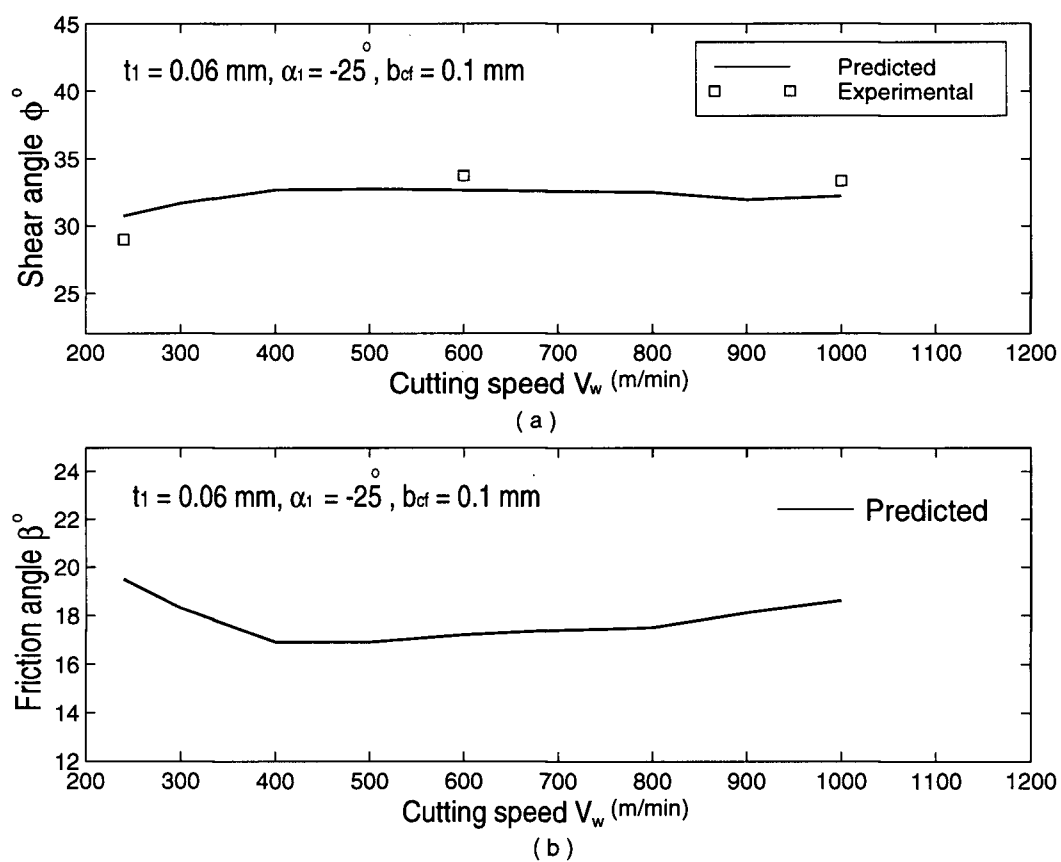


Figure 4.8: Effect of cutting speed on the predicted and experimental shear angle ϕ (a) and predicted friction angle β (b) (MB820 CBN chamfered tools).

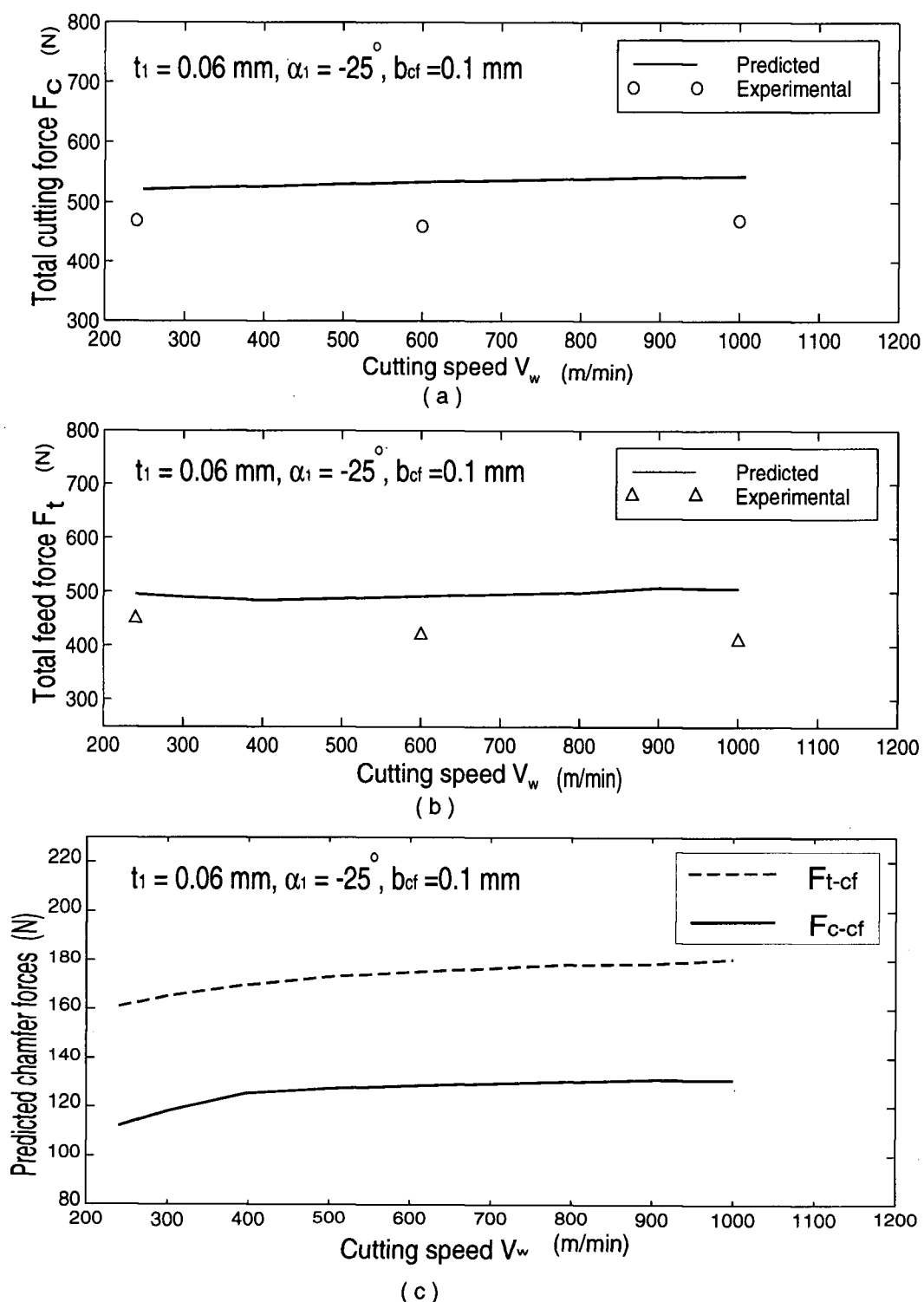


Figure 4.9: Effect of cutting speed V_w on the total cutting forces ((a), (b)) and chamfer forces (c) (MB820 CBN chamfered tools).

and CBN tools show this characteristic.

The effect of cutting speed on the predicted cutting temperature in the primary shear and the tool-chip interface zone is shown in figure 4.10. It can be seen that although the predicted temperature rise is only about 50° in the primary shear zone, temperature in the tool-chip interface increases from 1100° to 1700° when cutting speed is increased from 240 m/min to 600 m/min. The effect of temperature rise in tool-chip interface zone on the tool wear will be discussed later. As discussed in chapter 3, cutting speed has profound effect on the cutting temperature at the tool-chip interface T_{inter} . Figure 4.10 (c) shows the effect of cutting speed on the predicted and experimentally evaluated cutting energy E_c . The predicted and experimental cutting energy are in close agreement at cutting speed range: 240 m/min \sim 1000 m/min. Since shear angle and cutting forces are not changed significantly when cutting speed is increased from 240 m/min to 1000 m/min, both the predicted and experimental cutting energy E_c remain nearly constants.

Observation of Tool Wear

It is of interest to evaluate the wear behavior of chamfered tools with different chamfer geometry and compare it with sharp tools. Tool wear tests have been performed and the chamfered tools used in tool wear tests and cutting conditions are given in Tables 4.1 and 4.2.

Tool wear tests have been carried out to investigate the effect of chamfer angle and cutting speed on the tool wear V_B . Figure 4.11 (a), (b) show the comparison of tool wear V_B of S10 carbide tools with different chamfer angles at cutting speed 240 m/min and 600 m/min. Figure 4.11 (c) shows the effect of cutting speed on the tool wear of chamfered CBN tools. It is reported that the diffusion temperature for Cobalt binding material used in S10 carbide tools is about

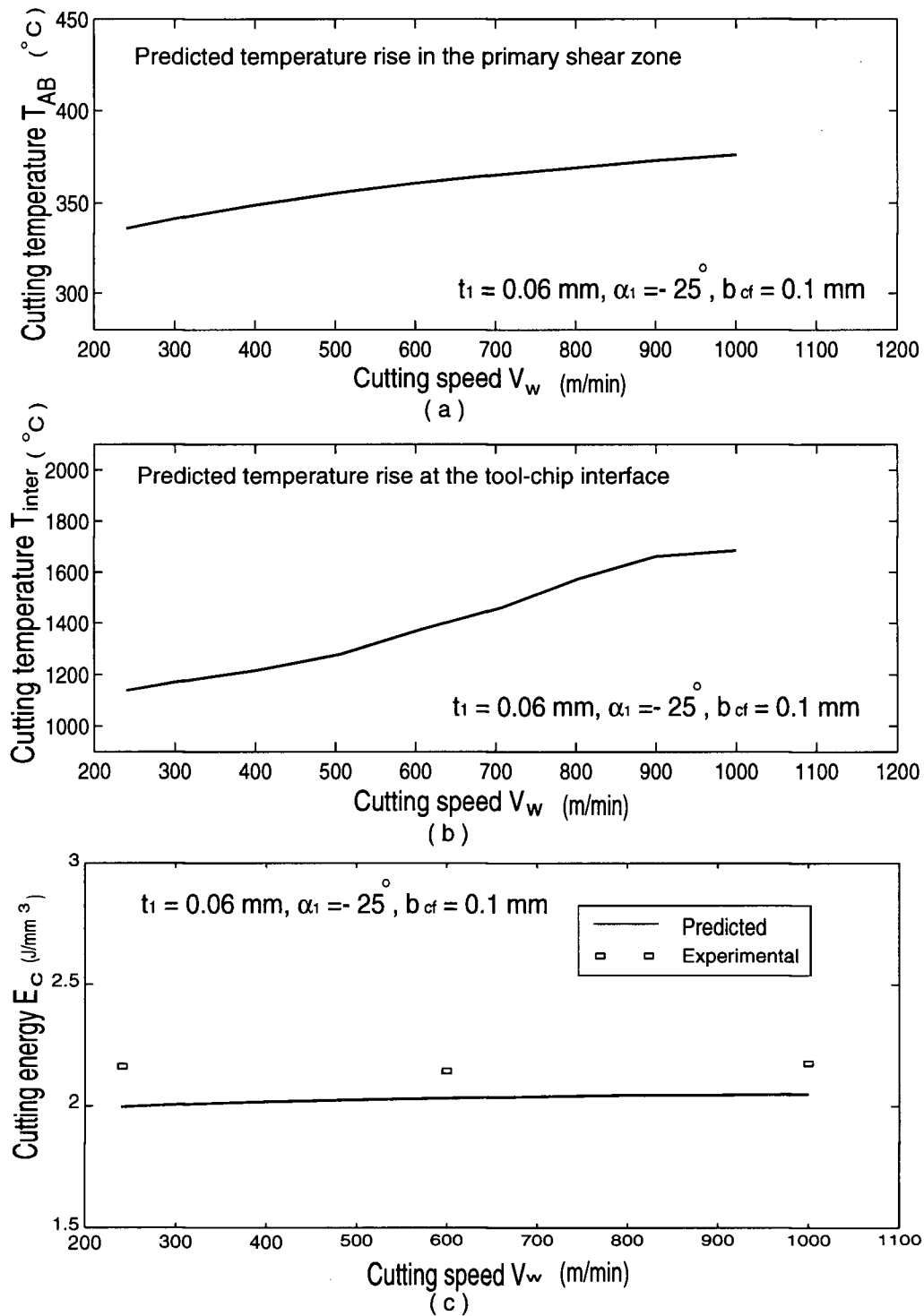


Figure 4.10: Effect of cutting speed V_w on the predicted cutting temperature in the primary shear and the tool-chip interface zones ((a), (b)), the predicted and experimental cutting energy (c) (MB820 CBN chamfered tools).

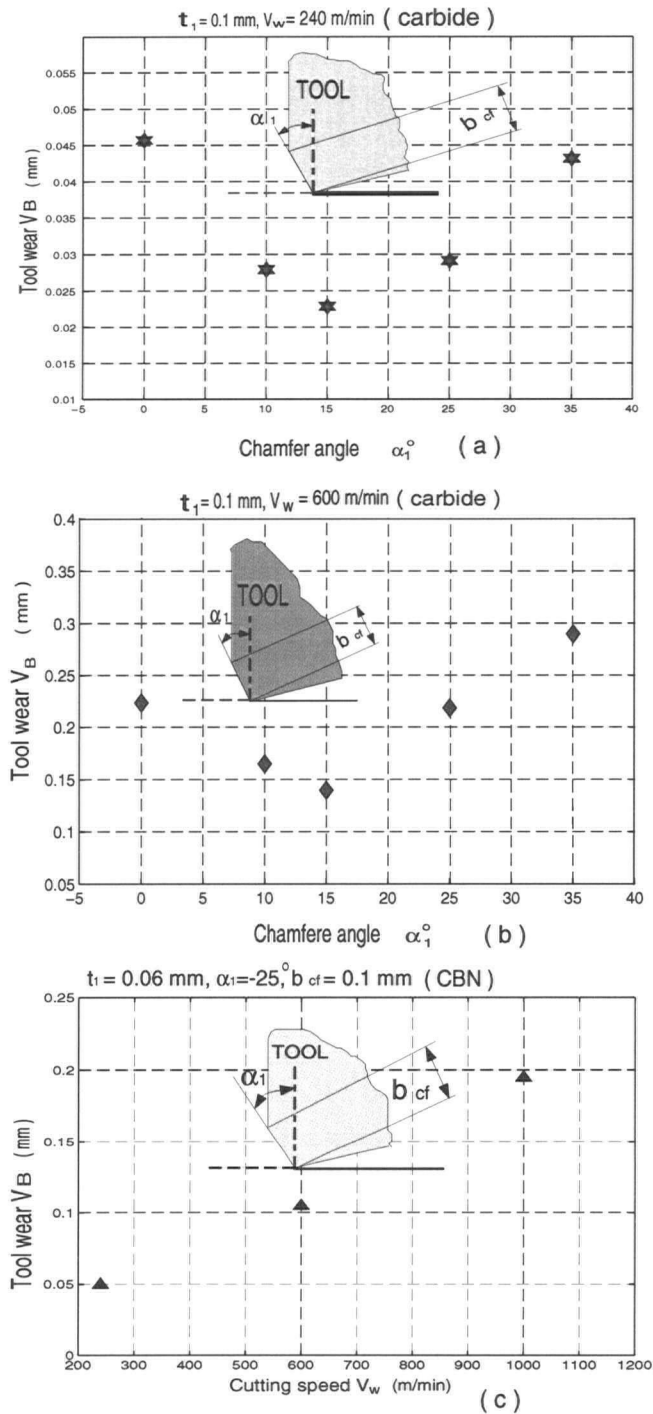


Figure 4.11: Comparison of tool wear V_B for chamfered carbide (a), (b), and CBN (c) tools from machining tests.

1300°C and 1600°C for binding material (Al_2O_3) used in CBN tools [72]. Hence, ISO S10 carbide tool must be used under 1300°C. It means that cutting speed should be selected under 240 m/min for machining P20 mold steel with S10 carbide tools. CBN may sustain without diffusing its binding materials up to 600 m/min. When the chamfer angle of the carbide tool is varied from 0° (i.e. sharp cutting edge) to -35°, the minimum wear was obtained with tools which had -15° chamfer angle.

Larger chamfer angles increased the force and friction, and smaller chamfer angles weaken the wedge, hence causing more flank wear. The trend was the same at both cutting speeds (240, 600 m/min). However, for the same volume of the material removed, the 240 m/min cutting speed gave 6 times lower flank wear than the cutting speed 600 m/min where severe crater wear due to diffusion of Cobalt binding was observed. While SEM pictures showed frequent micro-cracks and chipping in sharp cutting edges, there were no damage on the tools with -15° chamfer angle used at 240 m/min cutting speed. Evidently, 240 m/min speed corresponds to about 1300°C temperature on the rake face, which is just below the melting temperature of P20 and diffusion of Cobalt binding within the ISO S10 carbide tool. Hence, both analytic model and experiments indicate that ISO S10 carbide tools with chamfer angle is -15° at 240 m/min must be used in continuous machining of P20 mold steels at dry cutting conditions. For tool wear tests using chamfer CBN tools, it shows that tool wear is proportional to the increase of cutting speed as seen figure 4.11 (c) since higher cutting speed causes higher temperature rise at the tool-chip interface. Compared to the S10 carbide tools, much higher speeds (500m/min) can be used with CBN tools since CBN tools did not exhibit significant crater wear and micro-cracks up to 600 m/min cutting speed.

Figure 4.12 and 4.13 show the comparison of variation of tool wear V_B with cutting length between a sharp edge tool and a chamfered tool with -15° chamfer angle at the cutting conditions: $t_1=0.1$ mm, $V_w=240$ and 600 m/min, respectively. A chamfered tool with -15° chamfer

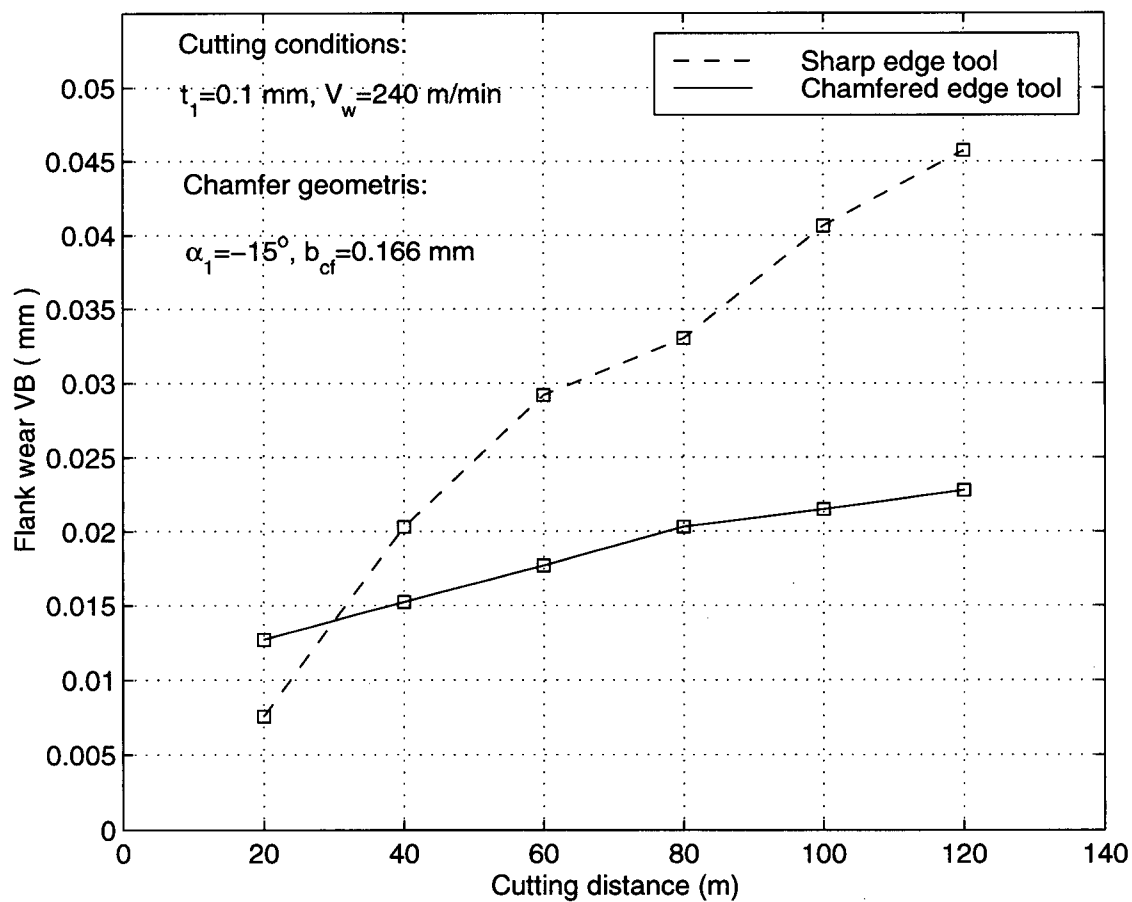


Figure 4.12: Comparison of tool wear history between a chamfered tool with -15° chamfer angle and a conventional sharp tool (SANDVIK carbide tools).

angle at the cutting speed of 240 m/min shows the development of tool wear is nearly two times lower than that of a sharp tool, much lower than that of sharp tool at the cutting speed of 600 m/min.

4.3.3 Summary

Mechanics of cutting with chamfered tools is presented in this chapter. The proposed model extends the analytic approach of Oxley et al. [6], [36] to chamfered tools. The plastic deformation zones are divided into primary shear zone, secondary deformation zone where the chip moves over the regular rake face, and the chamfered edge zone where the metal is trapped by forming a dead metal zone. An extrusion model is applied to the trapped metal zone. In all three zones, the yield and flow stress of the material are expressed as a function of strain, strain rate and temperature whose relationships are obtained from orthogonal cutting tests. The proposed model predicts the cutting forces and temperature in each deformation zone with realistic results. The model thus allows the analysis of how chamfer geometry and cutting speed influence the cutting performance, such as forces, temperature and tool wear. With the aid of proposed model, it has been observed that the optimal chamfer angle is -15° and the cutting speed is 240 m/min when dry cutting P20 mold steels with carbide tools. The same material can be cut up to 600 m/min with chamfered CBN tools.

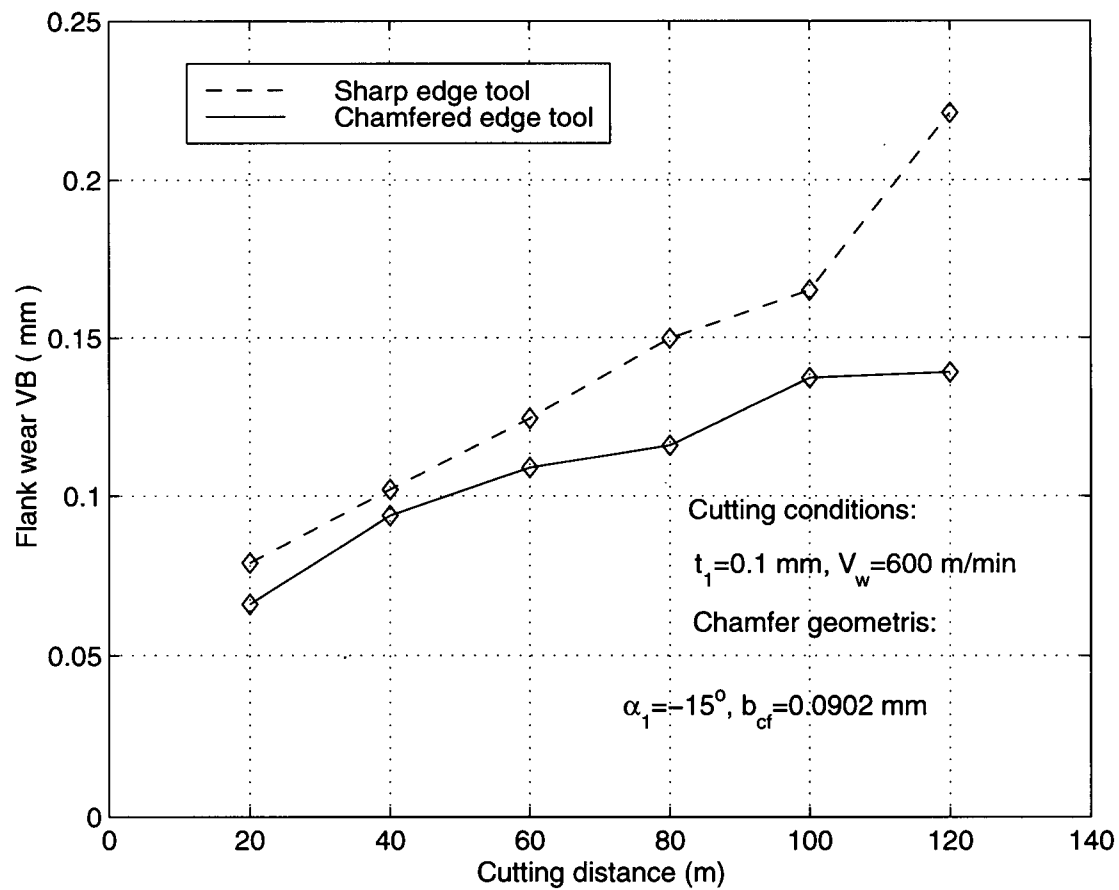


Figure 4.13: Comparison of the tool wear history between a chamfered tool with -15° chamfer angle and a conventional sharp tool (SANDVIK carbide tools).

Chapter 5

Conclusions

The objective of this thesis was to investigate the effects of tool edge geometry and cutting conditions on the machining of hardened steels. Analytical models have been developed for orthogonal machining, where sharp and chamfered cutting tools are modeled to investigate the influence of tool geometry and cutting conditions on cutting force and temperature for machinability analysis.

The mechanics of machining hardened mold steels are studied for both sharp edge and chamfered cutting tools. First, the cutting forces and temperature are predicted for machining with sharp tool, using Oxley's slip line field model [6]. The flow stress of the material is identified directly from orthogonal cutting tests where the shear angle, average friction coefficient, temperature, shear stress, strain and strain rate are estimated from material properties, measured chip thickness, rake face-chip contact length and cutting forces. Oxley et al.[6] used high speed compression test data to evaluate the flow stress, as opposed to orthogonal cutting test data proposed in this thesis. The analytical model is used to predict the cutting forces, shear angle, flow stresses and temperature on both primary shear and chip-tool rake face contact zones. The predicted results are compared with measurements from orthogonal cutting tests conducted with sharp ISO S10 carbide tools. The work material used in experiments was P20 mold steel. The following observations are made from the results:

- The strain hardening index evaluated from orthogonal cutting tests with sharp tools indicate that the strain hardening decreases with increasing speed. Experimental observation

also suggests that strain hardening becomes insignificant when cutting speed reaches a certain value.

- The temperature rise at the tool-chip interface mainly depends on the cutting speed. Predicted temperature rise in the primary shear zone is not significant at the speed range tested. However, the predicted temperature rise at the tool-chip interface is close to the melting temperature of P20 mold steel and diffusion temperature of Cobalt binding of the ISO S10 carbide tool at about cutting speed $300\text{m}/\text{min}$. Higher cutting speeds which cause to temperature beyond the diffusion limit of the carbide tool, leads to significant crater wear in the machining experiments.
- The model was found to be useful in analyzing optimal cutting speeds and chip loads in continuous turning of P20 mold steels.

Mechanics of cutting with chamfered tools has been modeled by extending the slip line field from the primary and the secondary deformation zones to the dead metal zone trapped over the chamfer land. The dead metal zone is assumed to be formed as the continuation of the primary shear line towards the cutting edge. As suggested by the experimental observations reported in the literature, the trapped metal is assumed to stay stationary and form a natural cutting edge as the continuation of the main rake face. The metal flow at the boundary of the dead metal is modeled similar to an extrusion process, where the boundary is assumed to act like a die wall. The contact between the chip and the main rake face is assumed to have an equal mixture of sticking and sliding zones. The total strain and friction energy produced in the primary, secondary and dead chamfer zones are formulated. The shear angle in the primary shear zone is predicted by minimizing the total energy consumed in chip formation. The proposed model predicts stresses, forces, temperature, and strain, strain rate and temperature dependent flow stress in the primary shear zone, dead metal boundary and at the chip - rake face contact area. The prediction results compared favourably with the experimental measurements conducted with chamfered ISO

S10 carbide and MITSUBISHI CBN cutting tools used in orthogonal turning of P20 mold steels.

The following conclusions are drawn from the chamfered cutting tool model and experimental results:

- Predicted and experimentally determined shear angles indicate that chamfer does not change the shearing process in the primary shear deformation zone significantly. Friction angles at the tool-chip interface, the cutting energy consumed, and cutting temperature rise in the primary shear deformation and tool rake face - chip interface zones show similar trends. However, predicted and experimentally measured cutting forces increased with the increasing chamfer angle, which is attributed to the presence of pressure and friction load at the dead metal - metal flow interface over the tool chamfer. Since the pressure on the dead metal interface coincides with the feed direction, the feed forces increase more than the tangential forces as the chamfer angle is increased.
- CBN tools seem to have a lower coefficient of friction than ISO S10 carbide tools. The friction coefficient for ISO S10 carbide tools varied from 28° to 26° as the cutting speed increased from 240 to 600 m/min, which resulted in an average shear angle of about 30° . When the cutting speed is varied from 240 to 1000 m/min with the CBN tools, the friction angle varied from only 16° to 19° . Therefore, the predicted and experimental shear angle and cutting energy did not also exhibit noticeable change within the cutting speed ranges tested. Furthermore, the cutting forces did not change significantly within the cutting speed ranges of 240 m/min to 1000 m/min. The predicted temperature indicates that the P20 material already reaches its re-crystallization phase (1000°C , γ region in Fe-C phase diagram) at the cutting speed 240 m/min as the chamfered tools were used in cutting tests. Therefore, there is no strain hardening to cause a force increase in the secondary zone beyond this speed.

- The temperature at the chip - tool interface reaches the diffusion limit of binding materials within the tool. This limit is about 1300°C at the cutting speed of $240\text{m}/\text{min}$ for chamfered ISO S10 carbide tools, and 1600°C at the cutting speed of $600\text{m}/\text{min}$ for chamfered CBN tools. Accelerated crater wear has been observed beyond these cutting speeds due to the diffusion of binding materials Cobalt and Al_2O_3 for carbide and CBN tools, respectively.
- In addition to cutting speed, the tool wear experiments indicate that the chamfer angle has a strong influence on the tool wear. When chamfer angle is varied from 0° to -35° on carbide tools, the minimum tool wear is observed around chamfer angle -15° . Larger chamfer angles increase the force and friction, and smaller chamfer angles weaken the wedge of cutting tools, hence, causing more tool wear. When the same volume of material was removed, the cutting speed at $240\text{ m}/\text{min}$ gave about 6 times lower flank wear than the cutting speed $600\text{ m}/\text{min}$, where severe crater wear due to diffusion of Cobalt binding was observed. CBN tools with -25° chamfer angle outperformed the CBN tools with -35° chamfer angle. Furthermore, the Scanning Electron Microscope (SEM) results of CBN tools with -35° showed a significant amount of micro-crack both within the CBN material and CBN-carbide bonding interface at the cutting speed of $800\text{ m}/\text{min}$ in turning tests.

This thesis presents a useful analytical model in analyzing the influence of tool geometry and cutting conditions in high speed machining of hardened steels. The model can be used for other materials cut at a wide speed range. The model is applicable to continuous machining, i.e. turning, where the process is at steady state. However, dies and molds are often machined using milling operations where the process is intermittent. The cutting tools enter and exit the material, and experience varying chip and thermal loads. Furthermore, ball end mills are used in machining dies with sculptured surfaces. The cutting speed starts from zero to the

highest value from the tip toward the ball-shank boundary of the ball end mills. As a result, the temperature, chip load and even edge geometry change for helical ball end mills. Although the proposed model is useful for turning, and a good starting point for milling, it should be extended to consider time varying nature of the forces, temperature and the corresponding material properties. Finite Element or Finite Difference models can be considered to investigate the dynamic process in the future.

Bibliography

- [1] E. Budak, Y. Altintas and E.J.A. Armarego, 1996, " Prediction of Milling Force Co-efficients From Orthogonal Cutting Data ", *Journal of Manufacturing Science and Engineering*, Vol. 118, pp216-224, May.
- [2] E. Shamoto and Y. Altintas, ASME 1997, " Prediction of Shear Angle in Oblique Cutting with Maximum Shear Stress and Minimum Energy Principle", *1997 ASME International Mechanical Engineering Congress and Exposition*, MED-Vol. 6-1, pp121-128.
- [3] M. Hiraro, J. Tlustý, R. Sowerby and G. Chandra, 1982, " Chip Formation with Chamfered Tools ", *Journal of Engineering for Industry*, Vol. 104, pp339-342, November.
- [4] T. Altan, B.W. Lilly, J.P. Kruth, et al., 1993, " Advanced Technologies for Die and Mold Manufacturing ", *Annals of the CIRP*, Vol.42, no.2, pp707-716.
- [5] M.A. Elbestawi, L. Chen, C.E. Becze and T.I. El-Wardany, 1997, " High-Speed Milling of Dies and Molds in Their Hardened State ", *Annals of the CIRP*, Vol. 46, pp57-59.
- [6] P.L.B. Oxley, 1989, *Mechanics of Machining-an analytical approach to assessing machinability*, Ellis Horwood Limited.
- [7] P. Mathew, W.F. Hastings and P.L.B. Oxley, 1979, " Machining - a study in high strain rate plasticity ", *Mechanical Properties at High Rates of Strain, 1979, Proceedings of the Second Conference on the Mechanical Properties of Materials at High Rates of Strain, The Institute of Physics Bristol and London, Oxford*, 28-30 March.
- [8] R.N. Roth and P.L.B. Oxley, 1972, " Slip-Line Field Analysis for Orthogonal Machining Based upon Experimental Flow Fields ", *Journal of Mechanical Engineering Science*, Vol 14, No 2, pp85-97.
- [9] R.J. Seethaler and I. Yellowley, 1997, "An Upper-Bound Cutting Model for Oblique Cutting Tools with A Nose Radius ", *Int. J. Mach. Tools Manufact.*, Vol. 37, No. 2, pp119-134.
- [10] I. Yellowley, 1983, " The Influence of Work Hardening on the Mechanics of Orthogonal Cutting with Zero Rake ", *Int. J. Mach. Tools Des. Res.*, Vol. 23, No. 4, pp181-189.
- [11] I. Yellowley and C.T. Lai, 1993, " The Use of Force Ratios in the Tracking of Tool Wear in Turning ", *Journal of Engineering for Industry*, Vol. 115, August, 370-372.

- [12] R. Radulescu and S.G. Kapoor, 1994, " An Analytical Model for Prediction of Tool Temperature Fields during Continuous and Interrupted Cutting ", *Journal of Engineering for Industry*, Vol. 116, pp135-143, May.
- [13] K.F. Ehmann, S.G. Kapoor, R.E. Devor, and I. Lazoglu, 1997, " Machining Process Modeling: A Review ", *Journal of Manufacturing Science and Engineering*, Vol. 119, November, pp655-663.
- [14] E. Oberg, F.D. Jones, H.L. Horton and H.H. Ryffel, 1992, *Machinery's Handbook*, 24th edition, INDUSTRIAL PRESS INC., New York.
- [15] T. Hosi, " Recent Development in Silver White Chip (SWC) Cutting ", *Cutting Tool Materials, Proceedings of an International Conference, Materials/Metalworking Technology Series*, September, 1980, Kentucky.
- [16] M. Oyane, F. Takashima, K. Oskada, and H. Tanaka, 1967, " The Behavior of Some Steels under Dynamic Compression ", *Proc. 10th Japan Congress on Testing Material*, p72-76.
- [17] J.H. Dautzenberg, P.C. Veenstra, and A.C.H. Van der Wolf, 1981, " The Minimum Energy Principle for the Cutting Process in Theory and Experiment ", *Annals of CIRP*, vol.30, p1-4.
- [18] B.F. Von Turkovich, 1979, " Influence of very High Cutting Speed on Chip Formation Mechanics ", *7th NAMRC*, p241-247.
- [19] G. Boothroyd, 1963, " Temperatures in Orthogonal Metal Cutting ", *Proc. Inst. Mech. Eng.*, vol.177, p789-802.
- [20] C.W. MacGregor, J.C. Fisher, 1946, " A Velocity Modified Temperature for the Plastic Flow of Metals ", *J. Appl. Mech.*, ASME, vol.13, A11-A16.
- [21] M.E. Merchant, 1945, " Mechanics of the Metal Cutting Process, II. Plasticity Conditions in Orthogonal Cutting ", *J. Appl. Phys.*, Vol.16, p318-324.
- [22] E.H. Lee, B.W. Shaffer, 1951, " The Theory of Plasticity Applied to A Problem of Machining ", *Trans. ASME, J. Appl. Mech.*, Vol.18, p405-413.
- [23] M.C. Shaw, N.H. Cook, and I. Finnie, 1953, " Shear Angle Relationship in Metal Cutting ", *Trans. ASME* 75, p273-288.
- [24] S. Kobayashi, E.G. Thomsen, 1962, " Metal Cutting Analysis-II New Parameters ", *Journal of Engineering for Industry*, Vol.84, p71-80.
- [25] G.A. Robert, R.A. Cary, 1980, *Tool Steels*, 4th edition, ASM.

- [26] W. Johnson, R. Sowerby, J.B. Haddow, 1970, *Plane-Strain Slip-Line Fields: Theory and Bibliography*, Edward Arnold LTD.
- [27] J. Chakrabarty, 1987, *Theory of Plasticity*, McGraw-Hill Book Company.
- [28] N.N. Zorev, 1963, " Interrelationship Between Shear Processes Occurring Along Tool Face and on Shear Plane in Metal Cutting ", *Proceedings of International Research in Production Engineering Research Conference*, p42-49, Sep.
- [29] M.C. Shaw, Resume and Critique of Papers in Part One, 1963, *Proceedings of International Research in Production Engineering Research Conference*, p3-17, Sep.
- [30] J.A. Schey, 1983, *Tribology in Metal Working-Friction, Lubrication, and Wear*, ASM.
- [31] E.G. Thomsen, C.T. Yang, S. Kobayashi, 1965, *Mechanics of Plastic Deformation In Metal Processings*, Macmillan Company, New York.
- [32] P. Albrecht, 1960, " New Developments in the theory of the Metal Cutting Process Part 1- The Ploughing Process in Metal Cutting ", ASME, *Journal of Engineering for Industry*, pp348-358.
- [33] E.J.A. Armarego and R.C. Whitfield, 1985, " Computer Based Modeling of Popular Machining Operations for Force and Power Prediction ", *Annals of the CIRP*, Vol.31, January, pp65-69.
- [34] E.J.A. Armarego, 1982, " Practical Implications of Classical thin shear zone cutting analysis ", *UNESCO-CIRP seminar on manufacturing Technology*, Singapore.
- [35] G.S. Gad, E.J.A. Armarego and A.J. R. Smith, 1992, " Tool-Chip Contact Length in Orthogonal Machining and Its Importance in Tool Temperature Prediction ", *International Journal of Production Research*, Vol. 30, no. 3, pp485-501.
- [36] W.F. Hastings, P. Mathew and P.L.B. Oxley, 1980, " A Machining Theory for Predicting Chip Geometry, Cutting Forces, etc. from Work material Properties and Cutting Conditions ", *Proceedings of the Royal Society of London*, Vol.371, Series A, pp569-587.
- [37] D.A. Stephenson, 1991, " Assessment of Steady-State Metal Cutting Temperature Models Based on Simultaneous Infrared and Thermocouple Data ", *Journal of Engineering for Industry*, Vol.113, May, pp121-128.
- [38] D.A. Stephenson, 1989, " Material Characterization for Metal-Cutting Force Modeling ", *Journal of Engineering Materials and Technology*, Vol.111, April, pp210-219.
- [39] M.C. Shaw, 1984, *Metal Cutting Principles*, Clarendon Press, Oxford.

- [40] D.E. Dimla Jr, P.M. Lister and N.J. Leighton, 1997, " Neural Network Solution to the Tool Condition Monitoring Problem in Metal Cutting - A Critical Review of Methods ", *International Journal of Machine Tool Manufacturing*, Vol.37, No.9, pp1219-1241.
- [41] J.A. Arsecularatne, 1997, " On Tool-Chip Interface Stress Distribution, Ploughing Force and Size Effect in Machining ", *International Journal of Machine Tool Manufacturing*, Vol.37, No.7, pp885-899.
- [42] H. Berns, J. Liu and W. Theisen, 1996, " A New Experimental Approach to Metal Cutting ", *Z.Metallkd*, Vol.87, No.5.
- [43] E.J.A. Armarego and R.H. Brown, 1969, *The Machining of Metal*, Prentice-Hall Inc..
- [44] A. Ghosh and A.K. Mallik, 1986, *Manufacturing Science*, Ellis Horwood Limited.
- [45] E.M. Trent, 1991, *Metal Cutting*, Third edition, Butterworth-Heinemann Ltd.
- [46] K. Hitomi, 1961, " Fundamental Machinability Research in Japan ", *Journal of Engineering for Industry*, November, pp531-544.
- [47] S. Jacobson and P. Wallen, 1988, " A New Classification System For Dead Zone in Metal Cutting ", *International Journal of Machine Tools Manufacturing*, Vol.28, No.4, pp529-538.
- [48] H.K. Tönshoff, W. Bussmann and C. Stanske, 1986, " Requirements on Tools and Machines When Machining Hard Materials ", *Proceedings of the 26th International Machine Tool Design and Research Conference*, September, pp349-357.
- [49] E. Usui, K. Kikuchi and K. Hoshi, 1964, " The Theory of Plasticity Applied to Machining with Cut-Away Tools ", *Journal of Engineering for Industry*, Transaction of ASME, May, pp95-104.
- [50] H.T. Zhang, P.D. Liu and R.S. Hu, 1991, " A Three Zone Model and Solution of Shear Angle in Orthogonal Machining ", *Wear*, Vol.143, pp29-43.
- [51] B. Avitzur, 1968, *Metal Forming: Process and Analysis*, McGraw-Hill Book Company.
- [52] H. Kudo, 1965, " Some New Slip-Line Solutions for Two-Dimensional Steady-State Machining ", *International Journal of Mechanical Science*, Vol.7, pp43-55.
- [53] W.F. Hosford and R.M. Caddell, 1993, *Metal Forming Mechanics and Metallurgy*, PTR Prentice-Hall Inc..
- [54] D. Dudzinski and A. Molinari, 1997, " A Modeling of Cutting for Viscoplastic Materials ", *International Journal of Mechanical Science*, Vol. 39, No. 4, pp369-389.

- [55] R.F. Recht, 1985, " A Dynamic Analysis of High-Speed Machining ", *Journal of Engineering for Industry*, Vol. 107, November, pp309-315.
- [56] J.S. Strenkowski and J.T. Carroll, 1985, " A Finite Element Model of Orthogonal Metal Cutting ", *Journal of Engineering for Industry*, Vol. 107, pp349-354.
- [57] K. Komvopoulos and S.A. Erpenbeck, 1991, " Finite Element Modelling of Orthogonal Metal cutting ", *Journal of Engineering for Industry*, Vol. 113, pp253-267.
- [58] T.D. Marusich and M. Ortiz, 1995, " Modeling and Simulation of High-Speed Machining ", *International Journal of Numerical Methods in Engineering*, Vol. 38, pp3675-3694.
- [59] R.A.C. Slater, 1977, *Engineering Plasticity - Theory and Application to Metal Forming Process*, THE MACMILLAN PRESS LTD.
- [60] P.W. Wallace and G. Boothroyd, 1964, " Tool Forces and Tool-Chip Friction in Orthogonal Machining ", *Journal of Mechanical Engineering Science*, Vol. 6, No. 1, pp74-87.
- [61] W.B. Palmer and P.L.B. Oxley, 1959, " Mechanics of Orthogonal Machining ", *Proceedings Institution of Mechanical Engineers*, Vol. 173, No. 24, pp623-654.
- [62] M.G. Stevenson and P.L.B. Oxley, 1970-1971, " An Experimental Investigation of the Influence of Strain-Rate and Temperature on the Flow Stress Properties of a Low Carbon Steel Using a Machining test ", *Proceedings Institution of Mechanical Engineers*, Vol. 185, pp741-754.
- [63] *Modern Metal Cutting - A Practical Handbook*, AB Sandvik Coromant, Technical Editorial Department, Sweden, 1994.
- [64] M.I. Sadik and B. Lindström, 1993, " The Role of Tool-Chip Contact Length in Metal Cutting ", *Journal of Materials Processing Technology*, Vol 37, pp613-627.
- [65] T.C. Hsu, 1966, " A Study of the Normal and Shear Stress on a Cutting Tool ", *Journal of Engineering for Industry*, February, pp51-64.
- [66] M.E.S. Abdelmoneim and R.F. Scrutton, 1974, " Tool Edge Roundness and Stable Build-Up Formation in Finish Machining ", *Journal of Engineering for Industry*, November, pp1258-1267.
- [67] T.I. Elwardany, E. Mohammed and M.A. Elbestawi, 1996, " Cutting Temperature of Ceramic Tools in High Speed Machining of Difficult-to-cut Materials ", *International Journal of Machine Tools Manufacturing*, Vol. 36, No. 5, pp611-634.
- [68] W. Johnson, 1979, " Applications: Processes Involving High Strain Rates ", *Institution of Physics Conference*, Series No. 47: Chapter 4, pp337-357.

- [69] Xiaoping Li, 1997, " Development of a Predictive Model for Stress Distributions at the Tool-Chip Interface in Machining ", *Journal of Materials Processing Technology*, 63, pp169-174.
- [70] F. Vygen, "Characteristics of Tool Wear in High Speed Machining of P20 Mold Steel using CBN and Carbide Tools ", *Diploma thesis, visiting student in the Manufacturing Automation Laboratory at UBC, Technological University of Munich, Germany*, 1998.
- [71] J.H. Weiner, 1955, "Shear-Plane Temperature Distribution in Orthogonal Cutting", *Trans. ASME* 77, pp1331-1341.
- [72] ASM International Handbook Committee, 1989, *Metal Handbook Ninth Edition*, Vol. 16, ASM, pp71-117.
- [73] A.O. Tay, M.G. Stephensen, G. De Vahl Davis, and P.L.B. Oxley, 1976, " A Numerical Method for Calculating Temperature Distributions in Machining, from Force and Shear Angle Measurements ", *International Journal of Machine Tool Design and Research*, Vol. 16, pp335-349.
- [74] D. Kececiloglu, 1960, " Shear-Zone Size, Compressive Stress, and Shear Strain in Metal-Cutting and Their Effects on Mean Shear-Flow Stress ", *Journal of Engineering for Industry*, February, pp79 - 86.

Appendix A

Temperature in the Primary Shear and the Tool-Chip Interface Zones

Material thermal properties of P20 mold steel

The thermal properties, heat conductivity (κ) and specific heat (c) for P20 mold steel is given by the material handbooks as:

$$\begin{aligned}\kappa &= 28.74 + 0.0053T \text{ (J/m s } ^\circ\text{C)} \\ \rho c &= 3.59 \times 10^6 - 100T \text{ (J/m}^3\text{ } ^\circ\text{C)}\end{aligned}$$

Calculation of temperature in the primary shear zone

The temperature in the primary shear zone T_{AB} is determined by considering the plastic work done in this zone and is given by

$$T_{AB} = T_{room} + \eta \left[\frac{(1 - \lambda_s) F_s \cos \alpha_o}{\rho c t_1 w \cos(\phi - \alpha_o)} \right] \quad (\text{A.1})$$

where F_s , ϕ , α_o , and t_1 are shear force on \overline{AB} , shear angle, tool rake angle, and undeformed chip thickness, respectively. T_{room} is the initial temperature of work material. Based on heat partition principle, Boothroyd [19] suggested that a coefficient (λ_s) can be used to determine the proportion of heat conducted into the workpiece in the primary shear zone. It is found that λ_s is a function of $R_T \tan \phi_s$. Oxley et al. [6], [36], [62] proposed empirical equations to calculate λ_s , which is closed to the results reported by Weiner's [71] energy partition function.

$$\left. \begin{aligned}\lambda_s &= 0.5 - 0.35 \log_{10}(R_T \tan \phi) \text{ for } 0.04 \leq R_T \tan \phi \leq 10.0 \\ \lambda_s &= 0.3 - 0.15 \log_{10}(R_T \tan \phi) \text{ for } R_T \tan \phi > 10.0\end{aligned} \right\} \quad (\text{A.2})$$

Where R_T is non-dimensional thermal number given by $R_T = \frac{\rho c V_w t_1}{\kappa}$.

Calculation of temperature in the tool-chip interface zone

Oxley et al. [6], [36] proposed that the temperature rise at the tool-chip interface (T_{inter}) is determined by

$$\left. \begin{aligned} T_{inter} &= T_i + 0.9 \Delta T_M \\ \Delta T_c &= \frac{F_{fc} \sin \phi}{\rho c t_1 w \cos(\phi - \alpha_o)} \\ F_{fc} &= R_s \sin \beta = \frac{k_{AB} t_1 w \sin \beta}{\sin \phi \cos \theta} \\ \log_{10} \left(\frac{\Delta T_M}{\Delta T_c} \right) &= 0.06 - 0.195 \delta \sqrt{\frac{R_T t_2}{l_c}} + 0.5 \log_{10} \left(\frac{R_T t_2}{l_c} \right) \end{aligned} \right\} \quad (A.3)$$

where $T_i \equiv \{T_{AB}, T_{cf}\}$. For cutting with sharp tools, $T_i = T_{AB}$. For cutting with chamfered tools, $T_i = T_{cf}$. t_2 , δ , l_c is the chip thickness, thickness of plastic zone along the tool-chip interface, and the contact length along the tool-chip interface, respectively. ΔT_M is the maximum rise of temperature along the tool-chip interface. ΔT_c is the average temperature rise in the chip due to frictional work. In the calculation of average temperature in the tool-chip plastic deformation zone, the ratio of ΔT_M to ΔT_c is required as proposed by Broothroyd [19]. Stevenson and Oxley [62] applied Broothroyd's analysis and obtained an empirical equation as shown above to determine the ratio of ΔT_M to ΔT_c .

Appendix B

Mapping Flow Stresses in the machining process

Evaluation of flow stress in primary deformation zone

As presented in chapter 3, the flow stress σ_1 and strain hardening index n in the primary shear deformation zone are mapped from the shear strain γ_{AB} and shear strain rate $\dot{\gamma}_{AB}$. A empirical correlation of σ_1 and strain hardening index n with shear strain γ_{AB} and shear strain rate $\dot{\gamma}_{AB}$ is obtained from orthogonal machining tests under a range of cutting condition shown as follows

$$\left. \begin{aligned} &\text{For } t_1 \leq 0.03 \text{ mm} \\ \sigma_1 &= 10864.4399 \dot{\gamma}_{AB}^{-0.071} \gamma_{AB}^{-1.385} \text{ (MPa)} \\ n &= 0.00866 \dot{\gamma}_{AB}^{-0.0014} \gamma_{AB}^{2.476} \end{aligned} \right\} \quad (\text{B.4})$$

For $t_1 > 0.03 \text{ mm}$

$$\left. \begin{aligned} \sigma_1 &= 1850.1639 \dot{\gamma}_{AB}^{0.0178} \gamma_{AB}^{-0.65497} \text{ (MPa)} \\ n &= \frac{10.17495 \dot{\gamma}_{AB}^{-0.5340} \gamma_{AB}^{2.67378}}{V_w t_1} \end{aligned} \right\} \quad (\text{B.5})$$

Flow stresses ($\sigma \equiv \{\sigma_{cf}, \sigma_{inter}\}$) in the chamfered and secondary deformation zone

Again, the following expressions are calibrated from orthogonal cutting tests with sharp tools, where flow stresses in the primary and secondary zones and their corresponding velocity modified temperature are calculated (see, experimental modeling in chapter 3). Hence, the mapping relation between flow stress and velocity modified temperature T_m is obtained by

$$\left. \begin{aligned} T_m \leq 481.0 \text{ (K)} & \rightarrow \sigma = 2732.126 - 4.87 T_m \text{ (Mpa)} \\ 481.0 < T_m \leq 730.0 \text{ (K)} & \rightarrow \sigma = -0.6596 \cdot 10^{-4} T_m^3 + 0.10957 T_m^2 - 59.18 T_m + 10821.129 \text{ (MPa)} \\ T_m > 730.0 \text{ (K)} & \rightarrow \sigma = 260.0 \text{ (MPa)} \end{aligned} \right\} \quad (\text{B.6})$$

The velocity modified temperature in chamfered edge (T_{mcf}) and tool-chip interface zone (T_{mtc}) are given by

$$T_{mcf} = (T_{cf} + 273)(1 - 0.09 \log_{10}(\dot{\epsilon}_{cf})) \quad (\text{B.7})$$

$$T_{mtc} = (T_{inter} + 273)(1 - 0.09 \log_{10}(\frac{\dot{\gamma}_{inter}}{\sqrt{3}})) \quad (\text{B.8})$$

Appendix C

Identification of Edge Forces

A schematic diagram for the identification of edge force components in cutting and feed directions, experimental shear stress, shear angle, friction angle, and cutting force coefficients is shown in figure C.1. To identify the edge forces, cutting forces F_c , F_t which correspond a range of undeformed chip thickness t_1 are required at different cutting speeds. A C program is developed to achieve experimental identification of edge force components. Once a data file, which contains a set of undeformed chip thickness t_1 , and corresponding chip thickness t_2 , width of cut w , measured cutting forces F_c , F_t , and rake angle α_o , is loaded to the program, the edge forces are found using the least square root method as shown in figure C.1. Once edge force components F_{ce} and F_{te} , shear angle ϕ , and friction angle β are identified, experimental shear stress k_{AB} and cutting force coefficients K_{tc} and K_{fc} can be determined by following equations

$$\left\{ \begin{array}{l} k_{AB} = \frac{[(F_c - F_{ce})\cos\phi - (F_t - F_{te})\sin\phi]\sin\phi}{t_1 w} \\ K_{tc} = \frac{k_{AB} \cos(\beta - \alpha_o)}{\sin\phi \cos(\phi + \beta - \alpha_o)} \\ K_{fc} = \frac{k_{AB} \sin(\beta - \alpha_o)}{\sin\phi \cos(\phi + \beta - \alpha_o)} \end{array} \right. \quad (C.9)$$

The total cutting force F_c and feed force F_t can be expressed as

$$\left\{ \begin{array}{l} F_c = F_{ce} + K_{tc}t_1w \\ F_t = F_{te} + K_{fc}t_1w \end{array} \right\} \quad (C.10)$$

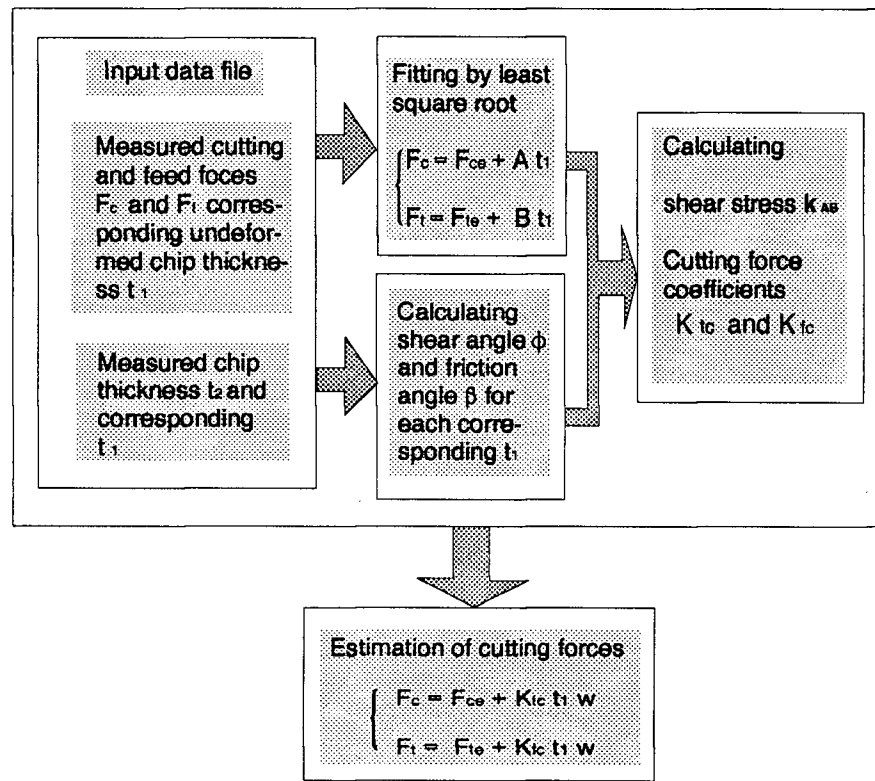


Figure C.1: Experimental identification of edge force components

From experimental observations, edge forces vary with the cutting speeds. Albrecht [32] also stated this from his experimental observations. Both F_{ce} and F_{te} are found to decrease with the increase of cutting speed V_w .

Under the cutting conditions: $V_w=100, 240, 380, 600$ m/min, and $w=3.6$ mm, the corresponding edge forces, F_{ce} and F_{te} are calculated from the developed program. A empirical equation used to determine edge force components F_{ce} and F_{te} at different cutting speed is obtained as shown by equation C.11

$$\left. \begin{aligned} F_{ce} &= 0.4318 \times 10^{-3} V_w^2 - 0.53524 V_w + 276.67 \\ F_{te} &= 0.4919 \times 10^{-3} V_w^2 - 0.7225 V_w + 352.71 \end{aligned} \right\} \quad (C.11)$$

It is noted that equation C.11 is valid for cutting carbide tool (SANDVIK, S10, see figure 3.8).

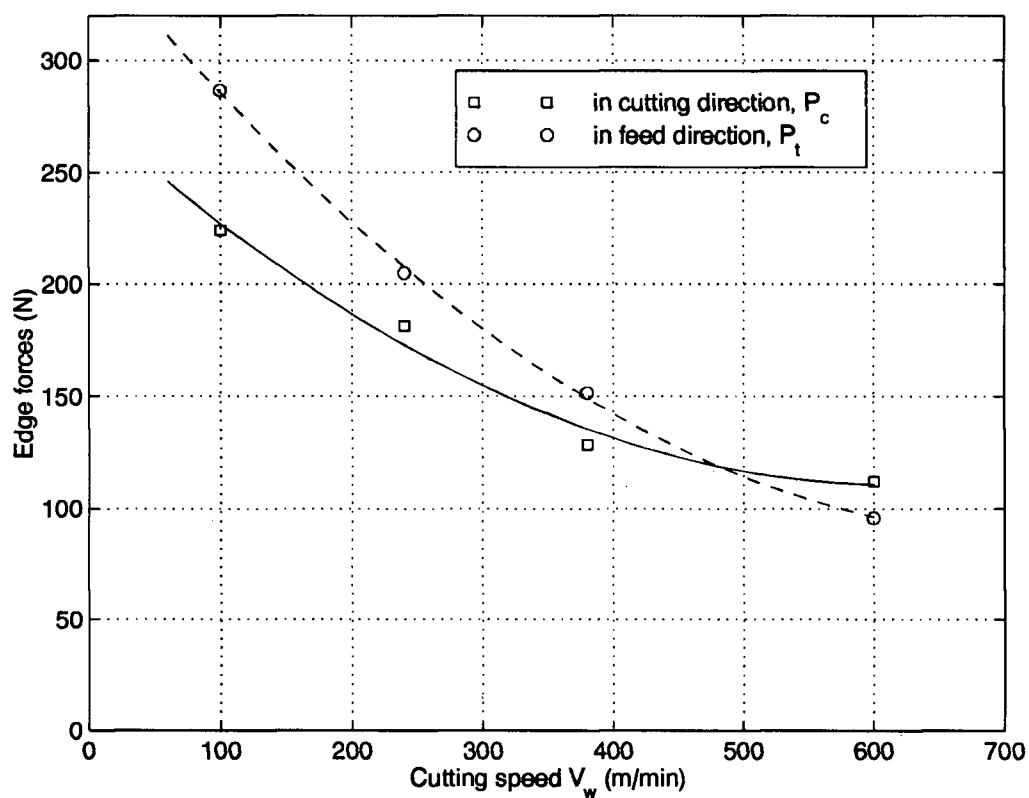


Figure C.2: Plot of variation of edge forces with cutting speed

Figure C.2 shows the variation of edge forces with cutting speeds.

For CBN tools, edge forces are given by

$$F_{ce} = 80.0 \text{ (N)} \quad (\text{C.12})$$

$$F_{te} = 180.0 \text{ (N)} \quad (\text{C.13})$$